Computational Homogenization of Piezoelectric Materials using FE^2 Methods and Configurational Forces

Dem Fachbereich Maschinenbau und Verfahrenstechnik

der Technischen Universität Kaiserslautern

zur Erlangung des akademischen Grades

Doktor-Ingenieur (Dr.-Ing.)

genehmigte Dissertation

von

Herrn

M.Sc. Md Khalaquzzaman

aus Dinajpur, Bangladesch

Herausgeber

Druck

Acknowledgement

First of all, I am highly grateful to my supervisor Prof. Dr.-Ing. Ralf Müller for his continual mentoring and support throughout this dissertation. I thank him for the guidance and advice which brought my dissertation to success. I would like to thank the co-supervisor Prof. Dr. Bai-Xiang Xu for her effort to review this work. My special thanks goes to Prof. Dr.-Ing. Eberhard Kerscher for chairing the examination committee.

I would like to thank Dr.-Ing. Sarah Staub for her valuable discussions on computational homogenization. I specially thank Dr.-Ing. David Schrade, M.Sc. Matthias Sabel for their help to my dissertation in various ways. I am thankful to all of my colleagues from the Institute of Applied Mechanics for their support. I want to express my gratefulness to the Bangladeshi community in Kaiserslautern for their mental and social support throughout the time of my dissertation.

I want to thank my wife and my family for their support and encouragement.

Md Khalaquzzaman
26/07/2015, Kaiserslautern

Zusammenfassung

Piezoelektrische Materialien besitzen die Eigenschaft, elektrische und mechanische Signale zu koppeln. Bei diesen Werkstoffen ist es möglich, durch Aufbringen einer mechanischen Last, ein elektrisches Feld zu erzeugen. Dieses Phänomen bezeichnet man als den piezoelektrischen Effekt. Umgekehrt führt das Anlegen einer elektrischen Spannung zu einer mechanischen Deformation, was als inverser piezoelektrischer Effekt bezeichnet wird. Aufgrund dieser Eigenschaften von piezoelektrischen Materialien, werden sie häufig in Sensoren und Aktoren eingesetzt. Ferroelektrische oder piezoelektrische Materialien ändern ihre Polarisation durch Aufbringen äußerer Lasten. Dank dieser Eigenschaft, können sie als dauerhafter Speicher mit direktem Zugriff eingesetzt werden. Um diese Werkstoffe in technischen Anwendungen effektiv einzusetzen, ist eine genaue Beschreibung des Antwortverhaltens erforderlich. Aufgrund des wachsenden Bedarfs nach einer exakten Charakterisierung, gewinnen numerische Methoden zunehmend an Bedeutung.

Viele Konstruktionswerkstoffe besitzen Inhomogenitäten auf mikroskopischer Ebene. Diese Inhomogenitäten erschweren die Charakterisierung des Antwortverhaltens mit experimentellen sowie numerischen Methoden. Andererseits können diese Defekte auch positive Eigenschaften hervorrufen; so weisen faserverstärkte Kunststoffe eine hohe Festigkeit auf, bei gleichzeitig niedrigem Gewicht. Auch bei piezoelektrischen Materialien spielen Inhomogenitäten auf der Mikroebene eine wichtige Rolle. Diese Inhomogenitäten resultieren zum einen aus der Struktur der Werkstoffe, die aus Domänen und Domänenwände, Körnern und Korngrenzen, sowie mikroskopischen Rissen besteht. Um den Einfluss der Mikrostruktur auf das Verhalten der Makrostruktur zu berücksichtigen, muss eine Homogenisierung der physikalischen Eigenschaften (z.B. in Form von Materialparametern) erfolgen. Eine Möglichkeit dazu ist die klassische Zwei-Skalen-Homogenisierung erster Ordnung mittels der FE^2-Methode, die in dieser Arbeit behandelt wird. Das Ziel dieser Arbeit ist es, den Einfluss der Mikrostruktur auf den Makro-Eshelby-Spannungstensor und die makroskopischen Konfigurationskräfte zu untersuchen. Die Konfigurationskräfte

werden an verschiedenen Defektanordnungen ausgewertet; unter anderem an der Rissspitze eines scharfen Risses im makroskopischen Bauteil.

Eine Literaturrecherche hat ergeben, dass der Makro-Verzerrungstensor verwendet wird um die Randbedingungen für die FE^2-Homogenisierung bei kleinen Verzerrungen zu ermitteln. Diese Vorgehensweise ist geeignet, um konsistente homogenisierte physikalische Eigenschaften (z.B. Spannungen, Verzerrungen) und homogenisierte Materialparameter (z.B. Steifigkeitstensor) zu bestimmen. Jedoch führt die Anwendung dieser Methode nicht zu einem physikalisch konsistenten Makro-Eshelby-Spannungstensor oder auf makroskopischer Ebene konsistenten Konfigurationskräften. Auch unter Vernachlässigung der volumenspezifischen Konfigurationskräfte auf der Mikro-Ebene, ruft diese Methode der Homogenisierung von piezoelektrischem Material unphysikalische volumenspezifische Konfigurationskräfte auf der Makro-Ebene hervor. Aus einer Analyse der Randbedingungen des repräsentativen Volumenelements (RVE) geht hervor, dass eine vom Verschiebungsgradienten getriebene Mikro-Randbedingung dieses Problem löst. Die Verwendung von Mikro-Randbedingungen, die auf dem Verschiebungsgradienten basieren, erfüllt auch die Hill-Mandel-Bedingung. Der Makro-Spannungstensor eines rein mechanischen Problems bei kleinen Verzerrungen kann auf zwei Arten berechnet werden: mit Hilfe von homogenisierten mechanischen Feldgrößen (Verschiebungsgradient und Spannungstensor) oder durch eine Volumenmittelung des Eshelby-Spannungstensors auf der Mikroebene. Die Hill-Mandel-Bedingung wird unter Berücksichtigung des Eshelby-Spannungstensors im Energieanteil jedoch nur von der zweiten Methode erfüllt. Bei Verwendung eines homogenisierten Eshelby-Spannungstensors aus homogenisierten physikalischen Eigenschaften führt in den Hill-Mandel-Bedingung zu einem weiteren Energieterm. Ein Körper verformt sich bei kleinen Deformationen entsprechend dem Verschiebungsgradient. Erfolgt die Homogenisierung mit Hilfe der verzerrungsgesteuerten Mikro-Randbedingung, so wird die Mikro-Ebene entsprechend den Makro-Verzerrungen deformiert. Die unmittelbare Umgebung des Gaußpunktes deformiert sich jedoch entsprechend dem Makro-Verschiebungsgradient. Dies erfordert Restriktionen an jedem Gaußpunkt auf Makro-Ebene, was zu unphysikalischen volumetrischen Konfigurationskräften auf der Makro-Ebene führen kann.

Eine auf der FE^2-Methode basierende Homogenisierungstechnik wird auch in dieser Arbeit für die Homogenisierung von piezoelektrischen Materialien verwendet. Bei dieser Methode wird jedem Gaußpunkt der Makro-Ebene ein repräsentatives Volumenelement zugeordnet, welches die Eigenschaften der Mikro-Struktur abbildet. Der makroskopische

Verschiebungsgradient und das elektrische Feld oder alternativ der Makro-Spannungstensor und die elektrische Verschiebung werden an das RVE am jeweiligen Gaußpunkt übergeben. Nach der Bestimmung der Randbedingungen erfolgt die Homogenisierung und die homogenisierten physikalischen Eigenschaften, sowie die Materialparamter werden an die Gaußpunkte übergeben. In dieser Arbeit werden zwei Fälle hinsichtlich der Ausbildung der Mikrostruktur an numerischen Beispielen untersucht: a) Homogenisierung bei stationärer Mikrostruktur und b) Homogenisierung bei zeitlich veränderlicher Mikrostruktur.

Für den ersten Fall werden die Domänenwände während der Homogenisierung des piezoelektrischen Materials fixiert. Bei hohen äußeren Lasten entspricht diese Annahme zwar nicht der Realität, führt aber zu einem besseren Verständnis des Einflusses der Mikrostruktur auf die Makro-Konfigurationskräfte. Die Homogenisierung wird an verschiedenen Mikrostrukturen und unter variierenden Lasten durchgeführt. Wenn die Last in Richtung der Polarisierung aufgebracht wird, wird eine niedrigere Konfigurationskraft an der Rissspitze beobachtet im Vergleich zu einer Belastung, welche normal zur Polarisationsrichtung angreift. Wenn die Polarisation innerhalb der Mikrostrukturen parallel oder normal zum elektrischen Feld und der Verschiebung ausgerichtet sind, werden nur Konfigurationskräfte parallel zum Ligament des Makro-Risses beobachtet. Im Fall von geneigten Polarisationsvektoren innerhalb der Mikrostruktur treten schräg zum Ligament ausgerichtete Konfigurationskräfte auf. Die numerischen Ergebnisse lassen auch darauf schließen, dass ein äußeres elektrisches Feld den Betrag der Konfigurationskräfte an den Knoten im Bereich der Rissspitze reduziert.

Im zweiten Fall können sich die Wände der Domänen innerhalb der Mikrostruktur in jedem Lastschritt bewegen. Daher liegt nach jedem Lastschritt eine neue Mikrostruktur vor, wenn die äußere Last größer als das Koerzitivfeld ist. Die Bewegung der Wände wird mit Hilfe der Konfigurationskräfte realisiert. In jedem Lastschritt werden die Knotenwerte der Konfigurationskräfte pro Einheitslänge auf die Domänenwände in einem Post-Processing Schritt berechnet. Die Kinetik der Domänenwände wird dann verwendet um deren neue Position zu bestimmen. Numerische Ergebnisse zeigen, dass in der Region um die Rissspitze die größten Veränderungen auftreten. Aus diesem Grund weichen die Werte der elektrischen Verschiebung auf der Makro-Ebene deutlich von denen aus Simulationen mit fixierten Domänenwänden ab. Die Bewegung der Wände führt dazu, dass Energie im System dissipiert wird. Daraus resultieren niedrigere Konfigurationskräfte an der Rissspitze auf der Makro-Ebene im Falle einer Homogenisierung mit veränder-

licher Mikrostruktur. Unter Verwendung der Homogenisierungsmethode mit veränderlicher Mikrostruktur ist es möglich, Hysteresekurven auf der Makro-Ebene zu erzeugen. Die Form der Hysteresekurven hängt dabei von der Rate der aufgebrachten äußeren elektrischen Last ab. Eine höhere Rate führt zu einer Vergrößerung der Hysterese.

Summary

Piezoelectric materials are electro-mechanically coupled materials. In these materials it is possible to produce an electric field by applying a mechanical load. This phenomenon is known as the piezoelectric effect. These materials also exhibit a mechanical deformation in response to an external electric loading, which is known as the inverse piezoelectric effect. By using these smart properties of piezoelectric materials, applications are possible in sensors and actuators. Ferroelectric or piezoelectric materials show switching behavior of the polarization in the material under an external loading. Due to this property, these materials are used to produce random access memory (RAM) for the non-volatile storage of data in computing devices. It is essential to understand the material responses of piezoelectric materials properly in order to use them in the engineering applications in innovative manners. Due to the growing interest in determining the material responses of smart material (e.g., piezoelectric material), computational methods are becoming increasingly important.

Many engineering materials possess inhomogeneities on the micro level. These inhomogeneities in the materials cause some difficulties in the determination of the material responses computationally as well as experimentally. But on the other hand, sometimes these inhomogeneities help the materials to render some good physical properties, e.g., glass or carbon fiber reinforced composites are light weight, but show higher strength. Piezoelectric materials also exhibit intense inhomogeneities on the micro level. These inhomogeneities are originating from the presence of domains, domain walls, grains, grain boundaries, micro cracks, etc. in the material. In order to capture the effects of the underlying microstructures on the macro quantities, it is essential to homogenize material parameters and the physical responses. There are several approaches to perform the homogenization. A two-scale classical (first-order) homogenization of electro-mechanically coupled materials using a FE^2-approach is discussed in this work. The main objective of this work is to investigate the influences of the underlying micro structures on the macro

Eshelby stress tensor and on the macro configurational forces. The configurational forces are determined in certain defect situations. These defect situations include the crack tip of a sharp crack in the macro specimen.

A literature review shows that the macro strain tensor is used to determine the micro boundary condition for the FE^2-based homogenization in a small strain setting. This approach is capable to determine the consistent homogenized physical quantities (e.g., stress, strain) and the homogenized material quantities (e.g., stiffness tensor). But the application of these type of micro boundaries for the homogenization does not generate physically consistent macro Eshelby stress tensor or the macro configurational forces. Even in the absence of the micro volume configurational forces, this approach of the homogenization of piezoelectric materials produces unphysical volume configurational forces on the macro level. After a thorough investigation of the boundary conditions on the representative volume elements (RVEs), it is found that a displacement gradient driven micro boundary conditions remedy this issue. The use of the displacement gradient driven micro boundary conditions also satisfies the Hill-Mandel condition. The macro Eshelby stress tensor of a pure mechanical problem in a small deformation setting can be determined in two possible ways: by using the homogenized mechanical quantities (displacement gradient and stress tensor), or by homogenizing the Eshelby stress tensor on the micro level by volume averaging. The first approach does not satisfy the Hill-Mandel condition incorporating the Eshelby stress tensor in the energy term, on the other hand, the Hill-Mandel condition is satisfied in the second approach. In the case of homogenized Eshelby stress tensor determined from the homogenized physical quantities, the Hill-Mandel condition gives an additional energy term. A body in a small deformation setting is deformed according to the displacement gradient. If the homogenization is done using strain driven micro boundary conditions, the micro domain is deformed according to the macro strain, but the tiny vicinity around the corresponding Gauß point is deformed according to the macro displacement gradient. This implies that some restrictions are imposed at every Gauß point on the macro level. This situation helps the macro system to produce nonphysical volume configurational forces.

A FE^2-based computational homogenization technique is also considered for the homogenization of piezoelectric materials. In this technique a representative volume element, which comprises of the micro structural features in the material, is assigned to every Gauß point of the macro domain. The macro displacement gradient and the macro electric field, or the macro stress tensor and the macro electric displacement are passed to the

RVEs at every macro Gauß point. After determining boundary conditions on the RVEs, the homogenization process is performed. The homogenized physical quantities and the homogenized material parameters are passed back to macro Gauß points. In this work numerical investigations are carried out for two distinct situations of the microstructures of the piezoelectric materials regarding the evolution on the micro level: a) homogenization by using stationary microstructures, and b) homogenization by using evolving microstructures.

For the first case, the domain walls remain at fixed positions through out the simulations for the homogenization of piezoelectric materials. For a considerably large external loading, the real situation is different. But to understand the effects of the underlying microstructures on the macro configurational forces, to some extent it is sufficient to do the homogenization with fixed or stationary microstructures. The homogenization process is carried out for different microstructures and for different loading conditions. If the mechanical load is applied in the direction of the polarization, a smaller crack tip configurational force is observed in comparison to the configurational force determined for a mechanical loading perpendicular to the polarization. If the polarizations in the microstructures are parallel or perpendicular to the applied electric field and the applied displacement, configurational forces parallel to the crack ligament of the macro crack are observed only. In the case of inclined polarizations in the microstructures, configurational forces inclined to the crack ligament are obtained. The simulation results also reveal that an application of an external electric field to the material reduces the value of the nodal configurational forces at the crack tip.

In the second case, the interfaces of the micro structures are allowed to move from their initial positions at every step of the applied incremental external loading. Thus, at every step of the application of the external loading, the microstructures are changed when the external loading is larger than the coercive field. The movement of the interfaces is realized through the nodal configurational forces on the micro level. At every step of the application of the external loading, the nodal configurational forces per unit length on the domain walls are determined in the post-processing of the FE-simulation on the micro domain. With the help of the domain wall kinetics, the new positions of the domain walls are determined. Numerical results show that the crack tip region is the most affected area in the macro domain. For that reason a very different distribution of the macro electric displacement is observed comparing the same produced by using fixed microstructures. Due to the movement of the domain walls, the energy is dissipated in the system. As a

result, a smaller configurational force appears at the crack tip on the macro level in the case of the homogenization by using evolving microstructures. By using the homogenization technique involving the evolution of the microstructures, it is possible to produce the electric displacement vs. electric field hysteresis loop on the macro level. The shape of the hysteresis loop depends on the value of the rate of application of the external electric loading. A faster deployment of the external electric field widens the hysteresis loop.

Contents

List of Figures

Chapter 1

Introduction

1.1 Motivation

Piezoelectric materials, which contain remanent polarizations, feature coupling between mechanical and electrical properties. These materials are capable of generating an electric field in response to a mechanical loading. This effect is called direct piezoelectric effect. In the inverse piezoelectric effect, these materials exhibit a deformation when an external electric field is applied. Piezoelectric materials are widely used in sensors and actuators due to their piezoelectric property. Common examples of piezoelectric sensors are sonic sensors, force and vibration sensors, etc. In valves (e.g., fuel injection, ink-jet) and ultra-sonic motors, piezoelectric materials are used as actuators. Piezoelectric materials are also used in composites and in multi-layer materials to obtain smart solutions in a variety of applications. On the micro level, these materials contain different domains of polarization, domain walls, grains, grain boundaries, micro cracks, etc. These micro features of piezoelectric materials are the source of high inhomogeneities on the micro level. These inhomogeneities may occur on different scales, see Figure 1.1.

The focus of this work is to study the effects of micro inhomogeneities of piezoelectric materials on macroscopic configurational forces. Special effort has been given on the configurational forces at certain defect situations. A sharp crack tip is considered as one of these defect situations. In order to fulfill the task of this research work, one has to deal with three fields of mechanics: electro-mechanically coupled piezoelectric materials; multiscale simulation, or computational homogenization of piezoelectric materials; and

configurational force theory. For a detailed knowledge of piezoelectric materials, the reader is referred to the text books by Xu [112] and Qin [80].

It is very difficult to capture the macroscopic material responses with the help of pre-assumed overall constitutive relations. To capture the overall macro material response of microscopically inhomogeneous material, some kind of homogenization techniques are to be used. There are several homogenization or multiscale techniques, e.g., asymptotic homogenization, semi-analytical homogenization, computational homogenization (FE^2-based or Fourier transformation based homogenization). The first two homogenization methods are only applicable to simple microstructures, while the last method (computational homogenization technique) is suitable for more complex situation. To capture the effect of the micro inhomogeneities in the configurational force on the macro level, one needs to homogenize the Eshelby stress tensor. Several approaches for the case of large deformation problem are proposed in Ricker et al. [84]. As large deformations are unlike for piezoelectric ceramics, a modified technique is used to obtain the homogenized Eshelby stress tensor in the case of small deformation. The node configurational forces represent the defect driving forces, e.g., the configurational force at a crack tip corresponds to the J-integral proposed by Rice in [82]. Thus, the magnitude of the configurational crack tip force yields a criterion whether a crack propagates depending on the underlying microscopic structure.
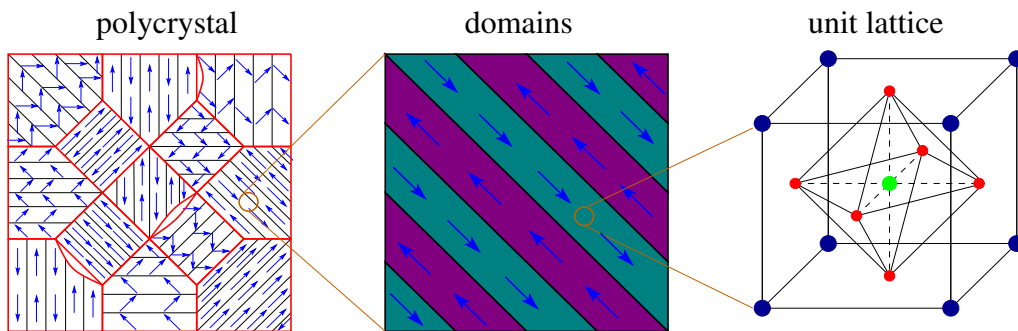
Figure 1.1: *Piezoelectric material on different scales*

1.2   State of the art

The rule of mixtures can simply be used to homogenize the moduli of inhomogeneous materials. Then the homogenized property is estimated by averaging over the corresponding properties of the microscopic components weighted by their volume fractions. This

method provides a rough estimate of the overall property by considering only a single microstructural characteristic, namely the volume fractions in the inhomogeneous material. This method does not include the influences of other microstructural characteristics. A technique is presented in Voigt [107] and Reuss [81] in order to estimate the upper and lower bounds of the macroscopic moduli. More accurate bounds for overall properties using a variational formulation are discussed in Hashin and Shtrikman [35, 36, 37].

A better technique is given in Eshelby [15], where the analytical solution of a boundary value problem of a spherical or an elliptical inclusion material in an infinite matrix is considered to determine the effective material parameters. This is the so called equivalent eigenstrain method. The extension of this method is the so called self-consistent method. In this method a particle of one phase is embedded into a material with unknown effective material properties. This approach is suitable for microstructures with regular geometry. This method is used for polycrystalline ceramics in the work by Kröner [50]. Readers are referred to Hashin [33, 34], Hill [39], Willis [110], etc. for more consultation on the self-consistent method. Another analytical homogenization method is presented in the article of Mori and Tanaka [68], Tanaka and Mori [102] and Benveniste [6] by using the mean-field approximation. This method is known as the Mori-Tanaka method.

An asymptotic homogenization procedure is outlined in Bensoussan et al. [5] and Sanchez-Palencia [85]. In this method an asymptotic expansion of the displacement and stress fields is applied on the ratio of a characteristic size of the heterogeneities and a measure of the microstructure, see Toledano and Murakami [103], Devries et al. [13], Suquet [100], Guedes and Kikuchi [30], Fish et al. [20]. This asymptotic homogenization method is suitable for the determination of effective overall properties as well as the local stress and strain quantities. The weakness of this method is that it is only applicable to a problem with simple micro domain and simple material models, generally for small deformations.

The so called unit cell methods are developed in order to handle the increasing inhomogeneities and complexities in the microstructures. These approaches are mentioned in different publications, e.g., Christman et al. [12], Bao et al. [4], Suresh et al. [101], Nakamura and Suresh [75], McHugh et al. [59], and so on. These unit cell methods are capable to supply valuable information on the local microstructural fields along with the homogenized material properties. The material properties are usually calculated by fitting the homogenized microscopical stress-strain fields, which are estimated from the analysis of a microstructural representative cell subjected under a certain loading, on macroscopically closed form phenomenological constitutive relations in a predetermined format. It is

severely difficult to prepare a suitable assumption for the macroscopic constitutive format if the material behavior shows nonlinearities. The unit cell method is used in the work of Poizat and Sester [78] and Li et al. [54], where effective properties of piezoelectric materials or composites are calculated.

Recently, an encouraging numerical method to homogenize the microscopically inhomogeneous engineering material has been developed, i.e. the multiscale computational homogenization. This approach is documented in the articles by Suquet [100], Guedes and Kikuchi [30], Terada and Kikuchi [104], Ghosh et al. [25, 26]; and further developed and improved in more recent years by Smit et al. [98], Miehe et al. [66, 67], Michel et al. [62], Feyel and Chaboche [19], Terada and Kikuchi [105], Ghosh et al. [27], Kouznetsova et al. [49], Miehe and Koch [65]. These micro-macro modeling methods evaluate the stress-strain at every point of interest on the macro level by an elaborate microstructural modeling attached to that macro point. This type of multiscale modeling does not necessitate a constitutive law on the macro level, and is capable to handle large deformation on the macro and on the micro levels. This method is suitable for any material law, physical nonlinearity and time dependency. The finite element method can be used to model the micro domain, see Smit et al. [98], Feyel and Chaboche [19], Terada and Kikuchi [105], and so on. If both macro and micro scales are simulated with the help of finite elements, the method is called FE^2-based computational homogenization. This is the interest of this research work. A detailed illustration of this approach can be found in Feyel [17, 18], Feyel and Chaboche [19], Miehe and Koch [65], Miehe [63, 64]. In the work of Ricker et al. [83, 84], a FE^2-based computational homogenization is used to homogenize the Eshelby stress tensor and the configurational forces. An application of this FE^2-based method towards the piezoelectric materials can be found in Schröder and Keip [92, 93, 94], Keip and Schröder [44]. In the work of Khalaquzzaman et al. [47], a FE^2-based homogenization technique is used in order to homogenize the configurational forces of piezoelectric materials. Few more numerical homogenization methods incorporating Voronoi cell methods are documented in publications of Ghosh et al. [25, 26], and methods based on fast Fourier transformation are presented in Fotiu and Nemat-Nasser [22], Moulinec and Suquet [69] and Miehe et al. [67].

A detailed survey of homogenization approaches can be found in the articles by Kanouté [43] and Geers et al. [24]. A comprehensive overview of homogenization methods is elaborated in the text books by Gross and Seelig [29] or Nemat-Nasser and Hori [76].

Primarily, the idea of the energy-momentum tensor to continuum mechanics of solids was discussed by Eshelby in Eshelby [14]. However, at that time the term energy-momentum tensor was not used. It was described as the Maxwell-tensor of elasticity. Later in Eshelby [16], the term energy-momentum tensor was introduced. Configurational force, which indicates the energy changes in a system, is a convenient tool to investigate the inhomogeneities or the fracture of solids. Further, this abstract physical quantity is also used in refinement of finite element meshes in Müller and Maugin [74], Müller et al. [73] and Braun [8]. To get a broad idea on configurational forces, the reader is referred to some well established text books, e.g., Maugin [58], Kienzler and Herrmann [48] and Gurtin [32].

The evolution of the microstructure of piezoelectric materials can be modeled by a sharp interface approach, or by a phase field approach. By modeling the domain wall with a sharp interface approach, a jump in certain material properties is introduced. As a result, the theory of configurational forces is applicable to the evolution of microstructures. In the work by Loge and Suo [56], a set of generalized coordinate systems was introduced to capture the geometry of the domain state, and a linear kinetic law, which is based on a variational principle, connects the rates of these coordinates to the conjugate driving force. The driving force is formulated within a thermodynamic framework in Kessler and Balke [45, 46], where the bending of domain walls is addressed. By using the driving force on the interface, a kinetic law for domain wall movement is postulated in Müller et al. [72] and Schrade et al. [88].

Phase field approaches regarding domain evolution in ferroelectric materials are discussed in Cao et al. [9], Wang et al. [109], Ahluwalia and Cao [1], Ahluwalia et al. [2], Choudhury et al. [10], Zhang and Bhattacharya [113], and Choudhury et al. [11]. A detailed numerical treatment of the complete set of equations of domain evolution is presented in Su and Landis [99], and Wang and Kamlah [108], where the finite element method is used. Phase field models, which incorporate the spontaneous polarization as the order parameter, are presented in Schrade et al [87, 89, 90].

1.3   Structure of the investigation

This research work is subdivided into six chapters. For the sake of completeness, a brief introduction of continuum mechanics and electrostatics is given in Chapter 2 and Chap-

ter 3, respectively. Section 2.1 - 2.4 gives a short overview of continuum mechanics in a large deformation setting. It covers kinematics of deformation, strain measures, stress measures and balance laws in continuum mechanics. Since piezoelectric materials exhibit only small deformation, in Section 2.5 kinematics of deformation, strain measures, stress measures, and balance laws are recast in a small strain setting. The theory of configurational forces is presented in Section 2.6

In Section 3.1 - 3.4 a short overview of the electric charge, Coulomb's law, the electric potential, and the electric polarization in vacuum are given. Section 3.5 provides a short overview of the corresponding formulation of electrostatics in matter.

The theory of piezoelectric materials is presented in Chapter 4. It provides the field equations and the constitutive law of piezoelectric materials which includes the electro-mechanical coupling. In Section 4.3 the numerical implementation of the boundary value problem (BVP) regarding piezoelectric materials is concisely discussed. A detailed derivation of configurational forces for piezoelectric materials and a brief description on the numerical treatment of configurational forces are presented in Section 4.4.

Chapter 5 provides a detailed formulation of the FE^2-based homogenization techniques in a small strain framework using the configurational force theory. All derivations presented in this chapter are given only for the mechanical response of the material. In Section 5.1.1 a new set of boundary conditions for the micro boundary value problem is derived. A detailed derivation and discussion of different homogenization techniques of the Eshelby stress tensor are presented in Section 5.2. At the end of this chapter, numerical results are presented. In particular, crack tip configurational forces on the macro level, which are determined by using different microstructures, are obtained. The investigations in this chapter play a supporting role in the homogenization of piezoelectric materials in the next chapter.

Chapter 6 provides a detailed description of the FE^2-based homogenization techniques of piezoelectric materials using the configurational force theory. An detailed discussion of admissible boundary conditions for the micro BVPs is presented in Section 6.1. The determination of homogenized material moduli of piezoelectric materials is given in Section 6.2. Numerical results regarding configurational forces at the crack tip are also presented. Different micro structures and different electrical loadings are considered. All simulations in this chapter are carried out using non-evolving or stationary microstructures.

The treatment of homogenization techniques of piezoelectric materials using evolving microstructures is given in Chapter 7. It provides the theoretical background of the influences of external loadings on the underlying microstructures of piezoelectric materials. The evolution of the microstructures is realized with the help of configurational forces in the micro domain. Numerical results of the macro electric displacement distribution, the scale of evolution in the micro structure, the hysteresis in piezoelectric materials on the macro level are presented in this chapter.

Chapter 8 delivers a short conclusion of this research work and recommendations on future topics.

Chapter 2

Basics of continuum mechanics

Continuum mechanics is an important branch of mechanics. It helps us to deal with material simulations and structural problems to capture the mechanical responses. In continuum mechanics the modeling of the material is done as continuous mass rather than as discrete particles. At the beginning of this chapter, a short overview of non-linear continuum mechanics will be provided. Afterwards all relevant relations for linear continuum mechanics will be reformulated. Several textbooks could be listed on the classical continuum mechanics. Without claiming completeness some of them are listed as reference for the readers: Holzapfel [40], Ogden [77], Haupt [38], Gurtin [31], Marsden and Hughes [57], Fung and Tong [23], Betten [7], Liu [55].

2.1 Kinematics of deformation

The transformation of a continuum body from a reference or undeformed configuration to the current or spatial configuration is represented in Figure 2.1. The symbols $\mathcal{B}_0$ and $\mathcal{B}$ represent the continuum body in the undeformed configuration and in the spatial configuration, respectively. The one-to-one non-linear mapping function $\boldsymbol{\chi}(\cdot)$ in Figure 2.1 defines the motions of a continuum body,

$$\mathbf{x} = \boldsymbol{\chi}(\mathbf{X}, t) \tag{2.1}$$

which maps material points (denoted by the position vector $\mathbf{X}$ in the undeformed configuration) to the points in the current configuration denoted by the position vector $\mathbf{x}$ at
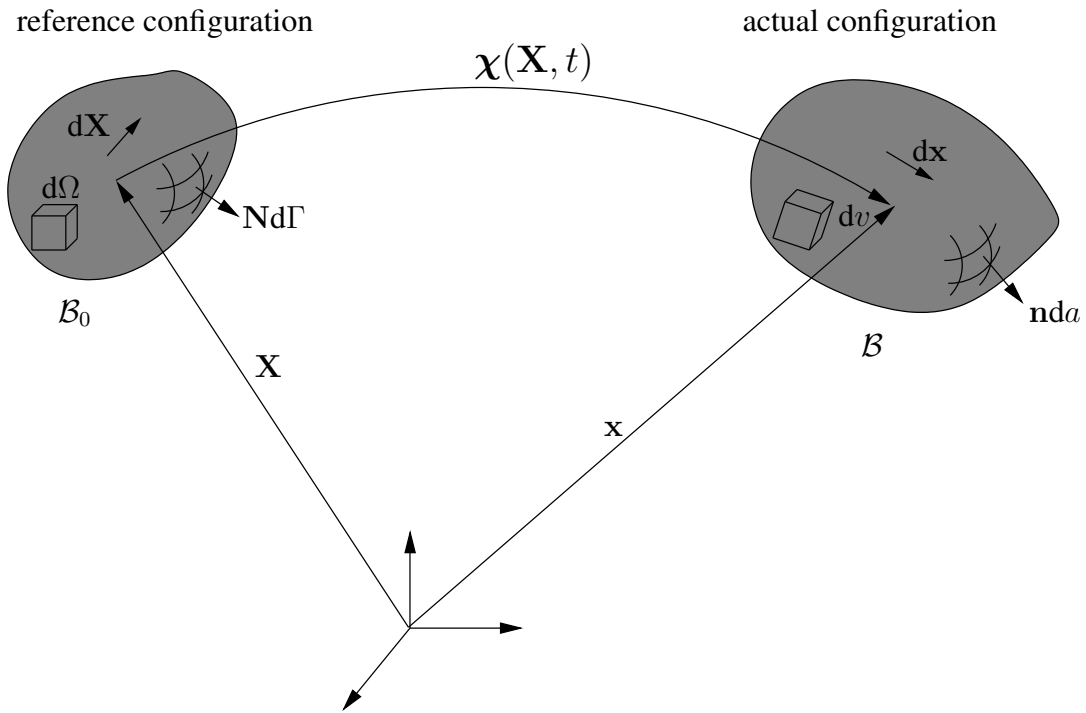
Figure 2.1: *Deformation map of reference to actual configuration*

time t. A line element $\mathrm{d}\mathbf{X}$ in the undeformed configuration is connected to a line element $\mathrm{d}\mathbf{x}$ in the spatial configuration through the deformation gradient $\mathbf{F}$,

$$\mathrm{d}\mathbf{x} = \mathbf{F}\mathrm{d}\mathbf{X} \qquad \text{with} \qquad \mathbf{F} = \frac{\partial \mathbf{x}}{\partial \mathbf{X}} = \mathrm{Grad}\mathbf{x}. \tag{2.2}$$

Therefore, the deformation gradient $\mathbf{F}$ maps the tangent spaces of the reference configuration to the tangent spaces of the current configuration.

The velocity $\mathbf{v}$ of a point of the deformed body is defined by the material time derivative of the position vector $\mathbf{x}$ on the current configuration,

$$\mathbf{v} = \frac{\mathrm{d}\mathbf{x}}{\mathrm{d}t} = \dot{\mathbf{x}} \quad \text{with} \quad \frac{\mathrm{d}(\cdot)}{\mathrm{d}t} = \left.\frac{\partial(\cdot)}{\partial t}\right|_{\mathbf{X}}. \tag{2.3}$$

By taking the material time derivative of the velocity $\mathbf{v}$, the acceleration can be formulated as

$$\mathbf{a} = \frac{\mathrm{d}\mathbf{v}}{\mathrm{d}t} = \dot{\mathbf{v}} = \ddot{\mathbf{x}}. \tag{2.4}$$

One can define the spatial velocity gradient l, which has an important role to describe motions as

$$\mathbf{l} = \text{grad}\mathbf{v} = \frac{\partial \mathbf{v}}{\partial \mathbf{x}} = \dot{\mathbf{F}}\mathbf{F}^{-1} = -\mathbf{F}\dot{\mathbf{F}}^{-1}. \tag{2.5}$$

To describe the transformation and the rate of a line element $\text{d}\mathbf{x}$, a surface element $\mathbf{n}\text{d}a$, and a volume element $\text{d}v$, the deformation gradient $\mathbf{F}$ and the spatial velocity gradient l are the required kinematic quantities. The relations are summarized as

$$\begin{aligned}
\text{d}\mathbf{x} &= \mathbf{F}\text{d}\mathbf{X}, & \dot{\text{d}\mathbf{x}} &= \mathbf{l}\text{d}\mathbf{x}, \\
\mathbf{n}\text{d}a &= J\mathbf{F}^{-T}\mathbf{N}\text{d}\Gamma, & (\mathbf{n}\text{d}a)\dot{} &= \left[(\text{div}\mathbf{v})\mathbf{1} - \mathbf{l}^T\right]\mathbf{n}\text{d}a, \\
\text{d}v &= J\text{d}\Omega, & \dot{\text{d}v} &= (\text{div}\mathbf{v})\text{d}v = (\text{tr}\mathbf{l})\text{d}v,
\end{aligned} \tag{2.6}$$

where J is the determinant of the Jacobian of the non-linear mapping, i.e. $J = \text{det}\mathbf{F}$.

2.2   Strain measures

With the help of the polar decomposition, it is possible to decompose the deformation gradient $\mathbf{F}$ in two ways: with a proper orthogonal rotation tensor $\mathbf{R}$ and a symmetric right stretch tensor $\mathbf{U}$, or with a symmetric left stretch tensor $\mathbf{V}$ and a rotation $\mathbf{R}$. The decomposition is done in the following way:

$$\mathbf{F} = \mathbf{R}\mathbf{U} = \mathbf{V}\mathbf{R}, \tag{2.7}$$

$$\text{with}\quad \mathbf{U} = \mathbf{U}^T,\quad \mathbf{V} = \mathbf{V}^T,\quad \mathbf{R}\mathbf{R}^T = \mathbf{1},\quad \text{det}\mathbf{R} = 1.$$

It is convenient to define the strain measures with the right and left stretch tensors $\mathbf{U}$ and $\mathbf{V}$. These stretch tensors are involved in the description of the deformation of a continuum body. Commonly used deformation tensors, which are based on $\mathbf{U}$ and $\mathbf{V}$, are given as example in the following:

$$\mathbf{C} = \mathbf{F}^T\mathbf{F} = \mathbf{U}^T\mathbf{U} = \mathbf{U}^2 \qquad \text{right Cauchy-Green tensor}, \tag{2.8}$$

$$\mathbf{b} = \mathbf{F}\mathbf{F}^T = \mathbf{V}\mathbf{V}^T = \mathbf{V}^2 \qquad \text{left Cauchy-Green tensor}. \tag{2.9}$$

In the undeformed or reference state $(\mathbf{F} = \mathbf{1})$, a strain measure should be zero. Making use of this idea leads to the introduction of the frequently used strain measures in the following:

$$\mathbf{E} = \frac{1}{2}(\mathbf{C} - \mathbf{1}) \qquad \text{Green-Lagrange strain tensor,}$$

(2.10)

$$\mathbf{e} = \frac{1}{2}(\mathbf{1} - \mathbf{b}^{-1}) \qquad \text{Euler-Almansi strain tensor.}$$

The Green-Lagrange and the Euler-Almansi strain tensor are related by deformation gradient $\mathbf{F}$ in the following way:

$$\mathbf{F}^T \mathbf{e} \mathbf{F} = \mathbf{E}.$$

(2.11)

Both strain tensors show the stretching of a line element of the continuum body in the reference configuration during deformation. This can be seen considering

$$\mathrm{d}s^2 - \mathrm{d}S^2 = \mathrm{d}\mathbf{x} \cdot \mathrm{d}\mathbf{x} - \mathrm{d}\mathbf{X} \cdot \mathrm{d}\mathbf{X} = \mathrm{d}\mathbf{X} \cdot (2\mathbf{E}\mathrm{d}\mathbf{X}) = \mathrm{d}\mathbf{x} \cdot (2\mathbf{e}\mathrm{d}\mathbf{x}).$$

(2.12)

The rate of change of a line element in the undeformed configuration can be expressed as

$$\frac{\mathrm{d}}{\mathrm{d}t}(\mathrm{d}s^2 - \mathrm{d}S^2) = 2\mathrm{d}\mathbf{x} \cdot (\mathbf{d}\mathrm{d}\mathbf{x}) = 2\mathrm{d}\mathbf{x} \cdot \left[(\dot{\mathbf{e}} + \mathbf{l}^T\mathbf{e} + \mathbf{e}\mathbf{l})\mathrm{d}\mathbf{x}\right] = 2\mathrm{d}\mathbf{X} \cdot (\dot{\mathbf{E}}\mathrm{d}\mathbf{X}),$$

(2.13)

where $\mathbf{d}$ denotes the symmetric part of the spatial velocity gradient which is defined by the additive split of $\mathbf{l}$ in the following way:

$$\mathbf{l} = \mathbf{d} + \mathbf{w} \quad \text{with} \quad \mathbf{d} = \frac{1}{2}(\mathbf{l} + \mathbf{l}^T) \quad \text{and} \quad \mathbf{w} = \frac{1}{2}(\mathbf{l} - \mathbf{l}^T).$$

(2.14)

2.3   Stress measures

Using the stress tensors $\boldsymbol{\sigma}$ and $\mathbf{P}$, the traction vectors $\mathbf{t}$ and $\mathbf{T}$, which are defined as force per area in the actual and reference configuration, respectively, can be formulated by a linear mapping of the normal vectors $\mathbf{n}$ and $\mathbf{N}$, respectively. The normal vectors $\mathbf{n}$ and $\mathbf{N}$ are also defined in the actual and reference configuration, respectively. As a consequence, one obtains

$$\mathbf{T}\mathrm{d}\Gamma = \mathbf{P}\mathbf{N}\mathrm{d}\Gamma = \mathbf{t}\mathrm{d}a = \boldsymbol{\sigma}\mathbf{n}\mathrm{d}a.$$

(2.15)

The stress tensors $\mathbf{P}$ and $\boldsymbol{\sigma}$ are named as the first Piola-Kirchhoff stress and the Cauchy stress tensor, respectively. As the first Piola-Kirchhoff stress tensor is in the actual and the

reference configurations, it is identified as a so called two field tensor. On the other hand, the Cauchy stress tensor is defined completely in the actual configuration and shows the symmetry property $\boldsymbol{\sigma} = \boldsymbol{\sigma}^T$ for a simple continuum. With the help of (2.6_3) these two stress tensors can be related in the following way:

$$\mathbf{P} = J\boldsymbol{\sigma}\mathbf{F}^{-T}, \tag{2.16}$$

and the following identity is established by using the symmetry property of the Cauchy stress tensor

$$\mathbf{P}\mathbf{F}^T = \mathbf{F}\mathbf{P}^T. \tag{2.17}$$

The first Piola-Kirchhoff stress tensor does not have the symmetry property as the Cauchy stress tensor. For that reason, the second Piola-Kirchhoff stress tensor $\mathbf{S}$ is introduced to obtain a symmetric stress measure defined in the reference configuration. The second Piola-Kirchhoff stress tensor can be defined by

$$\mathbf{S} = \mathbf{F}^{-1}\mathbf{P} = J\mathbf{F}^{-1}\boldsymbol{\sigma}\mathbf{F}^{-T} \quad \text{yielding} \quad \mathbf{S} = \mathbf{S}^T. \tag{2.18}$$

2.4 Balance laws

The concept of balance laws plays an important role in the understanding of continuum mechanics as well as the theory of configurational forces. In continuum mechanics five balance laws need to be formulated, namely the balance of mass, of linear momentum, of angular momentum, of energy, and of entropy. Any balance law listed here has the generalized structure

$$\frac{\mathrm{d}}{\mathrm{d}t} \int_{\mathcal{B}_0} \varphi \mathrm{d}\Omega = \int_{\partial\mathcal{B}_0} \boldsymbol{\Phi} \cdot \mathbf{N} \mathrm{d}\Gamma + \int_{\mathcal{B}_0} r_\varphi \mathrm{d}\Omega, \tag{2.19}$$

where φ is the quantity which needs to be balanced, r_φ is the supply/production of φ and $\boldsymbol{\Phi}$ is the flux of φ. Equation (2.19) is stated for a control volume $\mathcal{B}_0$ (in the undeformed configuration). Therefore, it is termed as a global balance law. Equation (2.19) can be transformed to its local form with the help of the Gauß theorem in the following way:

$$\dot{\varphi} = \mathrm{Div}\boldsymbol{\Phi} + r_\varphi. \tag{2.20}$$

The mass balance, or precisely termed as the conservation of mass, can be written in global and local form in the reference or in the undeformed configuration by

$$\frac{\mathrm{d}}{\mathrm{d}t} \int_{\mathcal{B}_0} \rho_0 \mathrm{d}\Omega = 0 \quad \text{or} \quad \dot{\rho}_0 = 0, \tag{2.21}$$

respectively. Here ρ_0 denotes the mass density of the continuum in the reference configuration. By making use of (2.6_5), the mass density in the reference configuration ρ_0 and the density in the current configuration ρ can be related by

$$\int_{\mathcal{B}_0} \rho_0 \mathrm{d}\Omega = \int_{\mathcal{B}} \rho \mathrm{d}v \quad \Rightarrow \quad \rho_0 = \rho J. \tag{2.22}$$

The balance of linear momentum is expressed by

$$\frac{\mathrm{d}}{\mathrm{d}t} \int_{\mathcal{B}_0} \rho_0 \mathbf{v} \mathrm{d}\Omega = \int_{\partial\mathcal{B}_0} \mathbf{PN} \mathrm{d}\Gamma + \int_{\mathcal{B}_0} \mathbf{f} \mathrm{d}\Omega \tag{2.23}$$

in the global form, and in the local form it is defined by

$$\rho_0 \dot{\mathbf{v}} = \mathrm{Div}\mathbf{P} + \mathbf{f}, \tag{2.24}$$

where $\mathbf{f}$ expresses the body forces which are defined per volume in the reference configuration.

In the static condition the inertia terms can be neglected. As a result, this leads to the equilibrium conditions in the global and local form

$$\int_{\partial\mathcal{B}_0} \mathbf{PN} \mathrm{d}\Gamma + \int_{\mathcal{B}_0} \mathbf{f} \mathrm{d}\Omega = \mathbf{0}, \tag{2.25}$$

and

$$\mathrm{Div}\mathbf{P} + \mathbf{f} = \mathbf{0}, \tag{2.26}$$

respectively.

The following balance law in the global form

$$\frac{\mathrm{d}}{\mathrm{d}t} \int_{\mathcal{B}_0} \mathbf{x} \times (\rho_0 \mathbf{v}) \mathrm{d}\Omega = \int_{\partial\mathcal{B}_0} \mathbf{x} \times (\mathbf{PN}) \mathrm{d}\Gamma + \int_{\mathcal{B}_0} \mathbf{x} \times \mathbf{f} \mathrm{d}\Omega \tag{2.27}$$

holds for the angular momentum. The global balance of angular momentum leads to the equation (2.17) in the local form, which is analogous to the symmetry of the Cauchy stress tensor $\boldsymbol{\sigma} = \boldsymbol{\sigma}^T$.

The balance of energy for a control volume in the reference configuration is expressed by

$$\frac{\mathrm{d}}{\mathrm{d}t} \int_{\mathcal{B}_0} \rho_0 (e + \frac{1}{2}\mathbf{v}\cdot\mathbf{v})\mathrm{d}\Omega = \int_{\partial\mathcal{B}_0} (\mathbf{PN})\cdot\mathbf{v}\mathrm{d}\Gamma + \int_{\mathcal{B}_0} \mathbf{f}\cdot\mathbf{v}\mathrm{d}\Omega - \int_{\partial\mathcal{B}_0} \mathbf{Q}\cdot\mathbf{N}\mathrm{d}\Gamma + \int_{\mathcal{B}_0} r\mathrm{d}\Omega, \quad (2.28)$$

where e, $\mathbf{Q}$ and r are the internal energy, the heat flux and source, respectively. The energy balance in the local form can be written as

$$\rho_0 \dot{e} = \mathbf{P} : \dot{\mathbf{F}} - \mathrm{Div}\mathbf{Q} + r. \tag{2.29}$$

The balance of entropy in the global form can be written as

$$\frac{\mathrm{d}}{\mathrm{d}t} \int_{\mathcal{B}_0} \rho_0 s \mathrm{d}\Omega = -\int_{\partial\mathcal{B}_0} \frac{\mathbf{Q}}{T} \cdot \mathbf{N}\mathrm{d}\Gamma + \int_{\mathcal{B}_0} \frac{r}{T}\mathrm{d}\Omega + \int_{\mathcal{B}_0} \Pi_s \mathrm{d}\Omega, \tag{2.30}$$

where s is the entropy of the system, the entropy flux is given by $\mathbf{Q}/T$ and the entropy source by r/T, with T the absolute temperature. The entropy production is designated by Π_s. The entropy s determines the direction in which thermodynamic processes take place. The local form of the entropy balance is written as

$$\rho_0 \dot{s} = -\mathrm{Div}\left(\frac{\mathbf{Q}}{T}\right) + \frac{r}{T} + \Pi_s. \tag{2.31}$$

From the second law of thermodynamics, it can be inferred that the entropy production Π_s has always a non-negative value,

$$\Pi_s \geq 0. \tag{2.32}$$

To deal with the purely mechanical theory of a system, the elimination of the heat flux $\mathbf{Q}$ and the heat production r in equations (2.28) and (2.30) or in equations (2.29) and (2.31) is to be done by introducing the free Helmholtz energy w. It is assumed that the changes in the state of the system are isothermal. As a result, the reduced dissipation inequality

$$\mathcal{D} = \Pi_s T = \mathbf{P} : \dot{\mathbf{F}} - \rho_0 \dot{w} \geq 0 \quad \text{with} \quad w = e - Ts \tag{2.33}$$

is obtained.

A free Helmholtz energy per volume in the reference or undeformed configuration is expressed by

$$W = \rho_0 w, \tag{2.34}$$

where W is also denoted as strain energy. The strain energy W can be considered as a potential for the stress measures because of the following equations:

$$\mathbf{P} = \frac{\partial W}{\partial \mathbf{F}} \quad \text{or} \quad \mathbf{S} = \frac{\partial W}{\partial \mathbf{E}} = 2\frac{\partial W}{\partial \mathbf{C}}. \tag{2.35}$$

2.5   Small deformations

The basics of continuum mechanics presented in the previous sections enable us to introduce the basic theory of configurational forces in the large strain framework. Since in piezoelectric materials there are only small deformations, it is not necessary to use the large strain formulation. In this situation a geometrically linear theory of continuum body serves the purpose. The central idea to derive the kinematically linear theory is based on the assumption that the current and the reference configuration approximately coincide. This assumption may create confusions when formulating the configurational force theory, as it is founded on changes of the continuum body in the reference configuration. On the other hand, the classical physical forces are based on changes in the actual configuration. In the case of large strain theory, a material point is denoted by its position in the undeformed configuration $\mathbf{X}$ (name of the particle). In small deformation setting a material point is designated just by its position or its coordinates $\mathbf{x}$. The displacement vector $\mathbf{u}$ defined by

$$\mathbf{u} = \mathbf{x} - \mathbf{X} \tag{2.36}$$

plays an important role as an essential kinematic descriptor in this theory. Within small strain theory, all stress and strain measures become identical. The linearized strain $\boldsymbol{\varepsilon}$ is defined as

$$\boldsymbol{\varepsilon} = \frac{1}{2}(\nabla \mathbf{u} + (\nabla \mathbf{u})^T), \tag{2.37}$$

and the stress tensor is denoted by $\boldsymbol{\sigma}$. The velocity $\mathbf{v}$ is defined as $\dot{\mathbf{u}}$. According to the small deformation setting it is not required to have two different control volumes in the reference and in the actual configuration. Furthermore no distinction between ρ and ρ_0 is required. The density is simply denoted by ρ in the following.

One can present all previous balance laws for small strain (geometric linear) setting in a short list,

1. conservation of mass

$$\rho = \text{const.}, \tag{2.38}$$

2. balance of linear momentum

$$\frac{\mathrm{d}}{\mathrm{d}t} \int_{\mathcal{B}} \rho \dot{\mathbf{u}} \mathrm{d}\Omega = \int_{\partial \mathcal{B}} \boldsymbol{\sigma} \mathbf{n} \mathrm{d}\Gamma + \int_{\mathcal{B}} \mathbf{f} \mathrm{d}\Omega \tag{2.39}$$

or

$$\rho \ddot{\mathbf{u}} = \text{div} \boldsymbol{\sigma} + \mathbf{f}, \tag{2.40}$$

3. balance of angular momentum

$$\frac{\mathrm{d}}{\mathrm{d}t} \int_{\mathcal{B}} \mathbf{x} \times (\rho \dot{\mathbf{u}}) \mathrm{d}\Omega = \int_{\partial \mathcal{B}} \mathbf{x} \times (\boldsymbol{\sigma} \mathbf{n}) \mathrm{d}\Gamma + \int_{\mathcal{B}} \mathbf{x} \times \mathbf{f} \mathrm{d}\Omega \tag{2.41}$$

or

$$\boldsymbol{\sigma} = \boldsymbol{\sigma}^T, \tag{2.42}$$

4. balance of energy

$$\frac{\mathrm{d}}{\mathrm{d}t} \int_{\mathcal{B}} \rho \left(e + \frac{1}{2} |\dot{\mathbf{u}}|^2 \right) \mathrm{d}\Omega = \int_{\partial \mathcal{B}} (\boldsymbol{\sigma} \mathbf{n}) \cdot \dot{\mathbf{u}} \mathrm{d}\Gamma + \int_{\mathcal{B}} \mathbf{f} \cdot \dot{\mathbf{u}} \mathrm{d}\Omega - \int_{\partial \mathcal{B}} \mathbf{Q} \cdot \mathbf{n} \mathrm{d}\Gamma + \int_{\mathcal{B}} r \mathrm{d}\Omega \tag{2.43}$$

or

$$\rho \dot{e} = \boldsymbol{\sigma} : \dot{\boldsymbol{\varepsilon}} - \text{div} \mathbf{Q} + r, \tag{2.44}$$

5. balance of entropy

$$\frac{\mathrm{d}}{\mathrm{d}t} \int_{\mathcal{B}} \rho s \mathrm{d}\Omega = -\int_{\partial \mathcal{B}} \frac{\mathbf{Q}}{T} \cdot \mathbf{n} \mathrm{d}\Gamma + \int_{\mathcal{B}} \frac{r}{T} \mathrm{d}\Omega + \int_{\mathcal{B}} \Pi_s \mathrm{d}\Omega \tag{2.45}$$

or

$$\rho \dot{s} = -\text{div} \left(\frac{\mathbf{Q}}{T} \right) + \frac{r}{T} + \Pi_s, \tag{2.46}$$

6. second law of thermodynamics

$$\Pi_s \geq 0. \tag{2.47}$$

The reduced dissipation inequalities becomes

$$\mathcal{D} = \boldsymbol{\sigma} : \dot{\boldsymbol{\varepsilon}} - \dot{W} \geq 0, \tag{2.48}$$

which leads by standard arguments to the conclusion that

$$\boldsymbol{\sigma} = \frac{\partial W}{\partial \boldsymbol{\varepsilon}}. \tag{2.49}$$

2.6   Configurational forces

The theory of configurational forces provides a convenient mechanism to investigate different kinds of material defects. In the literature configurational forces are also called material forces. This theory provides an unified approach to investigate defects and processes that bring changes in the material structure. It is frequently applied in the fields of fracture mechanics and phase transformations.

The theory of configurational forces with appropriate formulations can be used to model point, line, area and volume defects. Physically point defects may represent interstitial atoms or vacancies (centers of dilatation); dislocation lines may be considered as line defects; interfaces may be represented as area defects; and inclusions may be modeled as volume defects. Configurational forces play an important role in the analysis of morphology changes, which is very important for material science, as the macro constitutive response is greatly affected by the arrangement and evolution in the microstructures, see e.g., Müller and Gross [70, 71]. Driving forces are formulated with the consideration of the change of the total potential with respect to a virtual motion of the defect in the reference configuration. This fact is used in all applications of configurational forces. The material or configurational forces in continuum mechanics were introduced by Eshelby in the early fifties of the last century. In Eshelby [14] the driving forces on elastic singularities were evaluated via a second-order tensor (at that time Eshelby did use the term 'Maxwell tensor of elasticity'). Eshelby proved that the negative gradient of the total potential with respect to the position of the defect can be suitably used for the evaluation of material imperfections.

2.6.1   Theory of configurational forces

The theory of configurational forces, which is presented in the following, follows the introductory ideas stated in Eshelby [14, 16]. For a concise derivation only elastic materials are taken into consideration, but an extension of this derivation is possible for inelastic settings and has been discussed elaborately in Maugin [58]. For the theoretical analysis our attention is restricted to the quantities that are defined with respect to the material configuration in an effort to make the derivations more condensed. There exists a strain energy function

$$W = \hat{W}(\mathbf{F}, \mathbf{X}) \tag{2.50}$$

per unit volume of a hyper-elastic material in the reference configuration. An assumption is made that W depends on the deformation gradient $\mathbf{F}$ and explicitly on the position vector $\mathbf{X}$ (in the reference configuration). The second dependency is taken into account in order to be able to consider heterogeneity in the material. The first Piola-Kirchoff stress tensor is calculated by

$$\mathbf{P} = \frac{\partial \hat{W}}{\partial \mathbf{F}}. \tag{2.51}$$

For static conditions the balance of momentum (2.23) can be written in its local form as

$$\mathrm{Div}\mathbf{P} + \mathbf{f} = \mathbf{0}, \tag{2.52}$$

see equation (2.26). The vector $\mathbf{f}$ denotes body forces (defined per unit volume of the reference configuration). One can express the material gradient of the strain energy function W as in the following

$$
\begin{aligned}
\mathrm{Grad}W &= \mathbf{P} : \mathrm{Grad}\mathbf{F} + \left.\frac{\partial \hat{W}}{\partial \mathbf{X}}\right|_{\mathrm{expl.}} \\[2mm]
&= \mathrm{Div}(\mathbf{F}^T\mathbf{P}) - \mathbf{F}^T\mathrm{Div}\mathbf{P} + \left.\frac{\partial \hat{W}}{\partial \mathbf{X}}\right|_{\mathrm{expl.}}.
\end{aligned}
\tag{2.53}
$$

The first term on the RHS of (2.53$_1$) can be expressed in index notation by $P_{iJ}F_{iJ,K}$. The subscript expl. appearing for the first time in the second term in (2.53$_1$) indicates the explicit derivative of $\hat{W}$ with respect to the position $\mathbf{X}$. Mathematical manipulations and in-

corporation of the mechanical equilibrium condition (2.52) and kinematics $\mathbf{F} = \partial \mathbf{x} / \partial \mathbf{X}$ lead to an equation for the material forces in the form

$$\mathrm{Div}\,\mathbf{\Sigma} + \mathbf{g} = \mathbf{0}, \tag{2.54}$$

where the Eshelby stress tensor or the energy-momentum tensor is defined by

$$\mathbf{\Sigma} = W\mathbf{1} - \mathbf{F}^T\mathbf{P}, \tag{2.55}$$

and the configurational force

$$\mathbf{g} = -\mathbf{F}^T\mathbf{f} - \left.\frac{\partial \hat{W}}{\partial \mathbf{X}}\right|_{\mathrm{expl.}} \tag{2.56}$$

is introduced in order to obtain a similar structure as that of equation (2.52). With the definition of the symmetric Piola-Kirchhoff stress tensor in (2.18) and the symmetric right Cauchy-Green tensor in (2.8), equation (2.55) can be expressed as

$$\mathbf{\Sigma} = W\mathbf{1} - \mathbf{C}\mathbf{S}, \quad \text{thus,} \quad \mathbf{\Sigma}\mathbf{C} = \mathbf{C}\mathbf{\Sigma}^T. \tag{2.57}$$

The last expression in equation (2.57) can be considered as the symmetry of the Eshelby stress tensor $\mathbf{\Sigma}$ with respect to right Cauchy-Green tensor $\mathbf{C}$. From (2.56) an important realization can be drawn: if a continuum body is homogeneous and it does not contain any body forces, the divergence of the Eshelby stress tensor disappears, and that leads to

$$\mathrm{Div}\mathbf{\Sigma} = \mathbf{0}. \tag{2.58}$$

It can be stated that the Eshelby stress tensor satisfies a conservation law strictly within the continuum body. For an elaborate discussion of conservation laws of the Eshelby stress tensor, Kienzler and Herrmann [48] can be consulted.

2.6.2   Configurational forces in small deformation

In the previous section the configurational forces for large deformation problems are described. Since the piezoelectric materials investigated in this work exhibit primarily small deformation, a brief description of the configurational forces for the small deformation

setting will be discussed. The concept of configurational forces within a small deformation framework is a bit confusing, as the current configuration coincides with reference configuration in a small deformation framework.

Similar to large deformations, one can write the balance of configurational forces for small deformation problems as

$$\text{div}\,\boldsymbol{\Sigma} + \mathbf{g} = \mathbf{0}. \tag{2.59}$$

The Eshelby stress tensor is defined as

$$\boldsymbol{\Sigma} = W\mathbf{1} - (\nabla\mathbf{u})^T\boldsymbol{\sigma}, \tag{2.60}$$

and volume configurational forces are defined as

$$\mathbf{g} = -(\nabla\mathbf{u})^T\mathbf{f} - \left.\frac{\partial\hat{W}}{\partial\mathbf{x}}\right|_{\text{expl.}}. \tag{2.61}$$

For a complete derivation of the balance of configurational forces, the Eshelby stress tensor and the volume configurational forces in a small deformation framework, the reader is referred to Kienzler and Herrmann [48] and Müller et al. [73].

Chapter 3

Basics of electrostatics

Electrostatics is an important field of study in physical science incorporating the properties and phenomena of static charges, or of charges with slow movement and in the absence of acceleration. In this chapter a very short overview of electrostatics is presented, where electrodynamics and magnetic behavior of moving charges are neglected. Textbooks on the theories of electrostatics and -dynamics include Landau and Lifshitz [51, 52], Purcell [79] and Jackson [42]; a brief summary can be found in Schrade [86], Goy [28] and Mehling [61].

3.1 Electric charge

Electric charge, which has an influence on electromagnetic interaction, is a conserved property of particles. Modern experiments show that the electric charge is a quantized quantity. Being a quantized quantity, it can only contain values of integer multiples of the elementary charge $e \approx 1.60217646 \cdot 10^{-19}$ C. The proton and the electron have the charge of e and $-e$, respectively. Due to the additive feature, N electrically charged particles with individual charges q_i have the total charge

$$q = \sum_{i=1}^{N} q_i. \tag{3.1}$$

The discrete charges q_i need to be substituted by charge density to obtain a continuum description of electric charge. The charge density on the microscopic level of N point charges can be written as

$$\rho_{\text{mic}}(\mathbf{x}) = \sum_{i=1}^{N} q_i \delta(\mathbf{x} - \mathbf{x}_i), \tag{3.2}$$

where $\delta(\cdot)$ is the Dirac delta function, $\mathbf{x}_i$ is the position vector of the point charge q_i. The total amount of electric charges in a representative volume V^{R} can be determined as sketched in Figure 3.1

$$Q = \int_{V^{\text{R}}} \rho_{\text{mic}}(\bar{\mathbf{x}}) d\Omega = \sum_{i=1}^{N} q_i. \tag{3.3}$$

The volume average of the micro charge density ρ_{mic} in equation (3.2) over a representative volume V^{R} can be used to define the continuous and bounded charge density

$$\rho(\mathbf{x}) = \frac{Q}{V^{\text{R}}} = \frac{1}{V^{\text{R}}} \sum_{i=1}^{N} q_i. \tag{3.4}$$

Analogously, the surface charge density ω is expressed as

$$\omega(\mathbf{x}) = \frac{1}{A^{\text{R}}} \sum_{i=1}^{N_{\text{s}}} q_i, \tag{3.5}$$

where A^{R} is a representative surface area and N_{s} is the total number of point charges on that surface.
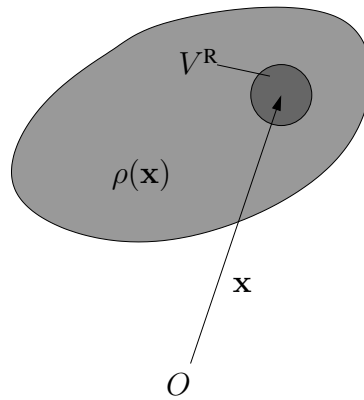
Figure 3.1: *A representative volume element V^R around the point* $\mathbf{x}$ *in electrically charged continuum body*

3.2   Coulomb's law

Coulomb's law determines the electrostatic interacting force between point charges. The interacting force is expressed as

$$\mathbf{F}_{12} = \frac{q_1 q_2}{4\pi\epsilon_0} \frac{\mathbf{x}_2 - \mathbf{x}_1}{|\mathbf{x}_2 - \mathbf{x}_1|^3}, \tag{3.6}$$

where $\mathbf{F}_{12}$ is the force exerted by a charge q_1 on another charge q_2 (Figure 3.2(a)). The electric constant ϵ_0 has a value of $8.854 \cdot 10^{-12}$C/(Vm). Newton's third law of motion is also applicable to the electrostatic forces, which gives, $\mathbf{F}_{12} = -\mathbf{F}_{21}$.

If a charge q_0 with a position $\mathbf{x}$ (Figure 3.2(b)) interacts with a system of N point charges with positions $\mathbf{x}_i$, then the resultant force acting on the test charge is expressed as

$$\mathbf{F}_0(\mathbf{x}) = \sum_{i=1}^{N} \frac{q_i q_0}{4\pi\epsilon_0} \frac{\mathbf{x} - \mathbf{x}_i}{|\mathbf{x} - \mathbf{x}_i|^3}. \tag{3.7}$$

In the case of a charge density ρ (see Figure 3.2(c)), the force exerted by the charge density within a body $\mathcal{B}$ on a charge q_0 can be written as

$$\mathbf{F}_0(\mathbf{x}) = q_0 \int_{\mathcal{B}} \frac{\rho}{4\pi\epsilon_0} \frac{\mathbf{x} - \mathbf{x}_i}{|\mathbf{x} - \mathbf{x}_i|^3} \mathrm{d}\Omega. \tag{3.8}$$
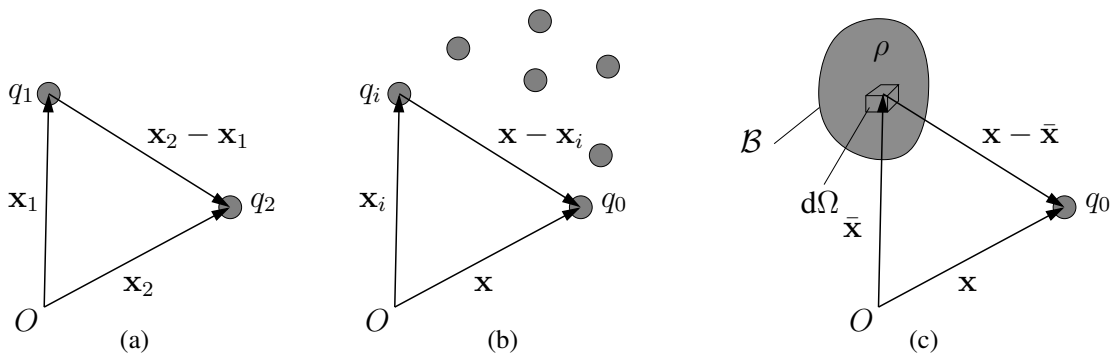
Figure 3.2: *Formulation of Coulomb's law (a) & (b) for point charges and (c) for charge densities*

The electric field is defined as the electrostatic force acted on a unit point charge. Equations (3.7) and (3.8) lead to the expression of the electric field $\mathbf{E}$ due to a system of point charges and a charged continuous body

$$\mathbf{E}(\mathbf{x}) = \sum_{i=1}^{N} \frac{q_i}{4\pi\epsilon_0} \frac{\mathbf{x} - \mathbf{x}_i}{|\mathbf{x} - \mathbf{x}_i|^3} \quad \text{and} \quad \mathbf{E}(\mathbf{x}) = \int_{\mathcal{B}} \frac{\rho}{4\pi\epsilon_0} \frac{\mathbf{x} - \mathbf{x}_i}{|\mathbf{x} - \mathbf{x}_i|^3} d\Omega, \tag{3.9}$$

respectively.

3.3   Work and electric potential

As the electric field is a conservative quantity, it can be expressed by a scalar potential field

$$\mathbf{E}(\mathbf{x}) = -\nabla\varphi(\mathbf{x}), \tag{3.10}$$

where $\nabla\varphi$ expresses the gradient of the electric potential. The electrostatic force on a charge is expressed as

$$\mathbf{F}_0 = q_0\mathbf{E}. \tag{3.11}$$

In order to move a charge q_0 from a point P with position vector $\mathbf{x}_P$ to another point L with position vector $\mathbf{x}_L$ along an arbitrary path Γ, the following work is required

$$W_P^L = -\int_{\Gamma} \mathbf{F}_0 \cdot d\mathbf{s} = -q_0 \int_{\Gamma} \mathbf{E} \cdot d\mathbf{s} \tag{3.12}$$

$$= q_0 \int_{\Gamma} \nabla\varphi(\mathbf{x}) \cdot d\mathbf{s} = q_0(\varphi(\mathbf{x}_P) - \varphi(\mathbf{x}_L)). \tag{3.13}$$

The scalar field φ is named the electric potential and is unique up to a constant which is often set to zero. The electric potential for the system of point charges depicted in Figure 3.2(b) is

$$\varphi(\mathbf{x}) = \sum_{i=1}^{N} \frac{q_i}{4\pi\epsilon_0 |\mathbf{x} - \mathbf{x}_i|}, \tag{3.14}$$

and the electric potential for the charge distribution shown in Figure 3.2(c) is given by

$$\varphi(\mathbf{x}) = \int_{\mathcal{B}} \frac{\rho(\bar{\mathbf{x}})}{4\pi\epsilon_0 |\mathbf{x} - \bar{\mathbf{x}}|} d\Omega. \tag{3.15}$$

The total potential energy of a system of point charges considering only its own electric field is given by

$$U = \frac{1}{2} \sum_{i=1}^{N} \sum_{\substack{j=1 \\ i \neq j}}^{N} \frac{q_i q_j}{4\pi\epsilon_0 \, |\mathbf{x}_i - \mathbf{x}_j|}, \tag{3.16}$$

and equation (3.16) can be written using the definition of the potential in (3.14) as

$$U = \frac{1}{2} \sum_{i=1}^{N} q_i \varphi(\mathbf{x}_i). \tag{3.17}$$

In the case of a charge distribution, the total potential can be written as

$$U = \frac{1}{2} \int_{\mathcal{B}} \int_{\mathcal{B}} \frac{\rho(\bar{\mathbf{x}})\rho(\tilde{\mathbf{x}})}{4\pi\epsilon_0 \, |\tilde{\mathbf{x}} - \bar{\mathbf{x}}|} \mathrm{d}\tilde{\Omega}\mathrm{d}\bar{\Omega} \tag{3.18}$$

and similarly, equation (3.18) can be written by using the definition of the potential in (3.15) as

$$U = \frac{1}{2} \int_{\mathcal{B}} \varphi(\bar{\mathbf{x}})\rho(\bar{\mathbf{x}})\mathrm{d}\bar{\Omega}. \tag{3.19}$$

The total potential energy of a collection of N discrete charges placed in an external electric potential field φ_{ext} is

$$U_{\mathrm{ext}} = \sum_{i=1}^{N} q_i \varphi_{\mathrm{ext}}(\mathbf{x}_i), \tag{3.20}$$

where the effect of the electric fields due to the charges q_i of the system is not considered. For a charge distribution, the total potential can be expressed by

$$U_{\mathrm{ext}} = \frac{1}{2} \int_{\mathcal{B}} \varphi_{\mathrm{ext}}(\bar{\mathbf{x}})\rho(\bar{\mathbf{x}})\mathrm{d}\bar{\Omega}. \tag{3.21}$$

Gauß law:
From equation (3.15) it follows that

$$\Delta\varphi(\mathbf{x}) = \frac{1}{\epsilon_0} \int_{\mathcal{B}} \rho(\bar{\mathbf{x}})\Delta\frac{1}{4\pi \, |\mathbf{x} - \bar{\mathbf{x}}|}\mathrm{d}\Omega = -\frac{1}{\epsilon_0} \int_{\mathcal{B}} \rho(\bar{\mathbf{x}})\delta(\mathbf{x} - \bar{\mathbf{x}})\mathrm{d}\Omega = -\frac{\rho(\mathbf{x})}{\epsilon_0}, \tag{3.22}$$

where Δ is the Laplace operator.

Multiplying equation (3.22) with $-\epsilon_0$ and considering the definition of electric field in equation (3.10) leads to the Gauß law

$$\epsilon_0 \mathrm{div}\mathbf{E}(\mathbf{x}) = \rho(\mathbf{x}). \tag{3.23}$$

It can be inferred from equation (3.10) that $\mathbf{E}$ is a curl free field:

$$\mathrm{curl}\mathbf{E}(\mathbf{x}) = \mathbf{0}. \tag{3.24}$$

Equations (3.23) and (3.24) (containing the electric field), or equations (3.10) and (3.22) (in terms of the electric potential) are the field equations of electrostatics.

3.4 Multipole expansion and polarization

A charge distribution ρ in the body $\mathcal{B}$ is shown in Figure 3.3. The vector $\boldsymbol{\eta}$ expresses the position vectors in $\mathcal{B}$, the vector $\mathbf{x}_0$ is the position vector of a fixed point in $\mathcal{B}$, and an arbitrary point far away from $\mathcal{B}$ is denoted by the position vector $\mathbf{x}$. The total electric
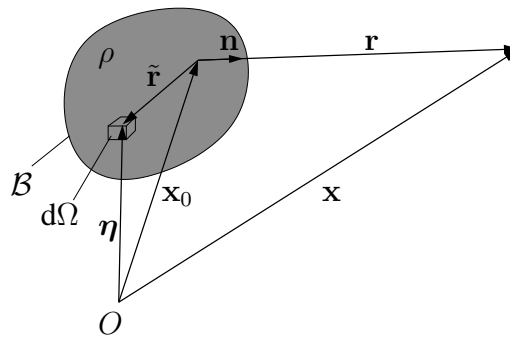
Figure 3.3: *Multipole expansion of a charge distribution*

potential stored in the body due to the charge distribution in equation (3.15) reads

$$\varphi(\mathbf{x}) = \int_{\mathcal{B}} \frac{\rho(\tilde{\mathbf{r}})}{4\pi\epsilon_0 \, |\mathbf{r} - \tilde{\mathbf{r}}|} \mathrm{d}\Omega = \frac{1}{4\pi\epsilon_0 r} \int_{\mathcal{B}} \rho\sqrt{(1+\alpha)^{-1}} \mathrm{d}\Omega, \tag{3.25}$$

where α is defined as $r^{-2}(\tilde{r}^2 - 2\mathbf{r}\cdot\tilde{\mathbf{r}}) \ll 1$; the vectors $\mathbf{r} = \mathbf{x} - \mathbf{x}_0 = r\mathbf{n}$ and $\tilde{\mathbf{r}} = \boldsymbol{\eta} - \mathbf{x}_0 = \tilde{r}\tilde{\mathbf{n}}$ are defined in such a way that $\mathbf{x} - \boldsymbol{\eta} = \mathbf{r} - \tilde{\mathbf{r}}$. The multipole expansion of φ in equation (3.25) can be written as

$$\varphi(\mathbf{x}) = \frac{1}{4\pi\epsilon_0}\left[\frac{1}{r}\int_{\mathcal{B}}\rho(\tilde{\mathbf{r}})\mathrm{d}\Omega + \frac{\mathbf{n}}{r^2}\cdot\int_{\mathcal{B}}\rho(\tilde{\mathbf{r}})\tilde{\mathbf{r}}\mathrm{d}\Omega + \frac{\mathbf{n}\otimes\mathbf{n}}{2r^3}:\int_{\mathcal{B}}\rho(\tilde{\mathbf{r}})(3\tilde{\mathbf{r}}\otimes\tilde{\mathbf{r}} - \tilde{r}\mathbf{1})\mathrm{d}\Omega + ...\right] \quad (3.26)$$

by using the Taylor series expansion of $\sqrt{(1+\alpha)^{-1}}$ with respect to α around $\alpha = 0$. The Taylor expansion of $(1+\alpha)^{-\frac{1}{2}}$ is $1 - \frac{1}{2}\alpha + \frac{3}{8}\alpha^2 - \frac{5}{16}\alpha^3 + ...$.

The different moments of the charge distribution, which are also independent of the position vector $\mathbf{x}$, can be defined from the integrals in (3.26). The first one is referred to the monopole moment of the system, or the net charge q. The second and the third one are called the dipole moment $\mathbf{p}$ and the quadrupole, respectively. Generally, the moments excluding the monopole moment in (3.26) have a dependency on $\mathbf{x}_0$. The interest of this work lies only on the net charge and the dipole moment of the system. For that reason the higher order moments of the system are not taken into consideration.

Note that the dipole moment is independent of $\mathbf{x}_0$, in the case of the net charge being zero. Otherwise, $\mathbf{x}_0$ is considered to be the center of the charge distribution. The (macroscopic) volume density of the charge and the volume density of the polarization are defined as the spatial averages of the quantities in the representative volume V^R

$$q = \frac{\sum_i q_i}{V^R}, \qquad \mathbf{P} = \frac{\sum_i \mathbf{p}_i}{V^R}. \tag{3.27}$$

The polarization can be interpreted as the relative displacement of positive and negative bound charges in a body. By adding the vacuum displacement field $\epsilon_0\mathbf{E}$, the so called electric displacement can be defined as

$$\mathbf{D} = \mathbf{P} + \epsilon_0\mathbf{E}. \tag{3.28}$$

3.5   Electrostatics in matter

The previous sections of this chapter dealt with the systems of point charges and charge densities in vacuum. In the case of matter, the field equations (3.23) and (3.24) describing the electrostatics are also equally applicable. But to transfer the field equations to matter

requires a careful averaging technique. The total charge density ρ_{tot} and the electric field $\mathbf{E}_{\text{tot}}$ can be divided as

$$\rho_{\text{tot}} \;=\; \rho_0 + \rho^{\text{free}} + \rho^{\text{bound}} = \rho_0 + \rho, \tag{3.29}$$

$$\mathbf{E}_{\text{tot}} \;=\; \mathbf{E}_0 + \mathbf{E}^{\text{free}} + \mathbf{E}^{\text{bound}} = \mathbf{E}_0 + \mathbf{E}, \tag{3.30}$$

respectively. Here ρ_0 is the charge density of the undisturbed matter and $\mathbf{E}_0$ is the corresponding electric field. The density ρ^{free} is the free charges which are capable of moving through the matter. These free charges may create an electric current in response to an external electric field. The charge density ρ^{free} consists of extra charges and free induced charges. While the density ρ^{bound} is the bound charges, which is a part of the induced charges in the material. With the help of an external electric field, the bound charges can only be displaced by a certain amount without leaving the material.

As a result, the electrostatic field equations (3.23) and (3.24) can be written as

$$\epsilon_0 \text{div}(\mathbf{E}_0 + \mathbf{E}) = \rho_0 + \rho \;\; \text{and} \;\; \text{curl}(\mathbf{E}_0 + \mathbf{E}) = \mathbf{0}. \tag{3.31}$$

As these field equations are linear, the following equations can be stated

$$\epsilon_0 \text{div}\mathbf{E} = \rho \;\; \text{and} \;\; \text{curl}\mathbf{E} = \mathbf{0}. \tag{3.32}$$

These electrostatic field equations are only applicable on the microscopic level of the material. The microscopic field equations require to be substituted with the macroscopic electrostatic field equations in order to obtain a continuum description of the field equations. The macroscopic field equations are derived by means of a spatial averaging procedure using the convolution theorem.

By using the averaging procedure, equation (3.32) can be written as

$$\epsilon_0 \text{div}\langle \mathbf{E} \rangle = \langle \rho^{\text{free}} \rangle + \langle \rho_{\text{ind}}^{\text{bound}} \rangle \;\; \text{and} \;\; \text{curl}\langle \mathbf{E} \rangle = \mathbf{0}. \tag{3.33}$$

The material polarization $\mathbf{P}^{\text{mat}}$ is determined through the volume average of the dipole moments in the material and holds the following balance equation,

$$\text{div}\mathbf{P}^{\text{mat}} = -\langle \rho_{\text{ind}}^{\text{bound}} \rangle. \tag{3.34}$$

Equations (3.34) and (3.33) give

$$\text{div}\left(\langle\epsilon_0\mathbf{E}\rangle + \mathbf{P}^{\text{mat}}\right) = \langle\rho^{\text{free}}\rangle. \tag{3.35}$$

The macroscopic electrostatic field equations

$$\text{div}\mathbf{D} = \rho \quad \text{and} \quad \text{curl}\mathbf{E} = \mathbf{0} \tag{3.36}$$

are derived from (3.35) by using the definition of the electric displacement $\mathbf{D} = \langle\epsilon_0\mathbf{E}\rangle + \mathbf{P}^{\text{mat}}$, and the notation $\mathbf{E} := \langle\epsilon_0\mathbf{E}\rangle$ and $\rho := \langle\rho^{\text{free}}\rangle$.

The electric displacement shows a jump in the normal direction on the boundary of the continuum material body. It is identical to the density of free surface charges,

$$[\![\mathbf{D}]\!] \cdot \mathbf{n} = \omega, \tag{3.37}$$

where $\mathbf{n}$ denotes the outer normal to the boundary $\partial\mathcal{B}$. For the definition of the jump operator $[\![\cdot]\!]$, see Appendix A.1.

Electrostatic energy:

In Section 3.3, it is mentioned that the total potential energy of charges in free space is written as

$$U = \frac{1}{2}\int_{\mathcal{B}}\varphi(\bar{\mathbf{x}})\rho(\bar{\mathbf{x}})\text{d}\bar{\Omega} \tag{3.38}$$

due to a charge density $\rho(\bar{\mathbf{x}})$ and a potential $\varphi(\bar{\mathbf{x}})$. To be applicable for matter, or specifically for dielectric matter, no assumption considering linearity, uniformity, etc., of the response of a dielectric matter to an applied field will be made. Rather a small change in the potential energy δU due to some sort of change $\delta\rho$ in the macroscopic charge density ρ is considered prevailing in all space. The work done to obtain this change is

$$\delta U = \frac{1}{2}\int_{\mathcal{B}}\varphi(\bar{\mathbf{x}})\delta\rho(\bar{\mathbf{x}})\text{d}\bar{\Omega}. \tag{3.39}$$

As $\text{div}\mathbf{D} = \rho$, the change $\delta\rho$ can be linked to a change in the electric displacement $\delta\mathbf{D}$:

$$\delta\rho = \text{div}(\delta\mathbf{D}). \tag{3.40}$$

In the following the total potential energy change can be written as

$$\delta U = \int_{\mathcal{B}} \mathbf{E} \cdot \delta \mathbf{D} \mathrm{d}\Omega, \tag{3.41}$$

where the electric field definition $\mathbf{E} = -\nabla \varphi$ is used and $\rho(\bar{\mathbf{x}})$ is considered as a localized charge distribution.

If the medium is assumed linear, then

$$\mathbf{E} \cdot \delta \mathbf{D} = \frac{1}{2} \delta (\mathbf{E} \cdot \mathbf{D}), \tag{3.42}$$

and the change of total potential energy is

$$\delta U = \frac{1}{2} \int_{\mathcal{B}} \delta (\mathbf{E} \cdot \mathbf{D}) \mathrm{d}\Omega, \tag{3.43}$$

and the total potential energy can be expressed as

$$U = \frac{1}{2} \int_{\mathcal{B}} \mathbf{E} \cdot \mathbf{D} \mathrm{d}\Omega. \tag{3.44}$$

In a local form the electric energy density for matter is written as

$$W = \frac{1}{2} \mathbf{E} \cdot \mathbf{D}. \tag{3.45}$$

Chapter 4

Theory of piezoelectric materials

This chapter provides a brief overview about the material theory of piezoelectric materials. The purpose of the theory of piezoelectric materials is to describe mathematically the material behaviour. This chapter includes field equations, material laws and configurational force theory of these materials. It also gives a numerical treatment of the standard boundary value problem (BVP) of piezoelectric materials as well as of configurational forces. As piezoelectric materials exhibit an electro-mechanical coupling, the corresponding theories for both mechanical and electrical parts for matter are presented. Piezoelectric materials produce an internal electric field when they are strained. On the other hand, piezoelectric materials exhibit strain or stress when an external electric field is applied to them. Here the field equations for both mechanical and electrical part are presented separately, and the coupling between the mechanical and electrical behavior of piezoelectric materials is obtained through the material laws. Readers are referred for a detailed theoretical background of piezoelectric materials to Müller et al. [72], Schrade et al. [88], etc. For numerical treatment of BVP of piezoelectric materials see Allik and Hughes [3], Müller et al. [72], etc.

4.1 Field equations

We consider a piezoelectric body $\mathcal{B}$ which contains a domain wall and two domains. The normal vector $\mathbf{n}_{\mathcal{S}}$ to a domain wall $\mathcal{S}$ points from the sub-body $\mathcal{B}^-$ into $\mathcal{B}^+$, for details see

Figure 4.1. Neglecting the inertia term the Cauchy stress tensor $\boldsymbol{\sigma}$ fulfills the mechanical equilibrium condition. The mechanical equilibrium has the form

$$
\begin{aligned}
\operatorname{div} \boldsymbol{\sigma} + \mathbf{f} &= \mathbf{0} \quad \text{in} \quad \mathcal{B}, \\
[\![\boldsymbol{\sigma}]\!]\mathbf{n}_{\mathcal{S}} &= \mathbf{0} \quad \text{on} \quad \mathcal{S},
\end{aligned}
\tag{4.1}
$$

in the bulk considering the body force $\mathbf{f}$ and on the domain wall, respectively. See Appendix A.1 or Müller et al. [72] for the definition of the jump operator $[\![(\cdot)]\!]$. The mechanical problem needs to be completed with suitable boundary conditions. Assigning either the displacements $\mathbf{u}^*$ on the boundary $\partial\mathcal{B}_u$ or the tractions $\mathbf{t}^*$ on the boundary $\partial\mathcal{B}_t$, one has

$$
\begin{aligned}
\mathbf{u} &= \mathbf{u}^* \quad \text{on} \quad \partial\mathcal{B}_u, \\
\boldsymbol{\sigma}\mathbf{n} &= \mathbf{t}^* \quad \text{on} \quad \partial\mathcal{B}_t.
\end{aligned}
\tag{4.2}
$$

The electric displacement $\mathbf{D}$ fulfills the electrostatic relation (Gauß law). In the presence of volume charges q, the field equations in the bulk and on the domain wall are

$$
\begin{aligned}
\operatorname{div} \mathbf{D} - q &= 0 \quad \text{in} \quad \mathcal{B}, \\
[\![\mathbf{D}]\!]\cdot\mathbf{n}_{\mathcal{S}} &= 0 \quad \text{on} \quad \mathcal{S} \ (\text{charge free interfaces}).
\end{aligned}
\tag{4.3}
$$

One can prescribe either the electric potential φ^* or the surface charge Q^* on the boundary,

$$
\begin{aligned}
\varphi &= \varphi^* \quad \text{on} \quad \partial\mathcal{B}_\varphi, \\
\mathbf{D} \cdot \mathbf{n} &= -Q^* \quad \text{on} \quad \partial\mathcal{B}_Q.
\end{aligned}
\tag{4.4}
$$
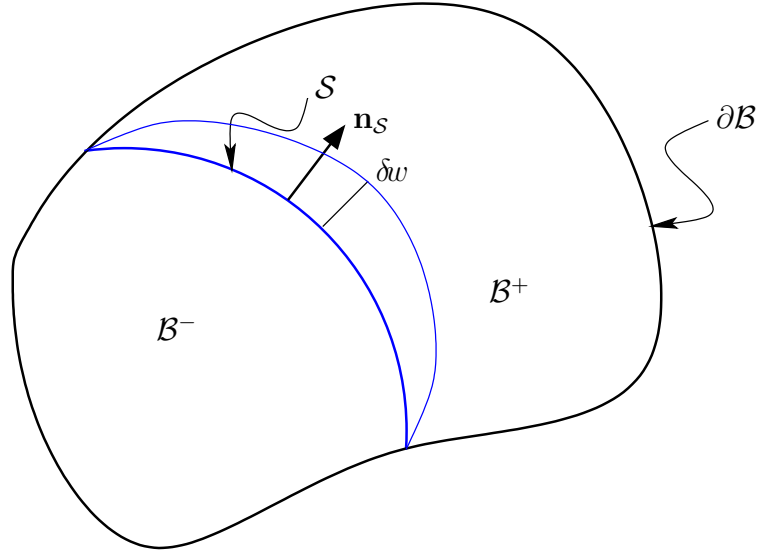
Figure 4.1: *A piezoelectric body containing a domain wall*

The kinematic relations in the bulk and on the domain wall are defined by

$$\varepsilon = \frac{1}{2}\left(\nabla \mathbf{u} + (\nabla \mathbf{u})^T\right) \quad \text{in} \quad \mathcal{B},$$
$$[\![\mathbf{u}]\!] = \mathbf{0} \quad \text{on} \quad \mathcal{S}, \tag{4.5}$$

where the linearized strain tensor ε represents the symmetric part of the displacement gradient. The second relation in (4.5) confirms a continuous displacement across a domain wall. Thus, separation, sliding, or interpenetration of the domains is not allowed, see Leo and Sekerka [53]. For the electric part, the following relations of the electric field $\mathbf{E}$ and electric potential φ are required,

$$\mathbf{E} = -\nabla\varphi \quad \text{in} \quad \mathcal{B},$$
$$[\![\varphi]\!] = 0 \quad \text{on} \quad \mathcal{S}. \tag{4.6}$$

The electric field $\mathbf{E}$ is defined as the negative gradient of the electric potential φ. Across the domain wall, a continuous electric potential is assumed by the second relation in (4.6).

All the field equations mentioned above are applicable for a boundary value problem (BVP) of the piezoelectric materials on the micro level. In the case of a macro BVP, all field equations excluding the equations with jump operators should be taken into account, since it is assumed that the piezoelectric materials are macroscopically free of interfaces.

4.2   Piezoelectric constitutive law

To complete the field equations in the previous sections for a certain material, constitutive relations are needed, which relate the Cauchy stress tensor $\boldsymbol{\sigma}$ and the electric displacement vector $\mathbf{D}$ to the strain tensor $\boldsymbol{\varepsilon}$ and the electric field $\mathbf{E}$. The material response of a ferroelectric ceramic under small electric or mechanical loading may be described by a linear piezoelectric constitutive law. One can write the electric enthalpy function as a thermodynamical potential,

$$H(\boldsymbol{\varepsilon}, \mathbf{E}) = \frac{1}{2}(\boldsymbol{\varepsilon} - \boldsymbol{\varepsilon}^0) \colon \left[\mathbb{C}(\boldsymbol{\varepsilon} - \boldsymbol{\varepsilon}^0)\right] - (\boldsymbol{\varepsilon} - \boldsymbol{\varepsilon}^0) \colon (\mathbb{b}^T \mathbf{E}) - \frac{1}{2}\mathbf{E}\cdot(\mathbf{A}\,\mathbf{E}) - \mathbf{P}^0\cdot\mathbf{E}, \quad (4.7)$$

which comprises an elastic, an electric and a coupling part. Taking the partial derivative with respect to $\boldsymbol{\varepsilon}$ and the negative of the partial derivative with respect to $\mathbf{E}$, one obtains the Cauchy stress tensor $\boldsymbol{\sigma}$ and the electric displacement $\mathbf{D}$ via

$$\boldsymbol{\sigma} = \frac{\partial H}{\partial \boldsymbol{\varepsilon}} = \mathbb{C}(\boldsymbol{\varepsilon} - \boldsymbol{\varepsilon}^0) - \mathbb{b}^T \mathbf{E}, \tag{4.8}$$

$$\mathbf{D} = -\frac{\partial H}{\partial \mathbf{E}} = \mathbb{b}(\boldsymbol{\varepsilon} - \boldsymbol{\varepsilon}^0) + \mathbf{A}\,\mathbf{E} + \mathbf{P}^0, \tag{4.9}$$

where $\mathbb{C}$ is the elastic tensor, $\mathbb{b}$ the piezoelectric tensor, $\mathbf{A}$ the dielectric tensor, $\boldsymbol{\varepsilon}^0$ the remanent strain, and $\mathbf{P}^0$ the spontaneous polarization.

4.3   Numerical implementation of piezoelectric materials using finite elements

In the previous sections, the theory of piezoelectric materials (BVP of piezoelectric materials) was illustrated. For a piezoelectric body with simple geometry and simple domain structure, the system of BVPs may be solved analytically. In the case of a piezoelectric body with complex geometry and complex domain structure, numerical methods are used to solve the BVPs. In the following section, a numerical treatment of the BVPs for piezoelectric materials using finite element method will be presented. For a detailed description of the numerical methods of piezoelectric materials, the reader is referred to Allik and Hughes [3], Müller et al. [72], etc.

4.3.1   Variational procedure

The total potential of piezoelectric materials can be written by the internal potential Π^{int} (containing H of (4.7)) and the potential Π^{ext} of the externally applied forces and charges:

$$\Pi[\mathbf{u}, \varphi, \mathcal{S}] = \underbrace{\int_{\mathcal{B}^{+/-}} H \mathrm{d}\Omega}_{\Pi^{\text{int}}} \underbrace{- \int_{\mathcal{B}^{+/-}} (\mathbf{f} \cdot \mathbf{u} - q\varphi) \mathrm{d}\Omega - \int_{\partial\mathcal{B}_t} \mathbf{t}^* \cdot \mathbf{u} \mathrm{d}\Gamma + \int_{\partial\mathcal{B}_Q} Q^* \varphi \mathrm{d}\Gamma}_{\Pi^{\text{ext}}}. \quad (4.10)$$

The total potential depends on the displacement field $\mathbf{u}$, the electric potential φ and the position of the domain wall $\mathcal{S}$. Here the domain wall is considered to be mobile. For that reason the fields and the position of the domain wall are required to be taken into account when the variation of the total potential is determined. Beginning with the internal potential, one obtains

$$\begin{aligned} \delta\Pi^{\text{int}} &= \int_{\mathcal{B}^{+/-}} \left(\frac{\partial H}{\partial \boldsymbol{\varepsilon}} : \delta\boldsymbol{\varepsilon} + \frac{\partial H}{\partial \mathbf{E}} : \delta\mathbf{E} \right) \mathrm{d}\Omega - \int_{\mathcal{S}} [\![H]\!] \delta w \mathrm{d}\Gamma \\ &= \int_{\mathcal{B}^{+/-}} (\boldsymbol{\sigma} : \delta\boldsymbol{\varepsilon} - \mathbf{D} : \delta\mathbf{E}) \mathrm{d}\Omega - \int_{\mathcal{S}} [\![H]\!] \delta w \mathrm{d}\Gamma. \end{aligned} \quad (4.11)$$

Here the term δw is the variation (mobility) of the domain wall in the direction of the normal $\mathbf{n}_{\mathcal{S}}$, see Figure 4.1. The variation of the external potential can be expressed by

$$\delta\Pi^{\text{ext}} = \int_{\mathcal{B}^{+/-}} (-\mathbf{f} \cdot \delta\mathbf{u} + q\delta\varphi) \mathrm{d}\Omega - \int_{\partial\mathcal{B}_t} \mathbf{t}^* \cdot \delta\mathbf{u} \mathrm{d}\Gamma + \int_{\partial\mathcal{B}_Q} Q^* \delta\varphi \mathrm{d}\Gamma. \quad (4.12)$$

4.3.2   Finite element procedure

Finite element method is used to solve the field equations. In order to calculate the field variables, the domain wall is kept fixed at a certain position ($\delta w = 0$). To determine the field variables as well as the configurational forces, the field equations (4.1) and (4.3) are to be solved.

The finite element formulation begins with the variations (4.11) and (4.12). Disregarding all terms with δw provides the variation of the total potential

$$\delta\Pi = \int_{\mathcal{B}} (\boldsymbol{\sigma} : \delta\boldsymbol{\varepsilon} - \mathbf{f} \cdot \delta\mathbf{u}) \mathrm{d}\Omega - \int_{\partial\mathcal{B}_t} \mathbf{t}^* \cdot \delta\mathbf{u} \mathrm{d}\Gamma$$

$$+ \int_{\mathcal{B}}(-\mathbf{D} \cdot \delta\mathbf{E} + q\delta\varphi)\mathrm{d}\Omega + \int_{\partial\mathcal{B}_Q} Q^*\delta\varphi\mathrm{d}\Gamma = 0. \qquad (4.13)$$

In the following a Voigt-notation expressed by the under-bar (for a detailed overview of Voigt-notation, see appendix A.2) is introduced. So, the required discretizations within a finite element setting are:

$$
\begin{aligned}
\underline{\boldsymbol{\sigma}} &= \mathbb{C}(\underline{\boldsymbol{\varepsilon}} - \underline{\boldsymbol{\varepsilon}}^0) - \underline{\mathbb{b}}^T\underline{\mathbf{E}}, & \underline{\mathbf{D}} &= \underline{\mathbb{b}}(\underline{\boldsymbol{\varepsilon}} - \underline{\boldsymbol{\varepsilon}}^0) + \underline{\mathbf{A}}\,\underline{\mathbf{E}} + \underline{\mathbf{P}}^0, \\
\underline{\mathbf{u}} &= \sum_I N_u^I\underline{\mathbf{u}}^I, & \varphi &= \sum_I N_\varphi^I\varphi^I, \\
\underline{\delta\mathbf{u}} &= \sum_I N_u^I\underline{\delta\mathbf{u}}^I, & \delta\varphi &= \sum_I N_\varphi^I\delta\varphi^I, \\
\underline{\boldsymbol{\varepsilon}} &= \sum_I \underline{\mathbf{B}}_u^I\underline{\mathbf{u}}^I, & \underline{\mathbf{E}} &= -\sum_I \underline{\mathbf{B}}_\varphi^I\underline{\varphi}^I, \\
\underline{\delta\boldsymbol{\varepsilon}} &= \sum_I \underline{\mathbf{B}}_u^I\underline{\delta\mathbf{u}}^I, & \underline{\delta\mathbf{E}} &= -\sum_I \underline{\mathbf{B}}_\varphi^I\underline{\delta\varphi}^I.
\end{aligned}
\qquad (4.14)
$$

Here the superscript I is the node number and N_u^I, N_φ^I denote the shape functions for the displacements and electric potential, respectively. The derivatives of the shape functions define the matrices $\underline{\mathbf{B}}_u^I$ and $\underline{\mathbf{B}}_\varphi^I$ as

$$
\underline{\mathbf{B}}_u^I = \begin{bmatrix} N_{u,x_1}^I & 0 \\ 0 & N_{u,x_2}^I \\ N_{u,x_2}^I & N_{u,x_1}^I \end{bmatrix}, \qquad \underline{\mathbf{B}}_\varphi^I = \begin{bmatrix} N_{\varphi,x_1}^I \\ N_{\varphi,x_2}^I \end{bmatrix}, \qquad (4.15)
$$

where our attention is restricted to 2D formulations. Inserting (4.14) in (4.13) infers

$$
\begin{aligned}
\delta\Pi &= \sum_I (\underline{\delta\mathbf{u}}^I)^T \left\{ \int_{\mathcal{B}^e} \left[(\underline{\mathbf{B}}_u^I)^T\underline{\boldsymbol{\sigma}} - N_u^I\underline{\mathbf{f}}\right]\mathrm{d}\Omega - \int_{\partial\mathcal{B}_t^e} N_u^I\underline{\mathbf{t}}^*\mathrm{d}\Gamma \right\} \\
&+ \sum_I \delta\varphi^I \left\{ \int_{\mathcal{B}^e} \left[(\underline{\mathbf{B}}_\varphi^I)^T\underline{\mathbf{D}} + N_\varphi^I q\right]\mathrm{d}\Omega + \int_{\partial\mathcal{B}_Q^e} N_\varphi^I Q^*\mathrm{d}\Gamma \right\} = 0, \quad (4.16)
\end{aligned}
$$

where $\mathcal{B}^e$ is the volume contained by the considered element. As the variation $\underline{\delta\mathbf{u}}^I$ and $\delta\varphi^I$ are arbitrary, equation (4.16) can be expressed as

$$
\sum_J \begin{bmatrix} \int_{\mathcal{B}^e}(\underline{\mathbf{B}}_u^I)^T\mathbb{C}\,\underline{\mathbf{B}}_u^J\mathrm{d}\Omega & \int_{\mathcal{B}^e}(\underline{\mathbf{B}}_u^I)^T\underline{\mathbb{b}}^T\underline{\mathbf{B}}_\varphi^J\mathrm{d}\Omega \\ \int_{\mathcal{B}^e}(\underline{\mathbf{B}}_\varphi^I)^T\underline{\mathbb{b}}^T\underline{\mathbf{B}}_u^J\mathrm{d}\Omega & -\int_{\mathcal{B}^e}(\underline{\mathbf{B}}_\varphi^I)^T\underline{\mathbb{b}}^T\underline{\mathbf{B}}_\varphi^J\mathrm{d}\Omega \end{bmatrix} \begin{bmatrix} \underline{\mathbf{u}}^J \\ \varphi^J \end{bmatrix} =
$$

$$\left[\begin{array}{c} \int_{\mathcal{B}^e} \left[(\underline{\mathbf{B}}_u^I)^T \underline{\mathbb{C}} \, \underline{\boldsymbol{\varepsilon}}^0 + N_u^I \underline{\mathbf{f}} \right] \mathrm{d}\Omega + \int_{\partial \mathcal{B}_t^e} N_u^I \underline{\mathbf{t}}^* \mathrm{d}\Gamma \\ \int_{\mathcal{B}^e} \left[(\underline{\mathbf{B}}_\varphi^I)^T \underline{\mathbb{b}} \, \underline{\boldsymbol{\varepsilon}}^0 - (\underline{\mathbf{B}}_\varphi^I)^T \underline{\mathbf{P}}^0 - N_\varphi^I q \right] \mathrm{d}\Omega - \int_{\partial \mathcal{B}_Q^e} N_\varphi^I Q^* \mathrm{d}\Gamma \end{array} \right]. \qquad (4.17)$$

In the next step this subsystem of linear equations is to be assembled to obtain the overall system of equations. In the following the boundary conditions regarding the displacements or electric potential are applied to the system of equations. This is a standard procedure in the finite element analysis, and therefore a detailed explanation is omitted here. For more details the reader is referred to standard textbooks on the FEM (e.g, Hughes [41], Wriggers [111], Zienkiewicz and Taylor [114]).

4.4 Configurational forces for piezoelectric materials

The theory of configurational forces, which are also known as material forces, gives an excellent tool for investigating the material behaviour with various kinds of material defects. The credit of making the introduction and calculating configurational forces goes back to the work of Eshelby in the early fifties of the 20th century, Eshelby [14]. Configurational forces are interpreted as energy changes of the system. It is widely used in fracture mechanics and in phase transformations.

4.4.1 Derivation of configurational forces

Section 2.6.1 and 2.6.2 provide the formulations of configurational forces for large deformation and small deformation problem, respectively. The formulations presented in those sections are for pure mechanical problem. As piezoelectric materials are electromechanically coupled, a formulation of the configurational force should incorporate the effect both from mechanical and electrical responses. Here we consider an inhomogeneous body $\mathcal{B}$ as in Figure 4.1. The electric enthalpy H depends on the strain $\boldsymbol{\varepsilon}$, the electric field $\mathbf{E}$ and explicitly on the position vector $\mathbf{x}$: $H = \hat{H}(\boldsymbol{\varepsilon}, \mathbf{E}; \mathbf{x})$. For the derivation of the configurational force balance of piezoelectric materials, we start from the definition of the electric enthalpy for piezoelectric materials:

$$H = \frac{1}{2}(\boldsymbol{\varepsilon} - \boldsymbol{\varepsilon}^0) \colon \left[\mathbb{C}(\boldsymbol{\varepsilon} - \boldsymbol{\varepsilon}^0) \right] - (\boldsymbol{\varepsilon} - \boldsymbol{\varepsilon}^0) \colon (\mathbb{b}^T \mathbf{E}) - \frac{1}{2}\mathbf{E} \cdot (\mathbf{A} \, \mathbf{E}) - \mathbf{P}^0 \cdot \mathbf{E}. \qquad (4.18)$$

This implies for fixed spontaneous strain and fixed spontaneous polarization the following rate form

$$
\begin{aligned}
\dot{H} &= \dot{\boldsymbol{\varepsilon}} : \left[\mathbb{C}(\boldsymbol{\varepsilon} - \boldsymbol{\varepsilon}^0) \right] - \dot{\boldsymbol{\varepsilon}} : (\mathbb{b}^T \mathbf{E}) - \mathbb{b}(\boldsymbol{\varepsilon} - \boldsymbol{\varepsilon}^0) \cdot \dot{\mathbf{E}} - (\mathbf{A}\,\mathbf{E}) \cdot \dot{\mathbf{E}} - \mathbf{P}^0 \cdot \dot{\mathbf{E}} \\
&= \dot{\boldsymbol{\varepsilon}} : \left[\mathbb{C}(\boldsymbol{\varepsilon} - \boldsymbol{\varepsilon}^0) - \mathbb{b}^T \mathbf{E} \right] - \left[\mathbb{b}(\boldsymbol{\varepsilon} - \boldsymbol{\varepsilon}^0) + \mathbf{A}\,\mathbf{E} + \mathbf{P}^0 \right] \cdot \dot{\mathbf{E}} \\
&= \boldsymbol{\sigma} : \dot{\boldsymbol{\varepsilon}} - \mathbf{D} \cdot \dot{\mathbf{E}}.
\end{aligned}
\tag{4.19}
$$

By using the definition of the strain tensor $\boldsymbol{\varepsilon} = \dfrac{1}{2}(\nabla \mathbf{u} + (\nabla \mathbf{u})^T)$ and the electric field $\mathbf{E} = -\nabla\varphi$, equation (4.19) can be written as

$$
\dot{H} = \underbrace{\boldsymbol{\sigma} : \nabla\dot{\mathbf{u}}}_{\dot{H}_{\mathrm{m}}} + \underbrace{\mathbf{D} \cdot \nabla\dot{\varphi}}_{\dot{H}_{\mathrm{e}}}.
\tag{4.20}
$$

Using the product rule, equation (4.20) can be rewritten as

$$
\dot{H} = (\boldsymbol{\sigma} : \nabla\mathbf{u})^{\cdot} - \dot{\boldsymbol{\sigma}} : \nabla\mathbf{u} + (\mathbf{D} \cdot \nabla\varphi)^{\cdot} - \dot{\mathbf{D}} \cdot \nabla\varphi.
\tag{4.21}
$$

Then the gradient of (4.21) is given by

$$
\nabla\dot{H} = \nabla(\boldsymbol{\sigma} : \nabla\mathbf{u})^{\cdot} - \nabla(\dot{\boldsymbol{\sigma}} : \nabla\mathbf{u}) + \nabla(\mathbf{D} \cdot \nabla\varphi)^{\cdot} - \nabla(\dot{\mathbf{D}} \cdot \nabla\varphi).
\tag{4.22}
$$

Using the identities

$$
\begin{aligned}
\nabla(\boldsymbol{\sigma} : \nabla\mathbf{u}) &= \nabla\boldsymbol{\sigma} : \nabla\mathbf{u} + \operatorname{div}\!\left((\nabla\mathbf{u})^T \boldsymbol{\sigma} \right) - (\nabla\mathbf{u})^T \operatorname{div}\boldsymbol{\sigma}, \\
\nabla(\mathbf{D} \cdot \nabla\varphi) &= \nabla\mathbf{D}\nabla\varphi + \operatorname{div}(\nabla\varphi \otimes \mathbf{D}) - \nabla\varphi\operatorname{div}\mathbf{D},
\end{aligned}
$$

equation (4.22) can be reformulated as

$$
\begin{aligned}
\nabla\dot{H} - \operatorname{div}\!\left((\nabla\mathbf{u})^T \boldsymbol{\sigma} \right)^{\cdot} &+ \left((\nabla\mathbf{u})^T \operatorname{div}\boldsymbol{\sigma} \right)^{\cdot} + \nabla(\dot{\boldsymbol{\sigma}} : \nabla\mathbf{u}) - (\nabla\boldsymbol{\sigma} : \nabla\mathbf{u})^{\cdot} \\
- \operatorname{div}(\nabla\varphi \otimes \mathbf{D})^{\cdot} &+ (\nabla\varphi\operatorname{div}\mathbf{D})^{\cdot} + \nabla(\dot{\mathbf{D}} \cdot \nabla\varphi) - (\nabla\mathbf{D}\nabla\varphi)^{\cdot} = \mathbf{0}.
\end{aligned}
\tag{4.23}
$$

Integrating equation (4.23) with respect to time t and using the mechanical equilibrium condition $\operatorname{div}\boldsymbol{\sigma} + \mathbf{f} = \mathbf{0}$ as well as the electrostatic balance condition $\operatorname{div}\mathbf{D} - q = 0$ yields

$$
\operatorname{div}\boldsymbol{\Sigma} - (\nabla\mathbf{u})^T \mathbf{f} + (\nabla\varphi)q
$$

$$+ \int_0^t \left(\nabla(\dot{\boldsymbol{\sigma}} : \nabla\mathbf{u}) - (\nabla\boldsymbol{\sigma} : \nabla\mathbf{u})^{\cdot} + \nabla(\dot{\mathbf{D}} \cdot \nabla\varphi) - (\nabla\mathbf{D}\nabla\varphi)^{\cdot} \right) \mathrm{d}\tau = \mathbf{0}, \qquad (4.24)$$

where

$$\boldsymbol{\Sigma} = H\,\mathbf{1} - (\nabla\mathbf{u})^T \boldsymbol{\sigma} - \nabla\varphi \otimes \mathbf{D} \qquad (4.25)$$

is introduced as the electro-mechanical Eshelby stress tensor.

Rewriting the time integrals in (4.24) for the mechanical and electrical part (subscript m and e for mechanical and electrical, respectively) as

$$\int_0^t (\dot{\boldsymbol{\sigma}} : \nabla\nabla\mathbf{u} - \nabla\boldsymbol{\sigma} : \nabla\dot{\mathbf{u}})\,\mathrm{d}\tau = \int_0^t ((\boldsymbol{\sigma} : \nabla\nabla\mathbf{u})^{\cdot} - \boldsymbol{\sigma} : \nabla\nabla\dot{\mathbf{u}} - \nabla\boldsymbol{\sigma} : \nabla\dot{\mathbf{u}})\,\mathrm{d}\tau$$

$$= \boldsymbol{\sigma} : \nabla\nabla\mathbf{u} - \int_0^t (\underbrace{\boldsymbol{\sigma} : \nabla\nabla\dot{\mathbf{u}} + \nabla\boldsymbol{\sigma} : \nabla\dot{\mathbf{u}}}_{\nabla\dot{H}_{\mathrm{m}}})\,\mathrm{d}\tau, \quad (4.26)$$

and

$$\int_0^t \left(\nabla(\nabla\varphi)\dot{\mathbf{D}} - \nabla\mathbf{D}\nabla\dot{\varphi} \right) \mathrm{d}\tau = \int_0^t ((\nabla(\nabla\varphi)\mathbf{D})^{\cdot} - \nabla(\nabla\dot{\varphi})\mathbf{D} - \nabla\mathbf{D}\nabla\dot{\varphi})\,\mathrm{d}\tau$$

$$= \nabla(\nabla\varphi)\mathbf{D} - \int_0^t (\underbrace{\nabla(\nabla\dot{\varphi})\mathbf{D} + \nabla\mathbf{D}\nabla\dot{\varphi}}_{\nabla\dot{H}_{\mathrm{e}}})\,\mathrm{d}\tau, (4.27)$$

the configurational force balance for piezoelectric materials

$$\mathrm{div}\boldsymbol{\Sigma} + \mathbf{g} = \mathbf{0},$$

$$\text{with} \quad \mathbf{g} = -(\nabla\mathbf{u})^T\mathbf{f} \;+\; (\nabla\varphi)q + \boldsymbol{\sigma} : \nabla\nabla\mathbf{u} - \nabla(\nabla\varphi)\mathbf{D} - (\underbrace{\nabla H_{\mathrm{m}} + \nabla H_{\mathrm{e}}}_{\nabla H}) \qquad (4.28)$$

is obtained. The term $\mathbf{g}$ is called configurational volume force. The gradient of the electric enthalpy $H = \hat{H}(\boldsymbol{\varepsilon}, \mathbf{E}; \mathbf{x})$ can be demonstrated as

$$\nabla H = \underbrace{\frac{\partial\hat{H}}{\partial\boldsymbol{\varepsilon}}}_{\boldsymbol{\sigma}} : \nabla\nabla\mathbf{u} + \nabla(\nabla\varphi)\underbrace{\frac{\partial\hat{H}}{\partial\mathbf{E}}}_{-\mathbf{D}} + \left.\frac{\partial\hat{H}}{\partial\mathbf{x}}\right|_{\mathrm{expl.}}, \qquad (4.29)$$

with the notation expl. for the explicit derivative with respect to position $\mathbf{x}$. Therefore, the local configurational force $\mathbf{g}$ can be compactly summarized as

$$\mathbf{g} = -(\nabla\mathbf{u})^T\mathbf{f} + (\nabla\varphi)q - \left.\frac{\partial\hat{H}}{\partial\mathbf{x}}\right|_{\text{expl.}}. \tag{4.30}$$

From this it can be concluded that all of the following can cause a configurational force: 1) a physical body force $\mathbf{f}$; 2) a volume charge density q; 3) an inhomogeneity in the material. As a consequence, the Eshelby stress tensor $\boldsymbol{\Sigma}$ is not a divergence free quantity in these cases. According to Kienzler & Herrmann [48] this gives the fact that the Eshelby stress tensor is not a conserved quantity.

4.4.2 Numerical implementation of configurational forces using finite elements

To obtain nodal configurational forces based on a FE calculation, the balance equation in (4.28) is discretized in a consistent way by approximating other field equations. Beginning with the weak form of (4.28) by a test function $\boldsymbol{\eta}$,

$$\int_{\mathcal{B}}(\text{div}\boldsymbol{\Sigma} + \mathbf{g})\cdot\boldsymbol{\eta}\text{d}\Omega = 0, \tag{4.31}$$

and by using integration by parts, equation (4.31) can be written as

$$\int_{\partial\mathcal{B}}(\boldsymbol{\Sigma}\mathbf{n})\cdot\boldsymbol{\eta}\text{d}\Gamma - \int_{\mathcal{B}}\boldsymbol{\Sigma}:\nabla\boldsymbol{\eta}\text{d}\Omega + \int_{\mathcal{B}}\mathbf{g}\cdot\boldsymbol{\eta}\text{d}\Omega = 0, \tag{4.32}$$

where $\mathbf{n}$ is the unit normal vector to the boundary. It is assumed that the test function $\boldsymbol{\eta}$ disappears on the boundary $\partial\mathcal{B}$, hence the first integral in (4.32) will be zero. This assumption leads to a stationary boundary, which does not change its position $\mathbf{x}$.

In this thesis our attention is kept restricted to a 2D formulation (plane strain), but the extension to 3D is straightforward and will not be described in detail here. The test function in (4.32) is approximated in each element $\mathcal{B}^e$ by node values $\boldsymbol{\eta}^I$ and shape functions N^I:

$$\underline{\boldsymbol{\eta}} = \sum_I N^I\underline{\boldsymbol{\eta}}^I, \quad \text{where} \quad \underline{\boldsymbol{\eta}} = \begin{bmatrix}\eta_1 & \eta_2\end{bmatrix}^T \quad \text{and} \quad \underline{\boldsymbol{\eta}}^I = \begin{bmatrix}\eta_1^I & \eta_2^I\end{bmatrix}^T. \tag{4.33}$$

By formulating the gradient of the test function and the electro-mechanical Eshelby stress tensor as in the following matrix notation

$$
\underline{\nabla \boldsymbol{\eta}} = [\eta_{1,1} \ \eta_{2,2} \ \eta_{1,2} \ \eta_{2,1}]^T = \sum_I \underline{\mathbf{D}}^I \underline{\boldsymbol{\eta}}^I, \quad \text{where} \quad \underline{\mathbf{D}}^I = \begin{bmatrix} N^I_{,x_1} & 0 \\ 0 & N^I_{,x_2} \\ N^I_{,x_2} & 0 \\ 0 & N^I_{,x_1} \end{bmatrix},
$$

$$
\underline{\boldsymbol{\Sigma}} = [\Sigma_{11} \ \Sigma_{22} \ \Sigma_{12} \ \Sigma_{21}]^T \quad \text{and} \quad \underline{\mathbf{g}} = [g_1 \ g_2]^T, \tag{4.34}
$$

one has the element-wise discretization of (4.32)

$$
\sum_I \underline{\boldsymbol{\eta}}^{I^T} \cdot \left[-\int_{\mathcal{B}^e} \underline{\mathbf{D}}^{I^T} \cdot \underline{\boldsymbol{\Sigma}} \, d\Omega + \int_{\mathcal{B}^e} N^I \underline{\mathbf{g}} \, d\Omega \right] = 0. \tag{4.35}
$$

It needs to be stated that the Voigt-notation for symmetric tensors cannot be considered, since the Eshelby stress tensor is generally not symmetric, see (4.25). The Eshelby stress tensor $\boldsymbol{\Sigma}$ shows the symmetry only if the material is isotropic. As equation (4.35) is to be satisfied for arbitrary nodal values $\boldsymbol{\eta}^I$, the term within the square brackets must disappear. This obviously yields the discrete configurational forces

$$
\underline{\mathbf{G}}^I_e = \left\{ \begin{array}{c} G^I_{e1} \\ G^I_{e2} \end{array} \right\} = \int_{\mathcal{B}^e} N^I \underline{\mathbf{g}}^I \, d\Omega = \int_{\mathcal{B}^e} \underline{\mathbf{D}}^{I^T} \cdot \underline{\boldsymbol{\Sigma}} \, d\Omega
$$

$$
= \int_{\mathcal{B}^e} \left\{ \begin{array}{c} N^I_{,x_1} \Sigma_{11} + N^I_{,x_2} \Sigma_{12} \\ N^I_{,x_1} \Sigma_{21} + N^I_{,x_2} \Sigma_{22} \end{array} \right\} d\Omega. \tag{4.36}
$$

The configurational forces $\underline{\mathbf{G}}^I_e$ regarding all n_e elements adjacent to node K are then assembled to a total configurational force

$$
\underline{\mathbf{G}}^K = \bigcup_{e=1}^{n_e} \underline{\mathbf{G}}^I_e. \tag{4.37}
$$

This does not give a new boundary value problem, as the nodal values $\underline{\mathbf{G}}^K$ can be determined from the quantities that are already computed (strain, stress, deformation measures, electric field, electric displacement and electric potential measures) in the solution of the displacement fields and the electric potentials. The determination of the discrete configurational forces is therefore considered as a post-processing step.

Chapter 5

Material homogenization in a small strain framework using configurational force theory

In this chapter a homogenization technique for a pure mechanical problem is described to determine the homogenized mechanical quantities. Special attention is given to the homogenization of the Eshelby stress tensor. Among the homogenization techniques, the FE^2-based homogenization is computationally efficient. This homogenization is a two-scale homogenization, in which two boundary value problems (BVPs) are solved: one on the macro level, and the other on the micro level. On the macro level no constitutive law is prescribed, but a boundary value problem on the micro level is used to determine the homogenized material response. In order to obtain representative numerical results on the macro level, or to capture the effect of micro inhomogeneities on the macro problem, it is necessary to attach a micro domain to each macro Gauß point. This micro domain should contain enough microstructural features of the material. Therefore, it is usually called representative volume element (RVE), see Figure 5.1. In order to solve the micro BVP, admissible boundary conditions are required.

A literature review reveals that the macro strain tensor is used to define the boundary conditions for the micro BVP in deformation driven homogenization. This gives consistent simulation results for the homogenized Cauchy stress tensor and the homogenized material parameters. However, the homogenization of the Eshelby stress tensor gives non-physical results for the macro configurational forces if a deformation driven homogeniza-

tion is performed by using the macro strain tensor. A deformation driven homogenization
using the macro displacement gradient solves this issue. In the following sections, the
effect of the boundary conditions of the micro domain on the macro Eshelby stress tensor
and on the macro configurational forces will be discussed in details.

5.1   Deformation driven homogenization

To prescribe the relevant admissible boundary conditions for the RVEs, it is necessary
to pass at each Gauß point either the macro displacement gradient or the macro stress
tensor down to the micro level. With the help of these boundary conditions, the micro
boundary value problem can be solved, and the remaining quantities such as the average
stress tensor or the average displacement gradient are determined, respectively. These av-
eraged quantities are passed back to the macro level as the material response. To simulate
the macro problem, the material parameters are required to be homogenized. A detailed
formulation of the homogenized material parameters will be presented in Chapter 6 for
piezoelectric materials which are electro-mechanically coupled. The formulations exclud-
ing the electrical parts in Chapter 6 can be used to determine the homogenized material
parameters for a pure mechanical problem. Here in this chapter, the focus is restricted to
deformation driven homogenization.
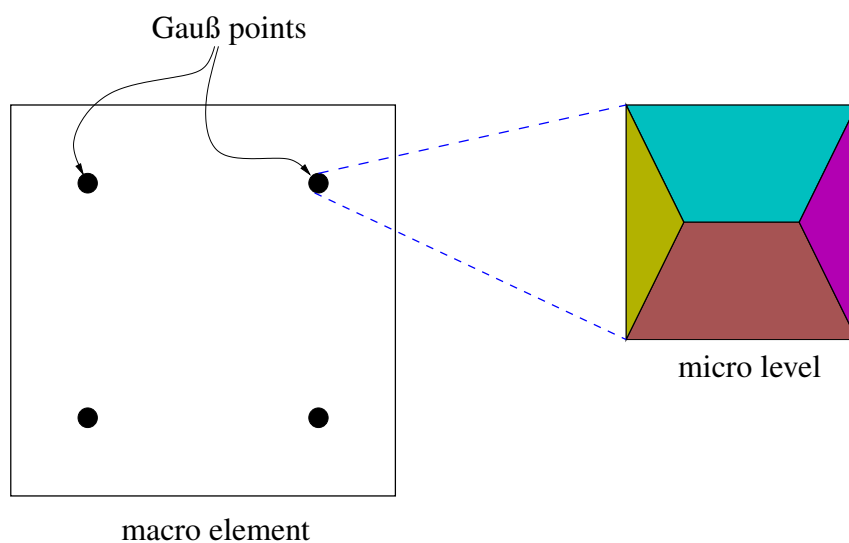
Figure 5.1: *Macro-micro transition*

In the following the macro or averaged quantities are denoted by the symbols with an over-bar, while the micro quantities remain unmarked. In the absence of body forces, the transition between the macro and the micro quantities is given by

$$\overline{\boldsymbol{\varepsilon}} = \frac{1}{V}\int_{\mathcal{B}_{\mathrm{mic}}} \boldsymbol{\varepsilon}\,\mathrm{d}\Omega = \frac{1}{V}\int_{\partial\mathcal{B}_{\mathrm{mic}}} \mathrm{sym}(\mathbf{u}\otimes\mathbf{n})\,\mathrm{d}\Gamma, \quad \overline{\boldsymbol{\sigma}} = \frac{1}{V}\int_{\mathcal{B}_{\mathrm{mic}}} \boldsymbol{\sigma}\,\mathrm{d}\Omega = \frac{1}{V}\int_{\partial\mathcal{B}_{\mathrm{mic}}} \mathrm{sym}(\mathbf{t}\otimes\mathbf{x})\,\mathrm{d}\Gamma. \quad (5.1)$$

A comprehensive proof of the connection between the macro and the micro quantities has been discussed in Schröder [91].

5.1.1 Determination of the admissible boundary conditions for the micro BVP

To have a consistent transition between the macro and the micro quantities, it is essential to satisfy an energy criterion which is the so called Hill-Mandel condition. The Hill-Mandel condition for a pure mechanical problem is defined by

$$\overline{\boldsymbol{\sigma}}:\dot{\overline{\boldsymbol{\varepsilon}}} = \frac{1}{V}\int_{\mathcal{B}_{\mathrm{mic}}} \boldsymbol{\sigma}:\dot{\boldsymbol{\varepsilon}}\,\mathrm{d}\Omega. \tag{5.2}$$

The condition assumes that the mechanical power on the macro level is equivalent to the volume average of the mechanical power on the micro level. By introducing $\mathcal{P}_{\mathrm{m}}$, the Hill-Mandel condition (5.2) can be formulated as

$$\mathcal{P}_{\mathrm{m}} = \frac{1}{V}\int_{\mathcal{B}_{\mathrm{mic}}} \boldsymbol{\sigma}:\dot{\boldsymbol{\varepsilon}}\,\mathrm{d}\Omega - \overline{\boldsymbol{\sigma}}:\dot{\overline{\boldsymbol{\varepsilon}}}. \tag{5.3}$$

The volume integral in (5.3) can be converted to surface or boundary integral with the Gauß formula:

$$\frac{1}{V}\int_{\mathcal{B}_{\mathrm{mic}}} \boldsymbol{\sigma}:\dot{\boldsymbol{\varepsilon}}\,\mathrm{d}\Omega = \frac{1}{V}\int_{\partial\mathcal{B}_{\mathrm{mic}}} \mathbf{t}\cdot\dot{\mathbf{u}}\,\mathrm{d}\Gamma. \tag{5.4}$$

By adding and subtracting the term $\overline{\boldsymbol{\sigma}}:\dot{\overline{\boldsymbol{\varepsilon}}}$ to the right hand side (RHS) of (5.3) and by using (5.4), $\mathcal{P}_{\mathrm{m}}$ can be written as

$$\mathcal{P}_{\mathrm{m}} = \frac{1}{V}\int_{\partial\mathcal{B}_{\mathrm{mic}}} \mathbf{t}\cdot\dot{\mathbf{u}}\,\mathrm{d}\Gamma - \overline{\boldsymbol{\sigma}}:\dot{\overline{\boldsymbol{\varepsilon}}} - \overline{\boldsymbol{\sigma}}:\dot{\overline{\boldsymbol{\varepsilon}}} + \overline{\boldsymbol{\sigma}}:\dot{\overline{\boldsymbol{\varepsilon}}}. \tag{5.5}$$

By using the definitions of the average quantities or the boundary integral on the micro level, the mechanical power on the macro level $\overline{\boldsymbol{\sigma}} : \dot{\overline{\boldsymbol{\varepsilon}}}$ can be expressed in three different ways:

$$
\left.
\begin{aligned}
\overline{\boldsymbol{\sigma}} : \dot{\overline{\boldsymbol{\varepsilon}}} &= \overline{\boldsymbol{\sigma}} : \frac{1}{V} \int_{\partial \mathcal{B}_{\mathrm{mic}}} \mathrm{sym}[\dot{\mathbf{u}} \otimes \mathbf{n}] \mathrm{d}\Gamma = \frac{1}{V} \int_{\partial \mathcal{B}_{\mathrm{mic}}} (\overline{\boldsymbol{\sigma}} \mathbf{n}) \cdot \dot{\mathbf{u}} \mathrm{d}\Gamma, \\[2mm]
\overline{\boldsymbol{\sigma}} : \dot{\overline{\boldsymbol{\varepsilon}}} &= \overline{\boldsymbol{\sigma}} : \overline{\dot{\nabla \mathbf{u}}} \\
&= \frac{1}{V} \int_{\partial \mathcal{B}_{\mathrm{mic}}} \mathrm{sym}[\mathbf{t} \otimes \mathbf{x}] \, \mathrm{d}\Gamma : \overline{\dot{\nabla \mathbf{u}}} = \frac{1}{V} \int_{\partial \mathcal{B}_{\mathrm{mic}}} \mathbf{t} \cdot (\overline{\dot{\nabla \mathbf{u}}} \, \mathbf{x}) \, \mathrm{d}\Gamma, \\[2mm]
\overline{\boldsymbol{\sigma}} : \dot{\overline{\boldsymbol{\varepsilon}}} &= \overline{\boldsymbol{\sigma}} : \overline{\dot{\nabla \mathbf{u}}} \\
&= (\overline{\boldsymbol{\sigma}} \frac{1}{V} \int_{\partial \mathcal{B}_{\mathrm{mic}}} \mathbf{n} \otimes \mathbf{x} \, \mathrm{d}\Gamma) : \overline{\dot{\nabla \mathbf{u}}} = \frac{1}{V} \int_{\partial \mathcal{B}_{\mathrm{mic}}} (\overline{\boldsymbol{\sigma}} \mathbf{n}) \cdot (\overline{\dot{\nabla \mathbf{u}}} \, \mathbf{x}) \, \mathrm{d}\Gamma
\end{aligned}
\right\} .
\tag{5.6}
$$

Inserting the different expressions of $\overline{\boldsymbol{\sigma}} : \dot{\overline{\boldsymbol{\varepsilon}}}$ into the right hand side of (5.5) and doing rearrangements, the following equation is deduced:

$$
\begin{aligned}
\mathcal{P}_{\mathrm{m}} &= \frac{1}{V} \int_{\partial \mathcal{B}_{\mathrm{mic}}} \Big[\mathbf{t} \cdot \dot{\mathbf{u}} - (\overline{\boldsymbol{\sigma}} \mathbf{n}) \cdot \dot{\mathbf{u}} - \mathbf{t} \cdot (\overline{\dot{\nabla \mathbf{u}}} \, \mathbf{x}) + (\overline{\boldsymbol{\sigma}} \mathbf{n}) \cdot (\overline{\dot{\nabla \mathbf{u}}} \, \mathbf{x}) \Big] \mathrm{d}\Gamma \\
&= \frac{1}{V} \int_{\partial \mathcal{B}_{\mathrm{mic}}} ((\mathbf{t} - \overline{\boldsymbol{\sigma}} \mathbf{n}) \cdot (\dot{\mathbf{u}} - \overline{\dot{\nabla \mathbf{u}}} \, \mathbf{x})) \, \mathrm{d}\Gamma .
\end{aligned}
\tag{5.7}
$$

As $\mathcal{P}_{\mathrm{m}} = 0$, one of the two terms in the multiplication under the boundary integral in (5.7) must be zero. Thus, from equation (5.7) two types of mechanical boundary conditions for the micro boundary value problem (BVP) are deduced,

$$
\mathbf{t} = \overline{\boldsymbol{\sigma}} \mathbf{n} \qquad \text{or} \qquad \dot{\mathbf{u}} = \overline{\dot{\nabla \mathbf{u}}} \, \mathbf{x} \quad \text{on} \quad \partial \mathcal{B}_{\mathrm{mic}}.
\tag{5.8}
$$

Another possible mechanical boundary condition for the micro scale problem is called periodic boundary condition. This boundary condition allows a fluctuation of $\mathbf{u}$, i.e.

$$
\dot{\mathbf{u}} = \overline{\dot{\nabla \mathbf{u}}} \, \mathbf{x} + \dot{\widetilde{\mathbf{w}}} \qquad \Rightarrow \qquad \nabla \dot{\mathbf{u}} = \overline{\dot{\nabla \mathbf{u}}} + \nabla \dot{\widetilde{\mathbf{w}}},
\tag{5.9}
$$

where $\widetilde{\mathbf{w}}$ denotes the fluctuation of the displacement field at the micro scale relative to the homogeneous term $\overline{\nabla \mathbf{u}} \, \mathbf{x}$. Suppose that the boundary of the representative volume ele-

ment $\partial\mathcal{B}_{\mathrm{mic}}$ can be divided into two parts: one positive boundary $\partial\mathcal{B}_{\mathrm{mic}}^+$ and one negative boundary $\partial\mathcal{B}_{\mathrm{mic}}^-$ as shown in Figure 5.2, whose normal vectors are related by $\mathbf{n}^+ = -\mathbf{n}^-$.
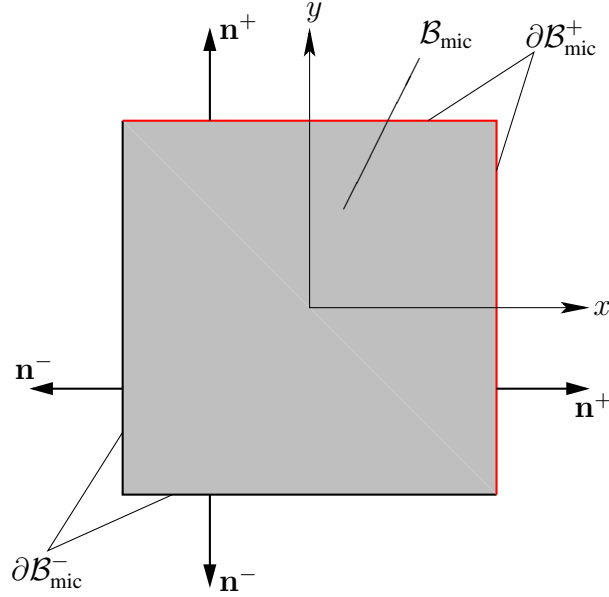
Figure 5.2: *A micro domain or a RVE with the boundary divided into* $\partial\mathcal{B}_{mic}^+$ *and* $\partial\mathcal{B}_{mic}^-$

With the assumption in (5.9), equation (5.7) can be transformed to

$$
\begin{aligned}
\mathcal{P}_{\mathrm{m}} &= \frac{1}{V}\int_{\partial\mathcal{B}_{\mathrm{mic}}}(\mathbf{t} - \overline{\boldsymbol{\sigma}}\mathbf{n})\cdot(\dot{\widetilde{\mathbf{w}}})\,\mathrm{d}\Gamma \\
&= \frac{1}{V}\left[\int_{\partial\mathcal{B}_{\mathrm{mic}}^+}(\mathbf{t}^+ - \overline{\boldsymbol{\sigma}}\mathbf{n}^+)\cdot\dot{\widetilde{\mathbf{w}}}^+\,\mathrm{d}\Gamma + \int_{\partial\mathcal{B}_{\mathrm{mic}}^-}(\mathbf{t}^- - \overline{\boldsymbol{\sigma}}\mathbf{n}^-)\cdot\dot{\widetilde{\mathbf{w}}}^-\,\mathrm{d}\Gamma\right].
\end{aligned}
\tag{5.10}
$$

By further assuming equal fluctuation of the displacement field on the opposite boundaries of $\mathcal{B}_{\mathrm{mic}}$, i.e. $\widetilde{\mathbf{w}}^+ = \widetilde{\mathbf{w}}^-$, equation (5.10) can be simplified to

$$
\mathcal{P}_{\mathrm{m}} = \frac{1}{V}\left[\int_{\partial\mathcal{B}_{\mathrm{mic}}^+}\mathbf{t}^+\cdot\dot{\widetilde{\mathbf{w}}}^+\,\mathrm{d}\Gamma + \int_{\partial\mathcal{B}_{\mathrm{mic}}^-}\mathbf{t}^-\cdot\dot{\widetilde{\mathbf{w}}}^-\,\mathrm{d}\Gamma\right].
\tag{5.11}
$$

To fulfill the Hill-Mandel condition $\mathcal{P}_{\mathrm{m}} = 0$ in equation (5.11), it is essential that $\mathbf{t}^+ = -\mathbf{t}^-$. So, the mechanical periodic boundary condition for $\mathcal{B}_{\mathrm{mic}}$ can be written as

$$
\dot{\widetilde{\mathbf{w}}}^+ = \dot{\widetilde{\mathbf{w}}}^- \qquad \text{and} \qquad \mathbf{t}^+ = -\mathbf{t}^- \qquad \text{on opposite faces of } \partial\mathcal{B}_{\mathrm{mic}}.
\tag{5.12}
$$

5.1.2   Mechanical power incorporating Eshelby stress tensor

In Section 5.1.1 the Hill-Mandel condition is written either in terms of the Cauchy stress tensor $\boldsymbol{\sigma}$ and strain tensor $\boldsymbol{\varepsilon}$ or the Cauchy stress tensor $\boldsymbol{\sigma}$ and the displacement gradient $\nabla \mathbf{u}$. To investigate the consistency of the macro Eshelby stress tensor and the macro configurational forces, the Hill-Mandel condition has to be expressed by the Eshelby stress tensor. In order to obtain the Hill-Mandel condition, the relation between the mechanical power and the Eshelby stress tensor needs to be established. The mechanical power in a small strain setting along with a linear elastic material can be written as

$$
\begin{aligned}
\dot{W} &= \boldsymbol{\sigma} : \nabla \dot{\mathbf{u}} = \boldsymbol{\sigma} \mathbf{1} : \nabla \dot{\mathbf{u}} = (\nabla \dot{\mathbf{u}})^T \boldsymbol{\sigma} : \mathbf{1} \\
&= \left[\left((\nabla \mathbf{u})^T \boldsymbol{\sigma} \right)^{\cdot} - (\nabla \mathbf{u})^T \dot{\boldsymbol{\sigma}} \right] : \mathbf{1} \\
&= \left[(W\mathbf{1} - \boldsymbol{\Sigma})^{\cdot} - (\nabla \mathbf{u})^T \dot{\boldsymbol{\sigma}} \right] : \mathbf{1}, \quad \text{as} \quad \boldsymbol{\Sigma} = W\mathbf{1} - (\nabla \mathbf{u})^T \boldsymbol{\sigma} \\
&= \left[\dot{W}\mathbf{1} - \dot{\boldsymbol{\Sigma}} - (\nabla \mathbf{u})^T \dot{\boldsymbol{\sigma}} \right] : \mathbf{1} \\
&= \dot{W}\mathbf{1} : \mathbf{1} - \dot{\boldsymbol{\Sigma}} : \mathbf{1} - (\nabla \mathbf{u})^T \dot{\boldsymbol{\sigma}} : \mathbf{1} \\
&= 3\dot{W} - \dot{\boldsymbol{\Sigma}} : \mathbf{1} - \dot{\boldsymbol{\sigma}} : \nabla \mathbf{u}, \quad \text{as} \quad \mathbf{1} : \mathbf{1} = 3 \\
&= 3\dot{W} - \dot{\boldsymbol{\Sigma}} : \mathbf{1} - \dot{W}, \quad \text{as} \quad \dot{W} = \boldsymbol{\sigma} : \nabla \dot{\mathbf{u}} = \dot{\boldsymbol{\sigma}} : \nabla \mathbf{u} \\
\Rightarrow \dot{W} &= 2\dot{W} - \dot{\boldsymbol{\Sigma}} : \mathbf{1} \\
\Rightarrow \dot{W} &= \dot{\boldsymbol{\Sigma}} : \mathbf{1} = \operatorname{tr}\dot{\boldsymbol{\Sigma}}, \quad\quad\quad\quad\quad\quad\quad\quad\quad\quad\quad\quad\quad (5.13)
\end{aligned}
$$

in which W is the strain energy density and $\mathbf{1}$ is the second order unit tensor.

So, the mechanical power of the small strain problem with a linear material law can be expressed in terms of the Eshelby stress tensor $\boldsymbol{\Sigma}$ as $\dot{\boldsymbol{\Sigma}} : \mathbf{1}$.

Thus, the Hill-Mandel condition incorporating the Eshelby stress tensor reads

$$
\dot{\boldsymbol{\Sigma}}_{\mathrm{M}} : \mathbf{1} = \frac{1}{V} \int_{\mathcal{B}_{\mathrm{mic}}} \dot{\boldsymbol{\Sigma}} : \mathbf{1} \mathrm{d}\Omega, \quad\quad\quad\quad\quad\quad (5.14)
$$

where the subscript 'M' stands for macro or homogenized quantities.

The macro or homogenized Eshelby stress tensor in a small strain setting can be determined in two different ways: either by using homogenized mechanical quantities (stress tensor and displacement gradient), or by performing a volume average of the Eshelby stress tensor on the micro level. More details on this issue are given in Section 5.2.

Equation (5.14) can be rewritten as

$$
\begin{aligned}
\dot{\boldsymbol{\Sigma}}_{\mathrm{M}} : \mathbf{1} &= \overline{\dot{\boldsymbol{\Sigma}} : \mathbf{1}} \\
&= \overline{\boldsymbol{\sigma} : \nabla \dot{\mathbf{u}}}, \quad \text{as} \quad \dot{W} = \dot{\boldsymbol{\Sigma}} : \mathbf{1} = \boldsymbol{\sigma} : \nabla \dot{\mathbf{u}} \\
&= \overline{\boldsymbol{\sigma}} : \overline{\nabla \dot{\mathbf{u}}}, \quad \text{(Hill-Mandel condition in (5.2)).} \quad (5.15)
\end{aligned}
$$

5.1.3 Boundary conditions of the micro BVP for pure mechanical problem

At this point of the derivation, it is possible to determine the displacement BC or the periodic BC for the micro BVP by using the macro displacement gradient $\overline{\nabla \mathbf{u}}$, or by using the macro strain tensor $\overline{\boldsymbol{\varepsilon}}$.

Macro displacement gradient driven boundary conditions:

The displacement or Dirichlet BC is

$$
\mathbf{u} = \overline{\nabla \mathbf{u}}\, \mathbf{x} \qquad \text{on} \quad \partial \mathcal{B}_{\mathrm{mic}}, \tag{5.16}
$$

and the corresponding micro displacement gradient on the boundary of the micro specimen is

$$
\nabla \mathbf{u} = \overline{\nabla \mathbf{u}} \qquad \text{on} \quad \partial \mathcal{B}_{\mathrm{mic}}. \tag{5.17}
$$

The periodic BC is

$$
\mathbf{u} = \overline{\nabla \mathbf{u}}\, \mathbf{x} + \tilde{\mathbf{w}} \qquad \text{on} \quad \partial \mathcal{B}_{\mathrm{mic}}, \tag{5.18}
$$

and the corresponding micro displacement gradient on the boundary of the micro specimen is

$$
\nabla \mathbf{u} = \overline{\nabla \mathbf{u}} + \nabla \tilde{\mathbf{w}} \qquad \text{on} \quad \partial \mathcal{B}_{\mathrm{mic}}. \tag{5.19}
$$

Macro strain driven boundary conditions:

The displacement or Dirichlet BC is

$$
\mathbf{u} = \overline{\boldsymbol{\varepsilon}}\, \mathbf{x} \qquad \text{on} \quad \partial \mathcal{B}_{\mathrm{mic}}, \tag{5.20}
$$

and the corresponding micro displacement gradient on the boundary of the micro specimen is

$$\nabla \mathbf{u} = \overline{\varepsilon}. \tag{5.21}$$

The periodic BC is

$$\mathbf{u} = \overline{\varepsilon} \, \mathbf{x} + \tilde{\mathbf{w}} \qquad \text{on} \quad \partial \mathcal{B}_{\mathrm{mic}}, \tag{5.22}$$

and the corresponding micro displacement gradient on the boundary of the micro specimen is

$$\nabla \mathbf{u} = \overline{\varepsilon} + \nabla \tilde{\mathbf{w}}. \tag{5.23}$$

5.2   Homogenization of the Eshelby stress tensor

In order to capture the effects of the micro inhomogeneities on the macro Eshelby stress tensor and macro configurational forces, it is essential to homogenize the Eshelby stress tensor. In the case of a large deformation problem, there are three possible different procedures to homogenize the Eshelby stress tensor. The detailed formulation is described by Ricker et al. [84]. In a small deformation setting along with linear material behavior, there are two possible procedures to homogenize the Eshelby stress tensor. In the first procedure, the homogenized Eshelby stress tensor is determined from homogenized mechanical quantities, and in the second procedure, the homogenized Eshelby stress tensor is determined by performing the volume average of the Eshelby stress tensor on the micro level.

5.2.1   Eshelby stress tensor from homogenized quantities

Here the homogenized or macro Eshelby stress is determined by using averaged or macro quantities as

$$\begin{aligned} \mathbf{\Sigma}_{\mathrm{M}} &= W_{\mathrm{M}} \mathbf{1} - (\nabla \mathbf{u}_{\mathrm{M}})^{T} \boldsymbol{\sigma}_{\mathrm{M}} \\ &= \overline{W} \mathbf{1} - (\overline{\nabla \mathbf{u}})^{T} \overline{\boldsymbol{\sigma}}, \end{aligned} \tag{5.24}$$

where W is the strain energy density.

5.2.1.1 Homogenized quantities using macro displacement gradient driven micro boundary conditions

Here the formulation for periodic boundary conditions will be discussed first, and then the results for Dirichlet boundary conditions can easily be obtained by omitting the fluctuation term. By using the averaging definition of the mechanical quantities and considering the absence of body force, equation (5.24) can be written as

$$
\begin{aligned}
\boldsymbol{\Sigma}_{\mathrm{M}} &= \frac{1}{V}\int_{\mathcal{B}_{\mathrm{mic}}} W\mathbf{1}\,\mathrm{d}\Omega - (\overline{\nabla\mathbf{u}})^T\frac{1}{V}\int_{\mathcal{B}_{\mathrm{mic}}}\boldsymbol{\sigma}\,\mathrm{d}\Omega \\
&= \frac{1}{V}\int_{\mathcal{B}_{\mathrm{mic}}} W\mathbf{1}\,\mathrm{d}\Omega - \frac{1}{V}\int_{\mathcal{B}_{\mathrm{mic}}}(\overline{\nabla\mathbf{u}})^T\boldsymbol{\sigma}\,\mathrm{d}\Omega \\
&= \frac{1}{V}\int_{\mathcal{B}_{\mathrm{mic}}} W\mathbf{1}\,\mathrm{d}\Omega - \frac{1}{V}\int_{\mathcal{B}_{\mathrm{mic}}}(\nabla\mathbf{u} - \nabla\tilde{\mathbf{w}})^T\boldsymbol{\sigma}\,\mathrm{d}\Omega \\
&= \frac{1}{V}\int_{\mathcal{B}_{\mathrm{mic}}}(W\mathbf{1} - (\nabla\mathbf{u})^T\boldsymbol{\sigma})\,\mathrm{d}\Omega + \frac{1}{V}\int_{\mathcal{B}_{\mathrm{mic}}}(\nabla\tilde{\mathbf{w}})^T\boldsymbol{\sigma}\,\mathrm{d}\Omega \\
&= \frac{1}{V}\int_{\mathcal{B}_{\mathrm{mic}}}\boldsymbol{\Sigma}\,\mathrm{d}\Omega + \frac{1}{V}\int_{\mathcal{B}_{\mathrm{mic}}}(\nabla\tilde{\mathbf{w}})^T\boldsymbol{\sigma}\,\mathrm{d}\Omega \\
&= \overline{\boldsymbol{\Sigma}} + \frac{1}{V}\int_{\mathcal{B}_{\mathrm{mic}}}(\nabla\tilde{\mathbf{w}})^T\boldsymbol{\sigma}\,\mathrm{d}\Omega. \tag{5.25}
\end{aligned}
$$

The relation between the macro Eshelby stress tensor and the volume average of the Eshelby stress tensor is

$$
\boldsymbol{\Sigma}_{\mathrm{M}} = \overline{\boldsymbol{\Sigma}} + \frac{1}{V}\int_{\mathcal{B}_{\mathrm{mic}}}(\nabla\tilde{\mathbf{w}})^T\boldsymbol{\sigma}\,\mathrm{d}\Omega. \tag{5.26}
$$

In the case of Dirichlet BC for the micro problem, $\nabla\tilde{\mathbf{w}} = \mathbf{0}$, which leads to $\boldsymbol{\Sigma}_{\mathrm{M}} = \overline{\boldsymbol{\Sigma}}$. The macro Eshelby stress tensor is equivalent to the volume average of the Eshelby stress tensor.

The Hill-Mandel condition reads

$$
\begin{aligned}
\boldsymbol{\Sigma}_{\mathrm{M}}:\mathbf{1} &= (\overline{\boldsymbol{\Sigma}} + \frac{1}{V}\int_{\mathcal{B}_{\mathrm{mic}}}(\nabla\tilde{\mathbf{w}})^T\boldsymbol{\sigma}\,\mathrm{d}\Omega):\mathbf{1} \\
&= \overline{\boldsymbol{\Sigma}}:\mathbf{1} + \frac{1}{V}\int_{\mathcal{B}_{\mathrm{mic}}}\left[(\nabla\tilde{\mathbf{w}})^T\boldsymbol{\sigma}\right]:\mathbf{1}\,\mathrm{d}\Omega \\
&= \overline{\boldsymbol{\Sigma}}:\mathbf{1} + \frac{1}{V}\int_{\mathcal{B}_{\mathrm{mic}}}\boldsymbol{\sigma}:\nabla\tilde{\mathbf{w}}\,\mathrm{d}\Omega \\
&= \overline{\boldsymbol{\Sigma}:\mathbf{1}} + \frac{1}{V}\int_{\mathcal{B}_{\mathrm{mic}}}\boldsymbol{\sigma}:\nabla\tilde{\mathbf{w}}\,\mathrm{d}\Omega. \tag{5.27}
\end{aligned}
$$

In the case of Dirichlet or displacement type BC, $\nabla\tilde{\mathbf{w}} = \mathbf{0}$, which infers $\boldsymbol{\Sigma}_{\mathrm{M}}\colon \mathbf{1} = \overline{\boldsymbol{\Sigma}\colon \mathbf{1}}$. So, the Hill-Mandel condition is satisfied.

5.2.1.2 Homogenized quantities using macro strain driven micro boundary conditions

Again by using the averaging definition on the mechanical quantities, equation (5.24) can be written as

$$
\begin{aligned}
\boldsymbol{\Sigma}_{\mathrm{M}} &= \frac{1}{V}\int_{\mathcal{B}_{\mathrm{mic}}} W\mathbf{1}\,\mathrm{d}\Omega - (\nabla\mathbf{u}_{\mathrm{M}})^{T}\frac{1}{V}\int_{\mathcal{B}_{\mathrm{mic}}}\boldsymbol{\sigma}\,\mathrm{d}\Omega \\
&= \frac{1}{V}\int_{\mathcal{B}_{\mathrm{mic}}} W\mathbf{1}\,\mathrm{d}\Omega - \frac{1}{V}\int_{\mathcal{B}_{\mathrm{mic}}}(\overline{\nabla\mathbf{u}})^{T}\boldsymbol{\sigma}\,\mathrm{d}\Omega \\
&= \frac{1}{V}\int_{\mathcal{B}_{\mathrm{mic}}} W\mathbf{1}\,\mathrm{d}\Omega - \frac{1}{V}\int_{\mathcal{B}_{\mathrm{mic}}}(\overline{\boldsymbol{\varepsilon}}+\overline{\boldsymbol{\omega}})^{T}\boldsymbol{\sigma}\,\mathrm{d}\Omega \qquad \left(\text{where } \boldsymbol{\omega}=\frac{1}{2}\left(\nabla\mathbf{u}-(\nabla\mathbf{u})^{T}\right)\right) \\
&= \frac{1}{V}\int_{\mathcal{B}_{\mathrm{mic}}} W\mathbf{1}\,\mathrm{d}\Omega - \frac{1}{V}\int_{\mathcal{B}_{\mathrm{mic}}}(\nabla\mathbf{u}+\overline{\boldsymbol{\omega}}-\nabla\tilde{\mathbf{w}})^{T}\boldsymbol{\sigma}\,\mathrm{d}\Omega \\
&= \frac{1}{V}\int_{\mathcal{B}_{\mathrm{mic}}}(W\mathbf{1}-(\nabla\mathbf{u})^{T}\boldsymbol{\sigma})\,\mathrm{d}\Omega - \frac{1}{V}\int_{\mathcal{B}_{\mathrm{mic}}}\overline{\boldsymbol{\omega}}^{T}\boldsymbol{\sigma}\,\mathrm{d}\Omega + \frac{1}{V}\int_{\mathcal{B}_{\mathrm{mic}}}(\nabla\tilde{\mathbf{w}})^{T}\boldsymbol{\sigma}\,\mathrm{d}\Omega \\
&= \frac{1}{V}\int_{\mathcal{B}_{\mathrm{mic}}}\boldsymbol{\Sigma}\,\mathrm{d}\Omega - \frac{1}{V}\int_{\mathcal{B}_{\mathrm{mic}}}\overline{\boldsymbol{\omega}}^{T}\boldsymbol{\sigma}\,\mathrm{d}\Omega + \frac{1}{V}\int_{\mathcal{B}_{\mathrm{mic}}}(\nabla\tilde{\mathbf{w}})^{T}\boldsymbol{\sigma}\,\mathrm{d}\Omega \\
&= \overline{\boldsymbol{\Sigma}} - \frac{1}{V}\int_{\mathcal{B}_{\mathrm{mic}}}\overline{\boldsymbol{\omega}}^{T}\boldsymbol{\sigma}\,\mathrm{d}\Omega + \frac{1}{V}\int_{\mathcal{B}_{\mathrm{mic}}}(\nabla\tilde{\mathbf{w}})^{T}\boldsymbol{\sigma}\,\mathrm{d}\Omega.
\end{aligned}
\tag{5.28}
$$

The relation between the macro Eshelby stress tensor and the volume average of the Eshelby stress tensor is

$$
\boldsymbol{\Sigma}_{\mathrm{M}} = \overline{\boldsymbol{\Sigma}} - \frac{1}{V}\int_{\mathcal{B}_{\mathrm{mic}}}\overline{\boldsymbol{\omega}}^{T}\boldsymbol{\sigma}\,\mathrm{d}\Omega + \frac{1}{V}\int_{\mathcal{B}_{\mathrm{mic}}}(\nabla\tilde{\mathbf{w}})^{T}\boldsymbol{\sigma}\,\mathrm{d}\Omega.
\tag{5.29}
$$

In the case of Dirichlet BC for the micro problem, $\nabla\tilde{\mathbf{w}} = \mathbf{0}$, which leads to $\boldsymbol{\Sigma}_{\mathrm{M}} = \overline{\boldsymbol{\Sigma}} - \frac{1}{V}\int_{\mathcal{B}_{\mathrm{mic}}}\overline{\boldsymbol{\omega}}^{T}\boldsymbol{\sigma}\,\mathrm{d}\Omega$. The macro Eshelby stress tensor is not equivalent to the volume average of the Eshelby stress tensor.

The Hill-Mandel condition reads

$$
\begin{aligned}
\boldsymbol{\Sigma}_{\mathrm{M}}\colon \mathbf{1} &= (\overline{\boldsymbol{\Sigma}} - \frac{1}{V}\int_{\mathcal{B}_{\mathrm{mic}}}\overline{\boldsymbol{\omega}}^{T}\boldsymbol{\sigma}\,\mathrm{d}\Omega + \frac{1}{V}\int_{\mathcal{B}_{\mathrm{mic}}}(\nabla\tilde{\mathbf{w}})^{T}\boldsymbol{\sigma}\,\mathrm{d}\Omega)\colon \mathbf{1} \\
&= \overline{\boldsymbol{\Sigma}}\colon \mathbf{1} - \frac{1}{V}\int_{\mathcal{B}_{\mathrm{mic}}}\left[\overline{\boldsymbol{\omega}}^{T}\boldsymbol{\sigma}\right]\colon \mathbf{1}\,\mathrm{d}\Omega + \frac{1}{V}\int_{\mathcal{B}_{\mathrm{mic}}}\left[(\nabla\tilde{\mathbf{w}})^{T}\boldsymbol{\sigma}\right]\colon \mathbf{1}\,\mathrm{d}\Omega
\end{aligned}
$$

$$\begin{aligned} &= \overline{\boldsymbol{\Sigma}} \colon \mathbf{1} + \frac{1}{V}\int_{\mathcal{B}_{\text{mic}}} \boldsymbol{\sigma} \colon \nabla\tilde{\mathbf{w}} \, \mathrm{d}\Omega, \quad \text{as} \quad \left[\overline{\boldsymbol{\omega}}^T \boldsymbol{\sigma}\right] \colon \mathbf{1} = 0 \\ &= \overline{\boldsymbol{\Sigma} \colon \mathbf{1}} + \frac{1}{V}\int_{\mathcal{B}_{\text{mic}}} \boldsymbol{\sigma} \colon \nabla\tilde{\mathbf{w}} \, \mathrm{d}\Omega. \end{aligned} \tag{5.30}$$

In the case of Dirichlet or displacement type BC, $\nabla\tilde{\mathbf{w}} = \mathbf{0}$, this infers $\boldsymbol{\Sigma}_{\text{M}} \colon \mathbf{1} = \overline{\boldsymbol{\Sigma} \colon \mathbf{1}}$. So, the Hill-Mandel condition is satisfied.

5.2.2 Macro Eshelby stress tensor as the volume average of micro Eshelby stress tensor

Here the homogenized or macro Eshelby stress tensor is determined by taking the volume average of the Eshelby stress tensor on the micro level. The macro Eshelby stress tensor is defined as

$$\boldsymbol{\Sigma}_{\text{M}} = \overline{\boldsymbol{\Sigma}} = \frac{1}{V}\int_{\mathcal{B}_{\text{mic}}} \boldsymbol{\Sigma} \, \mathrm{d}\Omega. \tag{5.31}$$

For the convenience of the formulations in the following section, index notation has been used. With index notation, equation (5.31) can be written as

$$(\boldsymbol{\Sigma}_{\text{M}})_{ij} = \overline{\boldsymbol{\Sigma}}_{ij} = \frac{1}{V}\int_{\mathcal{B}_{\text{mic}}} \boldsymbol{\Sigma}_{ij} \, \mathrm{d}\Omega. \tag{5.32}$$

The Hill-Mandel condition is easily satisfied in the following way,

$$\boldsymbol{\Sigma}_{\text{M}} \colon \mathbf{1} = \overline{\boldsymbol{\Sigma}} \colon \mathbf{1} = \left(\frac{1}{V}\int_{\mathcal{B}_{\text{mic}}} \boldsymbol{\Sigma} \, \mathrm{d}\Omega\right) \colon \mathbf{1} = \frac{1}{V}\int_{\mathcal{B}_{\text{mic}}} \left(\boldsymbol{\Sigma} \colon \mathbf{1}\right) \mathrm{d}\Omega = \overline{\boldsymbol{\Sigma} \colon \mathbf{1}}. \tag{5.33}$$

It can be concluded that the Hill-Mandel condition is satisfied if the macro Eshelby stress tensor is determined by averaging the Eshelby stress tensor on the micro level. This procedure is independent of the micro boundary conditions. This means that the Hill-Mandel condition is fulfilled for the micro boundary conditions determined either by using the macro displacement gradient or by using the macro strain tensor.

5.3   Balance of the homogenized configurational forces

In this section the balance of macro configurational forces is studied. As the homogenized Eshelby stress tensor determined by averaging the micro Eshelby stress tensor satisfies the Hill-Mandel condition, this macro Eshelby stress tensor will be considered for the balance law.

5.3.1   Macro displacement gradient based deformation of the micro domain

The micro domain is deformed according to the macro displacement gradient. Both types of micro boundary conditions, Dirichlet and periodic boundary conditions, are used to perform the homogenization process. Taking the divergence of both sides of equation (5.32) leads to

$$
\begin{aligned}
\overline{\Sigma}_{ij,j} &= \frac{1}{V}\int_{\mathcal{B}_{\mathrm{mic}}} \Sigma_{ij,j}\, \mathrm{d}\Omega \\
&= \frac{1}{V}\int_{\partial\mathcal{B}_{\mathrm{mic}}} \Sigma_{ij} n_j\, \mathrm{d}\Gamma \qquad \text{(according to divergence theorem).}
\end{aligned} \tag{5.34}
$$

Mathematical manipulations in equation (5.34) gives (see Appendix A.3.1)

$$
\begin{aligned}
\overline{\Sigma}_{ij,j} &= \overline{W}_{,i} - \overline{u}_{k,ij}\overline{\sigma}_{kj} \\
&= 0 \quad \text{(as} \quad \overline{W}_{,i} - \overline{u}_{k,ij}\overline{\sigma}_{kj} = \overline{g}_i = 0).
\end{aligned} \tag{5.35}
$$

In this case there are no unphysical volume configurational forces on the macro level.

5.3.2   Macro strain based deformation of the micro domain

Here the micro domain is deformed according to the macro strain. Similarly, by taking the divergence of both sides of equation (5.32) and mathematical manipulation (see Appendix A.3.2) leads to

$$
\overline{\Sigma}_{ij,j} = \frac{1}{V}\int_{\mathcal{B}_{\mathrm{mic}}} \Sigma_{ij,j}\, \mathrm{d}\Omega
$$

$$
\begin{aligned}
&= \overline{\omega}_{ki,j} \frac{1}{V} \int_{\mathcal{B}_{\text{mic}}} \sigma_{kj} \, \mathrm{d}\Omega \\
&= \overline{\omega}_{ki,j} \overline{\sigma}_{kj}.
\end{aligned}
\tag{5.36}
$$

If the macro strain tensor is used to determine the boundary conditions on the micro level, there are unphysical volume configurational forces on the macro level as in equation (5.36), $\overline{g}_i = -\overline{\omega}_{ki,j}\overline{\sigma}_{kj}$. This phenomenon is also seen in the numerical results of the homogenization for a small strain problem.

5.4   Numerical results and analyses

In this chapter the main focus is to establish a numerical technique which is capable of capturing the effect of micro inhomogeneities in the elastic material on the macro responses. Here the configurational forces at the crack tip of the macro domain are calculated to check the homogenization of configurational forces. The aim is to figure out the influence of the underlying microstructure on the configurational force at the crack tip of a macro specimen. In a real life problem, the underlying microstructures containing interfaces, grains, grain boundaries, micro defects, etc. are very complex in nature. Capturing the influences of the whole scenario of the underlying microstructures is a computationally expensive task or in some cases impossible. To understand the characteristic behaviour of the microstructures, it is sufficient to restrict attention to simplified micro domains with different orientations of the interfaces, micro cracks and grains.

5.4.1   Macro geometry and material parameters

A 4 mm×4 mm macro specimen with a sharp crack (see Figure 5.3) is simulated to determine the configurational forces at the crack tip with different micro domains at every Gauß point of the macro domain. The length of the crack is 2 mm and the width of the crack at the opening is 0.1 mm. In all simulations the bottom boundary of the macro domain remains fixed and the top boundary is displaced by 0.1 mm.
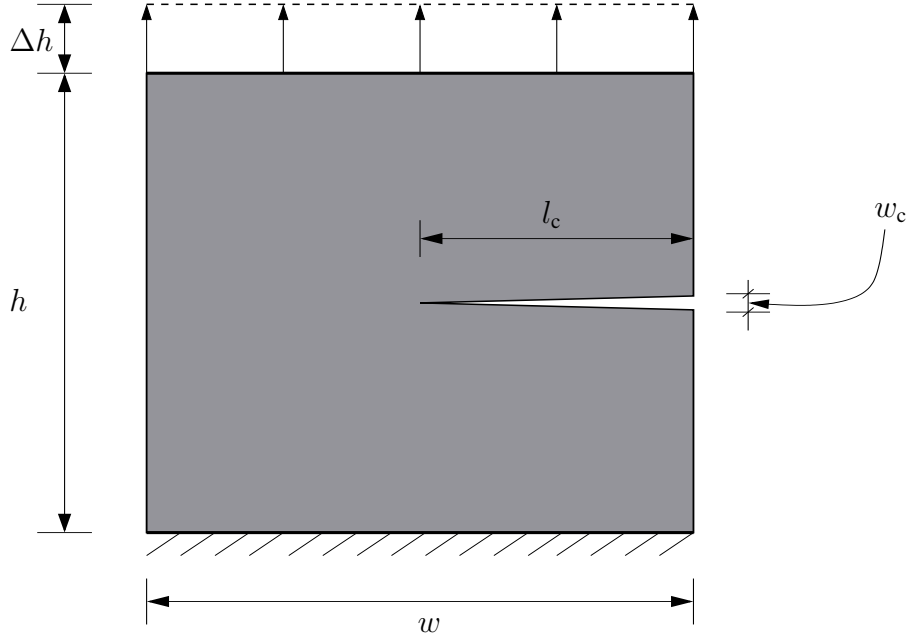
Figure 5.3: *A fractured macro specimen with dimension $h \times w$ containing a sharp crack (with crack length l_c and width at the opening w_c), the top of the structure is displaced by Δh*

All simulations in this chapter are carried out by using the following material parameter,

$$\underline{\mathbb{C}} = \begin{bmatrix} 12.6 & 5.3 & 0.0 \\ 5.3 & 12.6 & 0.0 \\ 0.0 & 0.0 & 3.53 \end{bmatrix} \cdot 10^4 \frac{\text{N}}{\text{mm}^2}. \tag{5.37}$$

When it is required to define two different materials, the values of $\underline{\mathbb{C}}$ in equation (5.37) is considered as the material parameter for the material with high stiffness and the material with low stiffness is assigned with the material parameter of $\underline{\mathbb{C}}/20$.

5.4.2   Simulation with an inhomogeneous micro domain

Figure 5.4 shows the nodal configurational forces which are produced from two different types of boundary conditions for the micro problem. In the first case, the boundary condition is determined by using $\mathbf{u}_b = \overline{\boldsymbol{\varepsilon}}\,\mathbf{x}_b$ (Figure 5.4(b) and 5.4(d)), and in the second case by using $\mathbf{u}_b = \overline{\nabla\mathbf{u}}\,\mathbf{x}_b$ (Figure 5.4(c) and 5.4(e)). The microstructure as shown in Figure 5.4(a) contains two different materials with a diagonal sharp interface. Figure 5.4(b) and 5.4(c) display the deformed macro domain with nodal configurational forces. Fig-

ure 5.4(d) and 5.4(e) show the zoomed crack tip vicinity with nodal configurational forces. From the theory of configurational forces, it is obvious that there should appear a large
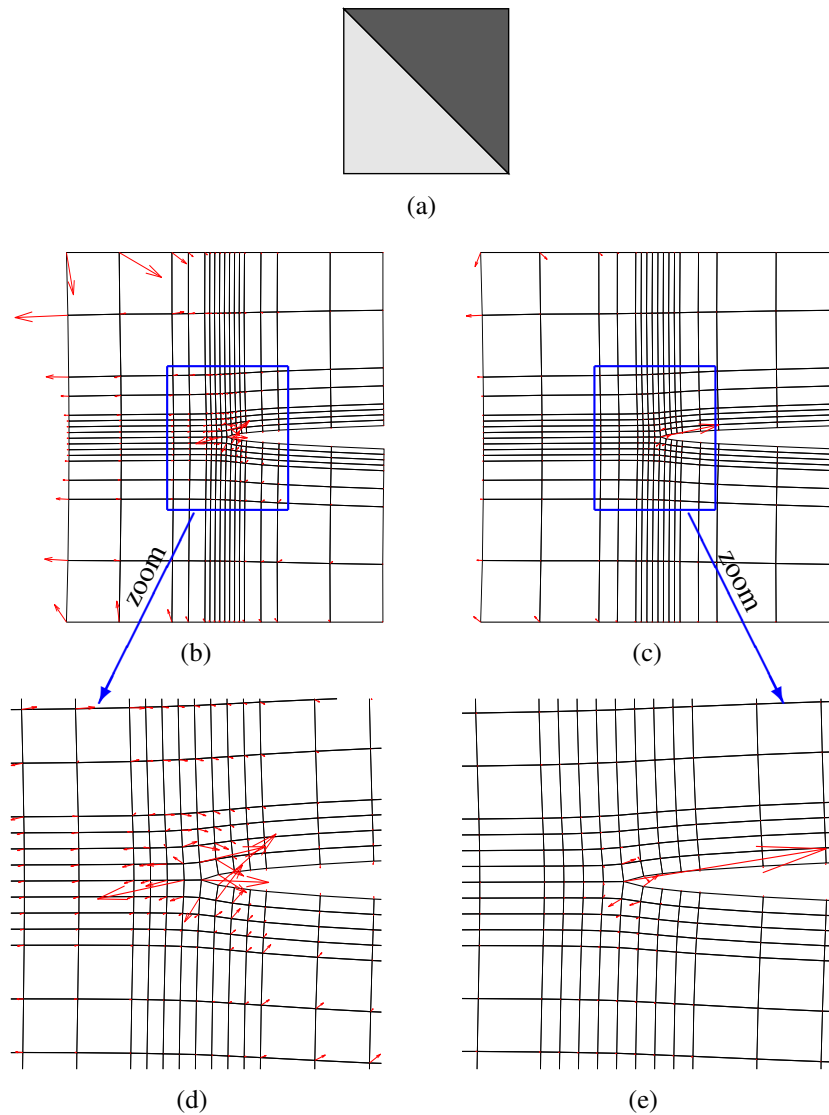
Figure 5.4: *Crack tip configurational forces on the macro level produced from (c) & (e) displacement gradient and (b) & (d) strain driven deformation of the inhomogeneous micro domain (a)*

configurational force at the crack tip node of the macro domain. But in Figure 5.4(d), a larger nodal configurational force at a node different from the one at the crack tip node is visible. This observation is not compatible with the configurational force theory or with fracture mechanics. On the other hand, it is easily visible in Figure 5.4(e) that the configurational force at the crack tip node is the largest one. This is produced from a dis-

placement gradient driven deformed micro domain based computational homogenization. The strain driven homogenization does not produce the largest configurational force at the crack tip, because it produces volume configurational forces on the macro level, even the micro domain is homogeneous and free of physical body force, see equation (5.36).

5.4.3   Simulation with a homogeneous micro domain
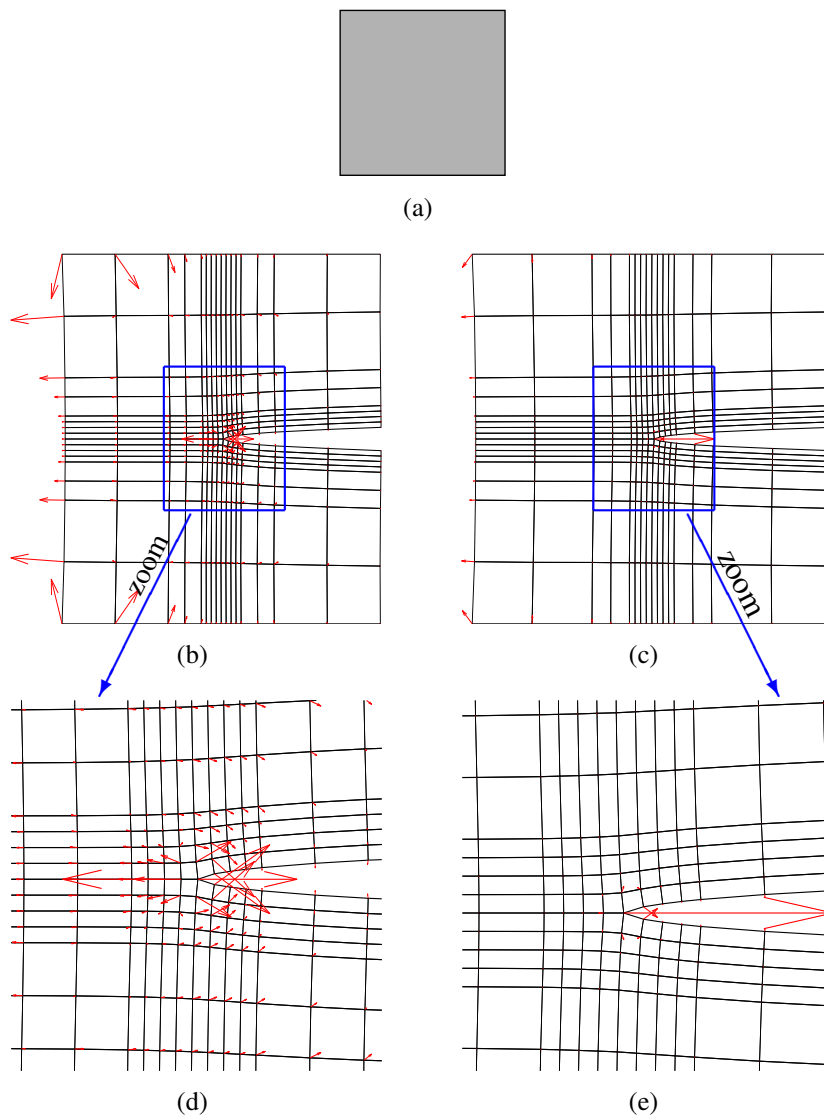
Figure 5.5: *Crack tip configurational forces on the macro level produced from (c) & (e) displacement gradient and (b) & (d) strain driven deformation of the homogeneous micro domain (a)*

The simulation results shown in Figure 5.4 are produced by using an inhomogeneous microstructure, but the results displayed in Figure 5.5 are generated by using a homogeneous micro domain. In this situation the simulation results also exhibit a similar scenario as in Section 5.4.2.

5.4.4 Physical interpretation

For a closer investigation of the difference between displacement gradient based and strain based BCs, the deformations of the microstructure under three different types of BCs (Figure 5.6) are studied: the macro strain tensor ($\mathbf{u}_b = \overline{\boldsymbol{\varepsilon}}\,\mathbf{x}_b$); the macro displacement gradient ($\mathbf{u}_b = \overline{\nabla\mathbf{u}}\,\mathbf{x}_b$); and the rotational or anti-symmetric part of the macro displacement gradient ($\mathbf{u}_b = \overline{\boldsymbol{\omega}}\,\mathbf{x}_b$), where

$$\overline{\boldsymbol{\varepsilon}} = \frac{1}{2}\left(\overline{\nabla\mathbf{u}} + (\overline{\nabla\mathbf{u}})^T\right) \quad \text{and} \quad \overline{\boldsymbol{\omega}} = \frac{1}{2}\left(\overline{\nabla\mathbf{u}} - (\overline{\nabla\mathbf{u}})^T\right).$$

If the micro domain is deformed according to the macro displacement gradient $\overline{\nabla\mathbf{u}}$, the micro deformation follows the macro deformation in a compatible manner. But in the case of the micro deformation using the macro strain tensor $\overline{\boldsymbol{\varepsilon}}$, the rotational part of the macro displacement gradient is omitted. This means that the rotation is restricted at every macro Gauß point. For such reason large configurational forces at internal nodes as well as at the crack tip node appear as a reaction to this constraint.
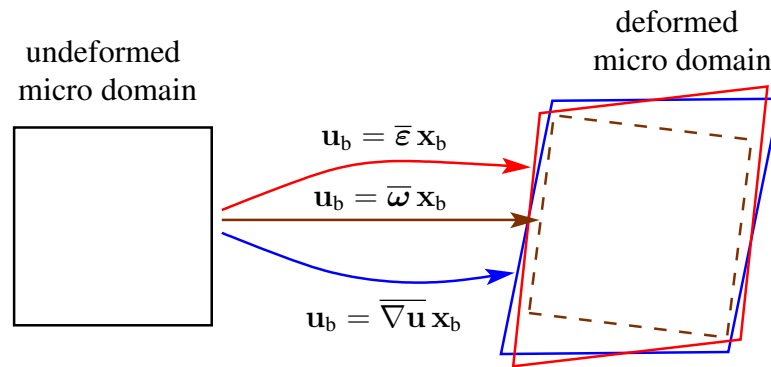
Figure 5.6: *Deformed micro domain with different boundary conditions on the micro level*

5.4.5   Influence of the micro domain

In Figure 5.7 and 5.8, the diagrams in the top row are the micro domains assigned to each Gauß point of the macro domain, and in the second row the deformed macro domains with configurational forces at the crack tip are displayed. At the bottom the numerical values of the configurational forces at the crack tip are reported. The arrows at the crack tips of the macro domains indicate the direction and the value of the configurational forces. The significance of the configurational forces is that the crack propagates in the opposite direction of the configurational force.

$$\mathbf{G} = \begin{bmatrix} 299.76 \\ 0.000 \end{bmatrix} \mathbf{N}, \qquad \mathbf{G} = \begin{bmatrix} 104.15 \\ 21.39 \end{bmatrix} \mathbf{N}, \qquad \mathbf{G} = \begin{bmatrix} 104.15 \\ 21.39 \end{bmatrix} \mathbf{N}$$
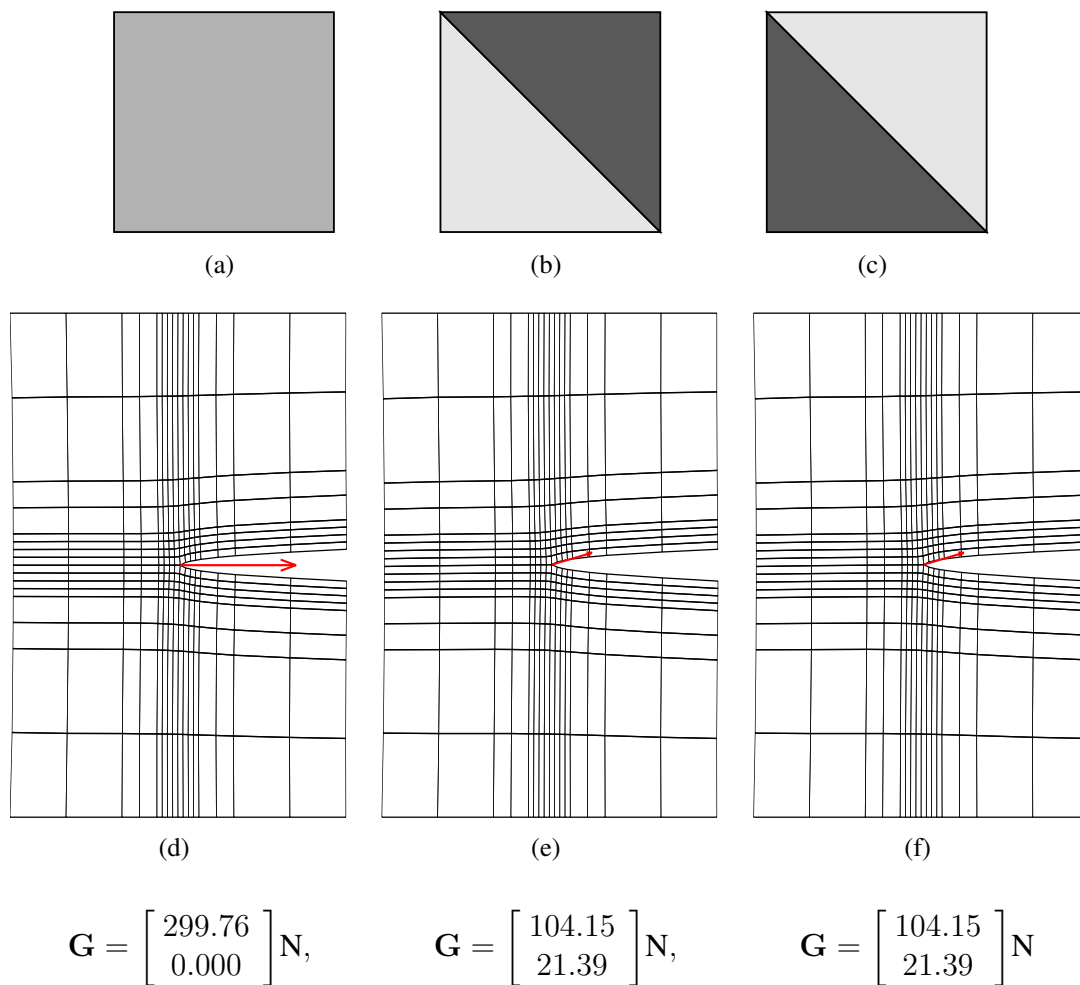
Figure 5.7: *Configurational forces for different microstructures by using displacement gradient driven deformation of the micro domain*

Figure 5.7(a) and 5.7(d) show that if the assigned micro domain is homogeneous, there is a horizontal configurational force of 299.76 N. In Figure 5.7(b) the assigned microstructure has two different materials which are separated by a diagonal sharp interface. In this case the configurational force has a vertical and a horizontal component, see Figure 5.7(e). In Figure 5.7(c) the assigned microstructure is similar to the one in Figure 5.7(b), the difference is that two materials swapped their position. In this case the configurational force is similar to Figure 5.7(e). This means that the configurational force does not depend on the location of the materials but on the orientation of the interface.

(a) (b) (c)

(d) (e) (f)

$$\mathbf{G} = \begin{bmatrix} 151.51 \\ 0.000 \end{bmatrix} \mathbf{N}, \qquad \mathbf{G} = \begin{bmatrix} 104.15 \\ -21.39 \end{bmatrix} \mathbf{N}, \qquad \mathbf{G} = \begin{bmatrix} 104.15 \\ -21.39 \end{bmatrix} \mathbf{N}$$
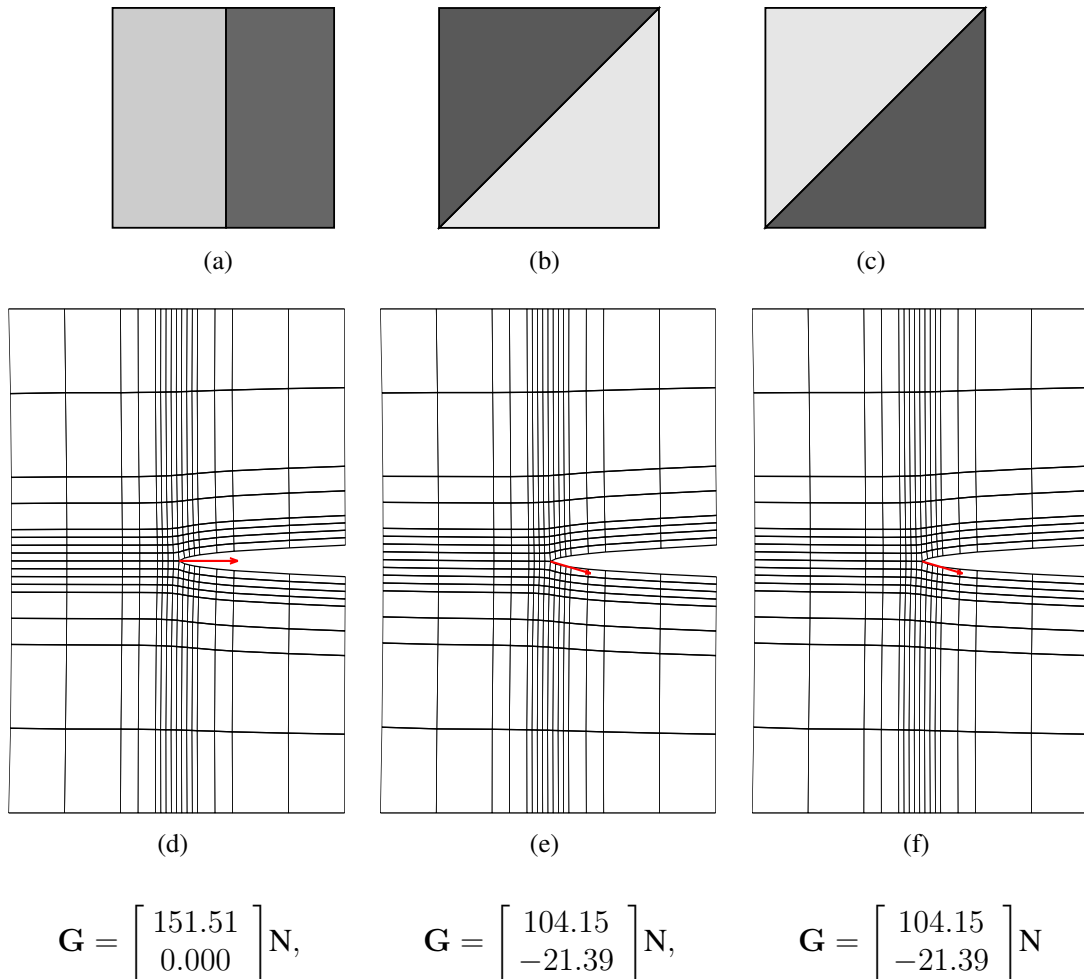
Figure 5.8: *Configurational forces for different microstructures by using displacement gradient driven deformation of the micro domain*

The simulation results in Figure 5.8(d) are generated by using a microstructure shown in Figure 5.8(a) with a vertical interface which separates the two materials. The results in

Figure 5.8(e) and 5.8(f) are produced by using a microstructure (see Figure 5.8(b) and 5.8(c)) with a diagonal interface. This interface is not the same diagonal as that in Figure 5.7(b) and 5.7(c). Figure 5.8(d) shows no vertical component in the configurational force, but in Figure 5.8(e) and 5.8(f) the configurational forces contain a vertical component. Now it can be deduced that there exists a vertical component in the configurational forces when the micro domain includes inclined interfaces.

5.4.6   Influence of the volume fraction

(a)

(b)
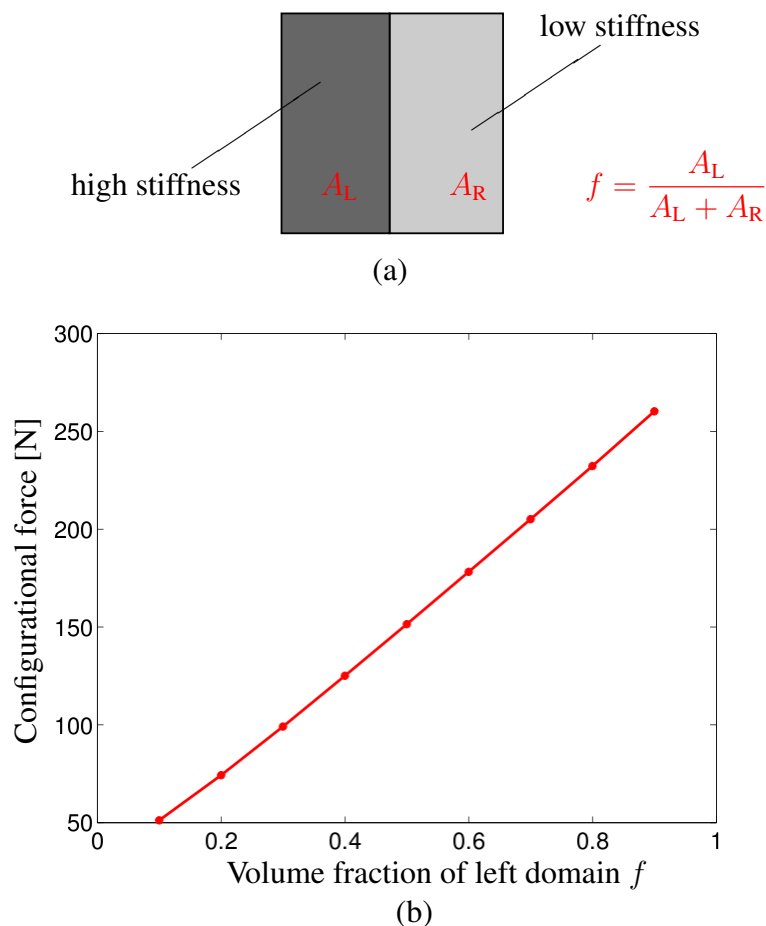
Figure 5.9: *Configurational forces for different volume fractions of the parts of the micro domain*

In this section the effect of the volume fraction of the materials of the microstructure is investigated. The microstructure in Figure 5.9(a) contains two materials of different elastic modulus with a vertical sharp interface. The material in the left domain has a

higher elastic modulus. Figure 5.9(b) shows that the absolute value of the configurational force at the crack tip varies approximately linearly with the variation of the left domain fraction. It results in a higher value of the configurational force for a higher volume fraction of the left domain. The reason is that an increment of the volume fraction of the left domain increases the macroscopic modulus of elasticity.

5.4.7 Influence of the ratio of the elastic moduli

In this section the position of the interface in the microstructure is kept at a fixed position as shown in Figure 5.10(a). The elastic moduli of these two materials are varied in such a way that the volume average of the elastic modulus remains constant.
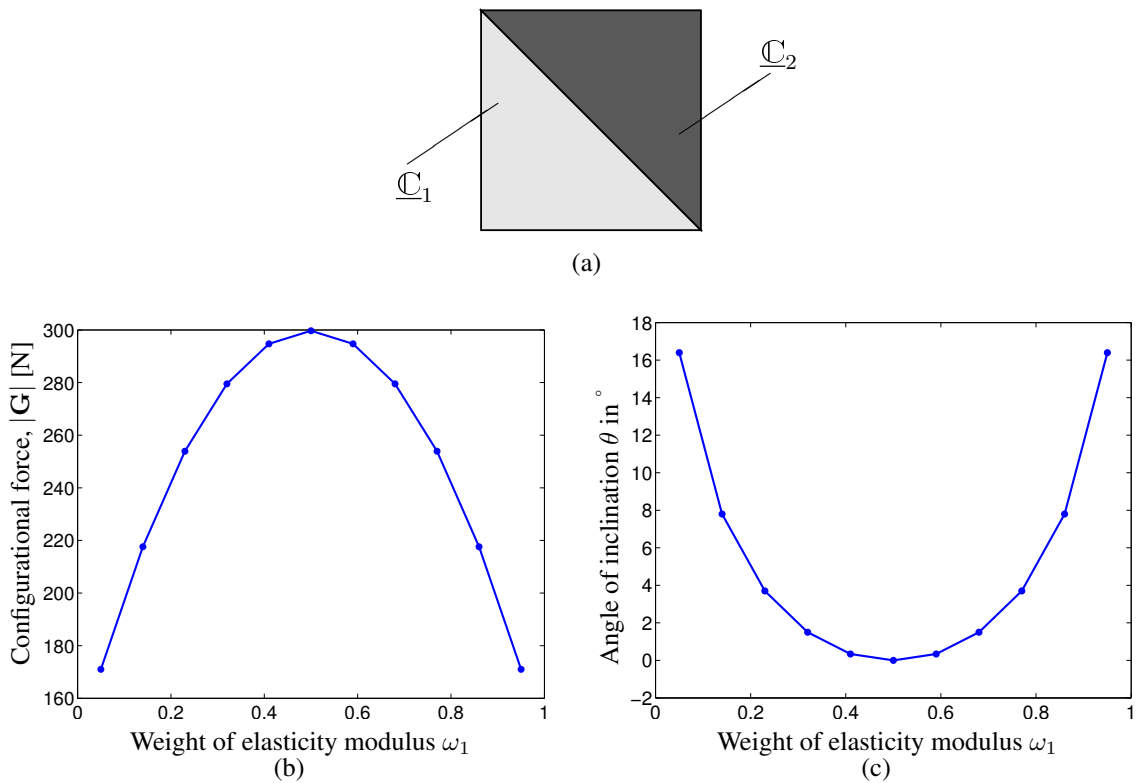
Figure 5.10: *Configurational forces for different ratios of elastic moduli*

The volume average of elastic modulus is defined as $\overline{\mathbb{C}} = (\mathbb{C}_1 + \mathbb{C}_2)/2$. Here $\underline{\mathbb{C}}_1$ is the elastic modulus of the lower triangle of the microstructure, and $\underline{\mathbb{C}}_2$ is the elastic modulus of the upper triangle of the microstructure. And $\underline{\mathbb{C}}_1 = 2\omega_1\overline{\mathbb{C}}$; $\underline{\mathbb{C}}_2 = 2(1-\omega_1)\overline{\mathbb{C}}$, where the weighting factor ω_1 takes a value between 0 and 1. The material parameter

in in equation (5.37) is used as the average of the elastic modulus $\overline{\mathbb{C}}$. Figure 5.10(b) shows the absolute value of the crack tip configurational force with respect to the weighting factor ω_1. The configurational force is the same for the pair of the weighting factors $(\omega_1, 1\text{-}\omega_1)$. In Figure 5.10(c) a similar observation is seen for the inclination angle of the configurational force. If the contribution of the elastic modulus from one material to the total elastic modulus is very small, the slope is larger. The slope becomes smaller if the weight ω_1 tends to 0.5. A weighting factor of 0.5 means that the microstructure is homogeneous, and this produces the largest configurational force at the crack tip. Table 5.1 shows the numerical results related to the plots in Figure 5.10.

Weighting factor(ω_1)	0.05	0.14	0.23	0.32	0.41	0.5	0.59	0.68	0.77	0.86	0.95
G_x, G_y in N	163.9	215.6	253.4	279.4	294.7	299.7	294.7	279.4	253.4	215.6	163.9
	48.4	29.5	16.2	7.1	1.8	0.0	1.8	7.1	16.2	29.5	48.4
$\|\mathbf{G}\|$	171.0	217.6	253.9	279.5	294.7	299.7	294.7	279.5	253.9	217.6	171.0
angle (θ) in °	16.4	7.8	3.7	1.5	0.34	0.0	0.34	1.5	3.7	7.8	16.4

Table 5.1: *Configurational forces for different value of the weighting factor ω_1*

Chapter 6

Homogenization of piezoelectric materials

In this chapter the FE^2-based homogenization technique of the mechanical and electrical quantities as well as the material parameters of piezoelectric materials is presented. An additional task in this chapter is to determine the homogenized configurational forces for microscopically inhomogeneous piezoelectric materials. Since piezoelectric materials exhibit small deformations, all formulations in the previous chapter regarding the homogenization of configurational forces will be taken into consideration. Following the conclusion obtained in Chapter 5, the macro displacement gradient driven boundary conditions on the micro domains will be used for the homogenization of the mechanical part of piezoelectric materials in order to obtain physically compatible configurational forces on the macro level. To prescribe the relevant admissible boundary conditions on the RVEs, one needs to pass at each Gauß point either the macro displacement gradient and the macro electric field, or the macro stress tensor and the macro electric displacement down to the micro level.

With the help of these boundary conditions, one solves the micro boundary value problem of piezoelectric materials and determines the remaining quantities such as the average stress tensor and electric displacement, or the average displacement gradient and electric field, respectively. These averaged quantities as well as the homogenized material parameters are passed back to the macro level as the material response. By using these homogenized material parameters, the macro problem is solved and the required physical quantities are determined on the macro level. In the homogenization procedure, the Es-

helby stress tensor is also averaged on the micro level and passed back to the macro level to determine the nodal configurational forces.

In absence of the body forces and volume charges on the micro level, the transition between the macro and the micro quantities is given as

$$\overline{\boldsymbol{\varepsilon}} \;=\; \frac{1}{V}\int_{\mathcal{B}_{\text{mic}}} \boldsymbol{\varepsilon}\, d\Omega = \frac{1}{V}\int_{\partial\mathcal{B}_{\text{mic}}} \text{sym}(\mathbf{u}\otimes\mathbf{n})\, d\Gamma, \quad \overline{\boldsymbol{\sigma}} = \frac{1}{V}\int_{\mathcal{B}_{\text{mic}}} \boldsymbol{\sigma}\, d\Omega = \frac{1}{V}\int_{\partial\mathcal{B}_{\text{mic}}} \text{sym}(\mathbf{t}\otimes\mathbf{x})\, d\Gamma, \quad (6.1)$$

$$\overline{\mathbf{E}} \;=\; \frac{1}{V}\int_{\mathcal{B}_{\text{mic}}} \mathbf{E}\, d\Omega = -\frac{1}{V}\int_{\partial\mathcal{B}_{\text{mic}}} \varphi\,\mathbf{n}\, d\Gamma, \quad \text{and} \quad \overline{\mathbf{D}} = \frac{1}{V}\int_{\mathcal{B}_{\text{mic}}} \mathbf{D}\, d\Omega = -\frac{1}{V}\int_{\partial\mathcal{B}_{\text{mic}}} Q\,\mathbf{x}\, d\Gamma. \quad (6.2)$$

A comprehensive proof of the connection between the macro and the micro quantities is described in Schröder [91].

6.1 Admissible boundary conditions for the micro BVP of piezoelectric materials

For a consistent transition between the macro and micro quantities of piezoelectric materials, the Hill-Mandel condition is required to be satisfied. As piezoelectric materials are an electro-mechanically coupled material, there are two parts in the Hill-Mandel condition. The mechanical and the electrical parts of Hill-Mandel condition are

$$\overline{\boldsymbol{\sigma}}:\dot{\overline{\boldsymbol{\varepsilon}}} = \frac{1}{V}\int_{\mathcal{B}_{\text{mic}}} \boldsymbol{\sigma}:\dot{\boldsymbol{\varepsilon}}\, d\Omega \qquad \text{and} \qquad \overline{\mathbf{D}}\cdot\dot{\overline{\mathbf{E}}} = \frac{1}{V}\int_{\mathcal{B}_{\text{mic}}} \mathbf{D}\cdot\dot{\mathbf{E}}\, d\Omega, \qquad (6.3)$$

respectively. The Hill-Mandel condition for this coupled problem assumes that the power of the mechanical and electrical contributions on the macro level are equivalent to the volume average of the power of the mechanical and electrical contributions on the micro level, respectively. By introducing $\mathcal{P}_{\text{m}}$ and $\mathcal{P}_{\text{e}}$, the Hill-Mandel conditions (6.3) can be reformulated as

$$\mathcal{P}_{\text{m}} = \frac{1}{V}\int_{\mathcal{B}_{\text{mic}}} \boldsymbol{\sigma}:\dot{\boldsymbol{\varepsilon}}\, d\Omega - \overline{\boldsymbol{\sigma}}:\dot{\overline{\boldsymbol{\varepsilon}}} = 0 \qquad \text{and} \qquad \mathcal{P}_{\text{e}} = \frac{1}{V}\int_{\mathcal{B}_{\text{mic}}} \mathbf{D}\cdot\dot{\mathbf{E}}\, d\Omega - \overline{\mathbf{D}}\cdot\dot{\overline{\mathbf{E}}} = 0. \quad (6.4)$$

A detailed derivation of the boundary conditions on the micro domain for the mechanical problem by using $\mathcal{P}_{\text{m}}$ is given in Chapter 5. The three possible boundary conditions for

the mechanical balance equation of piezoelectric materials are the Dirichlet boundary condition

$$\dot{\mathbf{u}} = \overline{\dot{\nabla}\mathbf{u}}\,\mathbf{x} \quad \text{on} \quad \partial\mathcal{B}_{\text{mic}}, \tag{6.5}$$

the periodic boundary condition

$$\dot{\mathbf{u}} = \overline{\dot{\nabla}\mathbf{u}}\,\mathbf{x} + \dot{\tilde{\mathbf{w}}} \quad \text{on} \quad \partial\mathcal{B}_{\text{mic}}$$
$$\dot{\tilde{\mathbf{w}}}^+ = \dot{\tilde{\mathbf{w}}}^- \qquad \text{and} \qquad \mathbf{t}^+ = -\mathbf{t}^- \qquad \text{on opposite faces of } \partial\mathcal{B}_{\text{mic}}, \tag{6.6}$$

and Neumann boundary condition

$$\mathbf{t} = \overline{\boldsymbol{\sigma}}\mathbf{n} \quad \text{on} \quad \partial\mathcal{B}_{\text{mic}}. \tag{6.7}$$

Similarly, by using the electrical part of the Hill-Mandel condition, three boundary conditions for the electrical balance equation can be determined, i.e. the Dirichlet BC

$$\dot{\varphi} = -\overline{\dot{\mathbf{E}}}\cdot\mathbf{x} \quad \text{on} \quad \partial\mathcal{B}_{\text{mic}}, \tag{6.8}$$

the periodic BC

$$\dot{\varphi} = -\overline{\dot{\mathbf{E}}}\cdot\mathbf{x} + \dot{\tilde{\omega}} \quad \text{on} \quad \partial\mathcal{B}_{\text{mic}}$$
$$\dot{\tilde{\omega}}^+ = \dot{\tilde{\omega}}^-$$
$$Q^+ = -Q^-, \tag{6.9}$$

and Neumann BC

$$Q = -\overline{\mathbf{D}}\cdot\mathbf{n} \quad \text{on} \quad \partial\mathcal{B}_{\text{mic}}. \tag{6.10}$$

An explicit derivation of the boundary conditions for the electrical part can be found in Schröder [91].

6.2   Homogenized material response

Here the formulations of the homogenized material parameters of piezoelectric materials are described in detail by using the three sets of boundary conditions for the micro BVP. In this section the underlined symbols denote the matrix notation with Voigt style. Here the formulations by Miehe and Koch [65] for mechanical properties in small deformation case is extended in order to homogenize the material moduli of piezoelectric materials.

The constitutive relations of piezoelectric materials in (4.8) and (4.9) can be expressed in a combined Voigt-notation as

$$\begin{bmatrix} \boldsymbol{\sigma} \\ \mathbf{D} \end{bmatrix} = \begin{bmatrix} \mathbb{C} & \mathbb{b}^T \\ \mathbb{b} & -\mathbf{A} \end{bmatrix} \begin{bmatrix} \boldsymbol{\varepsilon} \\ -\mathbf{E} \end{bmatrix} + \begin{bmatrix} -\mathbb{C}\,\boldsymbol{\varepsilon}^0 \\ \mathbf{P}^0 - \mathbb{b}\,\boldsymbol{\varepsilon}^0 \end{bmatrix}, \tag{6.11}$$

alternatively,

$$\underline{\mathbf{S}} = \underline{\mathbb{L}}\,\underline{\mathbf{e}} + \underline{\mathbf{S}}^0, \tag{6.12}$$

where

$$\underline{\mathbf{S}} = \begin{bmatrix} \boldsymbol{\sigma} \\ \mathbf{D} \end{bmatrix}, \quad \underline{\mathbb{L}} = \begin{bmatrix} \mathbb{C} & \mathbb{b}^T \\ \mathbb{b} & -\mathbf{A} \end{bmatrix}, \quad \underline{\mathbf{e}} = \begin{bmatrix} \boldsymbol{\varepsilon} \\ -\mathbf{E} \end{bmatrix} \quad \text{and} \quad \underline{\mathbf{S}}^0 = \begin{bmatrix} -\mathbb{C}\,\boldsymbol{\varepsilon}^0 \\ \mathbf{P}^0 - \mathbb{b}\,\boldsymbol{\varepsilon}^0 \end{bmatrix}.$$

6.2.1 Dirichlet boundary condition on the micro domain

The prescribed boundary displacements and potentials on the micro domains are

$$\mathbf{u}_q \;=\; \overline{\nabla\mathbf{u}}\,\mathbf{x}_q = \overline{\boldsymbol{\varepsilon}}\,\mathbf{x}_q + \overline{\boldsymbol{\varpi}}\,\mathbf{x}_q \quad \text{and} \tag{6.13}$$

$$\varphi_q \;=\; -\overline{\mathbf{E}}{\cdot}\mathbf{x}_q, \tag{6.14}$$

respectively, where $q = 1, \ldots, M$ (M is the total number of boundary nodes). In equation (6.13) $\overline{\boldsymbol{\varepsilon}}$ and $\overline{\boldsymbol{\varpi}}$ are the symmetric and the anti-symmetric part of the macro displacement gradient tensor $\overline{\nabla\mathbf{u}}$, respectively. Introducing the Voigt-notation for the macro strain tensor in 2D problems $\overline{\underline{\boldsymbol{\varepsilon}}} = [\overline{\varepsilon}_{11}, \ \overline{\varepsilon}_{22}, \ 2\overline{\varepsilon}_{12}]^T$, the alternative representation of $\underline{\mathbf{u}}_q$ and φ_q are

$$\underline{\mathbf{u}}_q \;=\; \underline{\mathbb{Q}}_{q\mathrm{m}}^T\,\overline{\underline{\boldsymbol{\varepsilon}}} \;+\; \mathbb{A}_{q\mathrm{m}}^T\,\overline{\boldsymbol{\varpi}} \tag{6.15}$$

$$\varphi_q \;=\; -\underline{\mathbb{Q}}_{q\mathrm{e}}^T\,\overline{\mathbf{E}}, \tag{6.16}$$

where the subscripts m and e denote the mechanical and the electrical part, respectively. And $\underline{\mathbb{Q}}_{q\mathrm{m}}$, $\mathbb{A}_{q\mathrm{m}}$ and $\underline{\mathbb{Q}}_{q\mathrm{e}}$ are defined in the following way:

$$\underline{\mathbb{Q}}_{q\mathrm{m}} = \frac{1}{2}\begin{bmatrix} 2x_1 & 0 \\ 0 & 2x_2 \\ x_2 & x_1 \end{bmatrix}_q, \quad \underline{\mathbb{Q}}_{q\mathrm{e}} = \begin{bmatrix} x_1 \\ x_2 \end{bmatrix}_q \quad \text{and} \quad \mathbb{A}_{q\mathrm{m}} = [-x_2 \ \ x_1]_q. \tag{6.17}$$

As there is no contribution from the infinitesimal rotational part $\overline{\omega}$ of the displacement gradient (the second term in (6.13)) to the stress field, this term is omitted in the following derivations. In a combined way the generalized displacement vector is

$$\underline{\mathbf{u}}_{qc} = \underline{\mathbb{Q}}_{qc}^{T} \overline{\mathbf{e}}, \tag{6.18}$$

where the subscript c denotes the combined formulations (mechanical and electrical), and

$$
\begin{aligned}
\underline{\mathbf{u}}_{qc} &= \left[u_{1q}, u_{2q}, \varphi_q \right]^{T}, \\
\overline{\mathbf{e}} &= \left[\overline{\varepsilon}_{11}, \overline{\varepsilon}_{22}, 2\overline{\varepsilon}_{12}, -\overline{E}_1, -\overline{E}_2 \right]^{T} \quad \text{and} \\
\underline{\mathbb{Q}}_{qc} &= \begin{bmatrix} \underline{\mathbb{Q}}_{qm} & \mathbf{0} \\ \mathbf{0} & \underline{\mathbb{Q}}_{qe} \end{bmatrix}
\end{aligned}
\tag{6.19}
$$

is used.

The boundary displacements and the electric potentials in global form is written as

$$\underline{\mathbf{u}}_{b} = \underline{\mathbb{Q}}_{c}^{T} \overline{\mathbf{e}}, \tag{6.20}$$

where $\underline{\mathbf{u}}_{b}$ contains all boundary degrees of freedom (the boundary mechanical displacements and electrical potentials) and

$$\underline{\mathbb{Q}}_{c} = \left[\underline{\mathbb{Q}}_{1c}, \underline{\mathbb{Q}}_{2c}, \cdots, \underline{\mathbb{Q}}_{Mc} \right]. \tag{6.21}$$

Assume $\underline{\mathbf{K}}\,\underline{\mathbf{u}} = \underline{\mathbf{F}}$ is the linear system of equations on the micro level after performing the assembling in the finite element analysis. The generalized stiffness matrix $\underline{\mathbf{K}}$, the generalized displacement vector $\underline{\mathbf{u}}$, and the right hand side $\underline{\mathbf{F}}$ are partitioned as

$$
\begin{bmatrix} \underline{\mathbf{K}}_{ii} & \underline{\mathbf{K}}_{ib} \\ \underline{\mathbf{K}}_{bi} & \underline{\mathbf{K}}_{bb} \end{bmatrix}
\begin{bmatrix} \underline{\mathbf{u}}_{i} \\ \underline{\mathbf{u}}_{b} \end{bmatrix}
=
\begin{bmatrix} \underline{\mathbf{F}}_{i} \\ \underline{\mathbf{F}}_{b} \end{bmatrix},
\tag{6.22}
$$

where subscripts i and b denote the internal and the boundary degrees of freedom, respectively. The linear displacements and potentials on the boundary can be represented in the compact global combined form

$$\mathbf{d}(\underline{\mathbf{u}}_{b}; \overline{\mathbf{e}}) = \underline{\mathbf{u}}_{b} - \underline{\mathbb{Q}}_{c}^{T} \overline{\mathbf{e}} = \mathbf{0}. \tag{6.23}$$

Using the Lagrange multiplier method to incorporate the boundary constraints in the total energy of the discrete system, one obtains

$$\pi = \frac{1}{2}\underline{\mathbf{u}}^T\underline{\mathbf{K}}\underline{\mathbf{u}} - \underline{\mathbf{u}}^T\underline{\mathbf{F}} - \underline{\boldsymbol{\delta}}^T(\underline{\mathbf{u}}_{\mathrm{b}} - \underline{\mathbb{Q}}_{\mathrm{c}}^T\overline{\mathbf{e}}), \qquad (6.24)$$

where $\underline{\boldsymbol{\delta}}$ are the Lagrange multipliers. In order to obtain the equilibrium solution of the system, the following conditions must be satisfied

$$\frac{\partial \pi}{\partial \underline{\mathbf{u}}} = \mathbf{0} \quad \text{and} \quad \frac{\partial \pi}{\partial \underline{\boldsymbol{\delta}}} = \mathbf{0}. \qquad (6.25)$$

Determining the partial derivatives in (6.25), it is possible to deduce the following equations

$$\begin{aligned}
\underline{\mathbf{K}}_{\mathrm{ii}}\underline{\mathbf{u}}_{\mathrm{i}} + \underline{\mathbf{K}}_{\mathrm{ib}}\underline{\mathbf{u}}_{\mathrm{b}} - \underline{\mathbf{F}}_{\mathrm{i}} &= \mathbf{0}, \\
\underline{\mathbf{K}}_{\mathrm{bi}}\underline{\mathbf{u}}_{\mathrm{i}} + \underline{\mathbf{K}}_{\mathrm{bb}}\underline{\mathbf{u}}_{\mathrm{b}} - \underline{\mathbf{F}}_{\mathrm{b}} - \underline{\boldsymbol{\delta}} &= \mathbf{0}, \\
\text{and} \qquad \underline{\mathbf{u}}_{\mathrm{b}} - \underline{\mathbb{Q}}_{\mathrm{c}}^T\overline{\mathbf{e}} &= \mathbf{0}.
\end{aligned} \qquad (6.26)$$

For discrete setting the limit $\mathbf{t}\mathrm{d}\Gamma \longrightarrow \boldsymbol{\delta}_{q\mathrm{m}}$ of the infinitesimal forces $\mathbf{t}\mathrm{d}\Gamma$ in (6.1) is considered to be the finite forces $\boldsymbol{\delta}_{q\mathrm{m}}$ and the limit $Q\mathrm{d}\Gamma \longrightarrow \delta_{q\mathrm{e}}$ of the infinitesimal charges $Q\mathrm{d}\Gamma$ in (6.2) is to be the finite charges $\delta_{q\mathrm{e}}$ acting on the node q. Then (6.1) and (6.2) degenerate to the discrete sums

$$\overline{\boldsymbol{\sigma}} = \frac{1}{V}\sum_{q=1}^{M}\mathrm{sym}\left[\boldsymbol{\delta}_{q\mathrm{m}} \otimes \mathbf{x}_q\right], \qquad (6.27)$$

and

$$\overline{\mathbf{D}} = -\frac{1}{V}\sum_{q=1}^{M}\delta_{q\mathrm{e}}\mathbf{x}_q. \qquad (6.28)$$

Equations (6.27) and (6.28) can be written in a combined way as in the following,

$$\overline{\mathbf{S}} = \frac{1}{V}\sum_{q=1}^{M}\underline{\mathbb{Q}}_{q\mathrm{c}}\underline{\boldsymbol{\delta}}_q. \qquad (6.29)$$

The average or homogenized stress tensor and electric displacement in a combined way with the help of the Voigt-notation is expressed in the following way

$$\overline{\mathbf{S}} = \frac{1}{V}\underline{\mathbb{Q}}_c\underline{\boldsymbol{\delta}}, \tag{6.30}$$

where $\overline{\mathbf{S}} = \left[\overline{\sigma}_{11}, \overline{\sigma}_{22}, \overline{\sigma}_{12}, \overline{D}_1, \overline{D}_2\right]^T$. Eliminating $\underline{\boldsymbol{\delta}}$ from the second equation in (6.26) and from (6.30); and using the first equation in (6.26), one obtains

$$\begin{aligned}
\overline{\mathbf{S}} &= \frac{1}{V}\underline{\mathbb{Q}}_c\left(\underline{\mathbf{K}}_{bi}\underline{\mathbf{u}}_i + \underline{\mathbf{K}}_{bb}\underline{\mathbf{u}}_b - \underline{\mathbf{F}}_b\right) \\
&= \frac{1}{V}\underline{\mathbb{Q}}_c\left(\underline{\mathbf{K}}_{bi}\underline{\mathbf{K}}_{ii}^{-1}(\underline{\mathbf{F}}_i - \underline{\mathbf{K}}_{ib}\underline{\mathbf{u}}_b) + \underline{\mathbf{K}}_{bb}\underline{\mathbf{u}}_b - \underline{\mathbf{F}}_b\right) \\
&= \frac{1}{V}\underline{\mathbb{Q}}_c\left((\underline{\mathbf{K}}_{bb} - \underline{\mathbf{K}}_{bi}\underline{\mathbf{K}}_{ii}^{-1}\underline{\mathbf{K}}_{ib})\underline{\mathbf{u}}_b + \underline{\mathbf{K}}_{bi}\underline{\mathbf{K}}_{ii}^{-1}\underline{\mathbf{F}}_i - \underline{\mathbf{F}}_b\right) \\
&= \frac{1}{V}\underline{\mathbb{Q}}_c\left((\underline{\mathbf{K}}_{bb} - \underline{\mathbf{K}}_{bi}\underline{\mathbf{K}}_{ii}^{-1}\underline{\mathbf{K}}_{ib})\underline{\mathbb{Q}}_c^T\overline{\mathbf{e}} + \underline{\mathbf{K}}_{bi}\underline{\mathbf{K}}_{ii}^{-1}\underline{\mathbf{F}}_i - \underline{\mathbf{F}}_b\right) \\
&= \frac{1}{V}\underline{\mathbb{Q}}_c\widetilde{\underline{\mathbf{K}}}_{bb}\underline{\mathbb{Q}}_c^T\overline{\mathbf{e}} + \frac{1}{V}\underline{\mathbb{Q}}_c\widetilde{\underline{\mathbf{F}}}_b.
\end{aligned} \tag{6.31}$$

A comparison of the equations (6.12) and (6.31) yields

$$\mathbb{L} = \frac{1}{V}\underline{\mathbb{Q}}_c\widetilde{\underline{\mathbf{K}}}_{bb}\underline{\mathbb{Q}}_c^T \qquad \text{and} \qquad \underline{\mathbf{S}}^0 = \frac{1}{V}\underline{\mathbb{Q}}_c\widetilde{\underline{\mathbf{F}}}_b, \tag{6.32}$$

where

$$\widetilde{\underline{\mathbf{K}}}_{bb} = \underline{\mathbf{K}}_{bb} - \underline{\mathbf{K}}_{bi}\underline{\mathbf{K}}_{ii}^{-1}\underline{\mathbf{K}}_{ib} \quad \text{and} \quad \widetilde{\underline{\mathbf{F}}}_b = \underline{\mathbf{K}}_{bi}\underline{\mathbf{K}}_{ii}^{-1}\underline{\mathbf{F}}_i - \underline{\mathbf{F}}_b. \tag{6.33}$$

From equation (6.32) the homogenized material parameters (elastic modulus $\underline{\mathbb{C}}$, dielectric modulus $\underline{\mathbf{A}}$, piezoelectric modulus $\underline{\mathbb{b}}$, remanent strain $\underline{\boldsymbol{\varepsilon}}^0$ and remanent polarization $\underline{\mathbf{P}}^0$) can easily be determined, see (6.11) and (6.12).

6.2.2 Neumann boundary condition on the micro domain

Constant traction and constant surface charge density are defined on the boundary of the RVE as

$$\mathbf{t} = \overline{\boldsymbol{\sigma}}\mathbf{n} \quad \text{and} \quad Q = -\overline{\mathbf{D}} \cdot \mathbf{n} \qquad \text{on} \quad \partial\mathcal{B}_{\text{mic}}, \tag{6.34}$$

respectively. These conditions satisfy the averaging theorem in a priori. However, equation (6.34) is not consistent with the deformation and electric field driven approach for

the homogenization technique. In order to obtain conditions equivalent to (6.34) in terms of a prescribed macroscopic strain $\overline{\varepsilon}$ and macroscopic electric field $\overline{\mathbf{E}}$ based on (6.1) and (6.2), the weak constraints

$$\frac{1}{V}\int_{\partial\mathcal{B}_{\text{mic}}}\text{sym}(\mathbf{u}\otimes\mathbf{n})\,\mathrm{d}\Gamma=\overline{\varepsilon}\quad\text{and}\quad-\frac{1}{V}\int_{\partial\mathcal{B}_{\text{mic}}}\varphi\,\mathbf{n}\,\mathrm{d}\Gamma=\overline{\mathbf{E}}\tag{6.35}$$

are considered on the boundary of the RVE. Scalar contraction of the first equation of (6.35) with $\overline{\sigma}$ from left hand side and scalar product of the second equation of (6.35) with $\overline{\mathbf{D}}$ give the expressions

$$\frac{1}{V}\int_{\partial\mathcal{B}_{\text{mic}}}\mathbf{u}\cdot\overline{\sigma}\mathbf{n}\,\mathrm{d}\Gamma-\overline{\sigma}:\overline{\varepsilon}=0\quad\text{and}\tag{6.36}$$

$$\frac{1}{V}\int_{\partial\mathcal{B}_{\text{mic}}}\varphi\left(-\overline{\mathbf{D}}\cdot\mathbf{n}\right)\mathrm{d}\Gamma-\overline{\mathbf{D}}\cdot\overline{\mathbf{E}}=0,\tag{6.37}$$

which are the equivalent formulations of the Hill-Mandel theorem. Equations (6.36) and (6.37) are considered as the Lagrange terms which, when added to some functional, enforce the constraints in (6.35) by means of the Lagrangian multipliers $\overline{\sigma}$ and $\overline{\mathbf{D}}$. The first terms in (6.36) and (6.37) are standard potentials of the tractions $\mathbf{t}=\overline{\sigma}\mathbf{n}$ and of the surface charge $Q=-\overline{\mathbf{D}}\cdot\mathbf{n}$ on the boundary $\partial\mathcal{B}_{\text{mic}}$, respectively. Thus, the weak constraints in (6.35) enforce, when treated with the Lagrange multiplier method, traction type and electric density type boundary conditions in (6.34) for prescribed stress field $\overline{\sigma}$ and electric density field $\overline{\mathbf{D}}$. It is obvious that the Lagrange multipliers $\overline{\sigma}$ and $\overline{\mathbf{D}}$ are then identified as the homogenized macro stress and the homogenized macro electric density vector, respectively. This observation enables us to compute the traction and surface charge density on the boundary for a $\overline{\varepsilon}$ and $\overline{\mathbf{E}}$ controlled process where the multipliers $\overline{\sigma}$ and $\overline{\mathbf{D}}$ appear as variables.

Discretization of the surface integrals in (6.35) is required for numerical implementation. Now, the limit $\mathbf{n}\mathrm{d}A\to\mathbf{a}_q$ of the continuous area vector is considered as a discrete area vector at the node q. In two-dimensional problems $n_{\text{dim}}=2$, the nodal area vector can be written as

$$\mathbf{a}_q=\frac{1}{2}\left[\mathbf{x}_{q+1}-\mathbf{x}_{q-1}\right]\times\mathbf{e}_3,\tag{6.38}$$

by the nodal coordinates $\mathbf{x}_{q-1}$ and $\mathbf{x}_{q+1}$ of nodes $q-1$ and $q+1$ which are the neighbors of node q. Here the neighbor nodes $q-1$, q and $q+1$ are to be oriented in such a way, so that the vector product of (6.38) with the Cartesian base vector $\mathbf{e}_3$ gives $\mathbf{a}_q$ as normal

vector pointing outward at node q. By considering the definition of the nodal area vector
(6.38), the integrals in (6.35) can be approximated as

$$\frac{1}{V} \sum_{q=1}^{M} \text{sym} \left[\mathbf{u}_q \otimes \mathbf{a}_q \right] = \overline{\boldsymbol{\varepsilon}}, \tag{6.39}$$

and

$$-\frac{1}{V} \sum_{q=1}^{M} \varphi_q \mathbf{a}_q = \overline{\mathbf{E}}. \tag{6.40}$$

This may be written by the matrix representation

$$\sum_{q=1}^{M} \underline{\mathbb{S}}_{q\text{m}} \underline{\mathbf{u}}_q = \underline{\overline{\boldsymbol{\varepsilon}}}, \tag{6.41}$$

and

$$\sum_{q=1}^{M} \underline{\mathbb{S}}_{q\text{e}} \varphi_q = -\underline{\overline{\mathbf{E}}}. \tag{6.42}$$

where $\underline{\mathbb{S}}_{q\text{m}} \in \mathbb{R}^3 \times \mathbb{R}^2$ and $\underline{\mathbb{S}}_{q\text{e}} \in \mathbb{R}^2$ are the matrices which depend on the area vector $\mathbf{a}_q$
at nodal point q. The representations, in analogy to the first two equations in (6.17), may
be expressed as the forms

$$\underline{\mathbb{S}}_{q\text{m}} = \frac{1}{2V} \begin{bmatrix} 2a_1 & 0 \\ 0 & 2a_2 \\ a_2 & a_1 \end{bmatrix}, \tag{6.43}$$

and

$$\underline{\mathbb{S}}_{q\text{e}} = \frac{1}{V} \begin{bmatrix} a_1 \\ a_2 \end{bmatrix} \tag{6.44}$$

for $n_{\text{dim}} = 2$, respectively.

The combined coordinate matrix can be expressed as in the following form

$$\underline{\mathbb{S}}_{q\text{c}} = \begin{bmatrix} \underline{\mathbb{S}}_{q\text{m}} & \mathbf{0} \\ \mathbf{0} & \underline{\mathbb{S}}_{q\text{e}} \end{bmatrix}, \tag{6.45}$$

and the combined constraint can be stated as

$$\sum_{q=1}^{M} \underline{\mathbb{S}}_{q\text{c}} \underline{\mathbf{u}}_{q\text{c}} = \underline{\overline{\mathbf{e}}}. \tag{6.46}$$

Similar as (6.21) a global combined coordinate matrix $\underline{\mathbb{S}}_c \in \mathbb{R}^5 \times \mathbb{R}^{3 \cdot M}$ associated with all M nodal points on the boundary of the RVE is defined by

$$\underline{\mathbb{S}}_c = [\underline{\mathbb{S}}_{1c} \quad \underline{\mathbb{S}}_{2c} \quad \cdots \quad \underline{\mathbb{S}}_{Mc}].$$ (6.47)

Afterwards the combined weak constraints in (6.35) is written by the compact global form

$$\mathbf{s}(\underline{\mathbf{u}}_b; \overline{\mathbf{e}}) = \underline{\mathbb{S}}_c \underline{\mathbf{u}}_b - \overline{\mathbf{e}} = \mathbf{0}.$$ (6.48)

The Lagrange multiplier method can be used to incorporate these constraints in the computation of the equilibrium state of the microstructure. By applying the Lagrange multiplier, the set of linear equations

$$\begin{aligned}
\underline{\mathbf{K}}_{ii}\underline{\mathbf{u}}_i + \underline{\mathbf{K}}_{ib}\underline{\mathbf{u}}_b - \underline{\mathbf{F}}_i &= \mathbf{0}, \\
\underline{\mathbf{K}}_{bi}\underline{\mathbf{u}}_i + \underline{\mathbf{K}}_{bb}\underline{\mathbf{u}}_b - \underline{\mathbf{F}}_b - \underline{\mathbb{S}}_c^T \boldsymbol{\lambda} &= \mathbf{0}, \\
\text{and} \quad \underline{\mathbb{S}}_c \underline{\mathbf{u}}_b - \overline{\mathbf{e}} &= \mathbf{0}
\end{aligned}$$ (6.49)

is derived. Eliminating $\underline{\mathbf{u}}_i$ from first two equations of (6.49),

$$\underline{\mathbf{u}}_i = \underline{\mathbf{K}}_{ii}^{-1}\left(\underline{\mathbf{F}}_i - \underline{\mathbf{K}}_{ib}\underline{\mathbf{u}}_b\right),$$ (6.50)

$$\underline{\mathbf{K}}_{bi}\underline{\mathbf{K}}_{ii}^{-1}\left(\underline{\mathbf{F}}_i - \underline{\mathbf{K}}_{ib}\underline{\mathbf{u}}_b\right) + \underline{\mathbf{K}}_{bb}\underline{\mathbf{u}}_b - \underline{\mathbf{F}}_b - \underline{\mathbb{S}}_c^T\boldsymbol{\lambda} = \mathbf{0},$$ (6.51)

$$\left(\underline{\mathbf{K}}_{bi}\underline{\mathbf{K}}_{ii}^{-1}\underline{\mathbf{K}}_{ib} + \underline{\mathbf{K}}_{bb}\right)\underline{\mathbf{u}}_b + \underline{\mathbf{K}}_{bi}\underline{\mathbf{K}}_{ii}^{-1}\underline{\mathbf{F}}_i - \underline{\mathbf{F}}_b - \underline{\mathbb{S}}_c^T\boldsymbol{\lambda} = \mathbf{0},$$ (6.52)

the following equation is obtained

$$\underline{\mathbf{u}}_b = \widetilde{\underline{\mathbf{K}}}_{bb}^{-1}\left(\underline{\mathbb{S}}_c^T\boldsymbol{\lambda} - \widetilde{\underline{\mathbf{F}}}_b\right),$$ (6.53)

where

$$\widetilde{\underline{\mathbf{K}}}_{bb} = \underline{\mathbf{K}}_{bb} - \underline{\mathbf{K}}_{bi}\underline{\mathbf{K}}_{ii}^{-1}\underline{\mathbf{K}}_{ib} \quad \text{and} \quad \widetilde{\underline{\mathbf{F}}}_b = \underline{\mathbf{K}}_{bi}\underline{\mathbf{K}}_{ii}^{-1}\underline{\mathbf{F}}_i - \underline{\mathbf{F}}_b.$$ (6.54)

Inserting $\underline{\mathbf{u}}_b$ of equation (6.53) into the last equation of (6.49), the following relation can be inferred

$$\underline{\mathbb{S}}_c\widetilde{\underline{\mathbf{K}}}_{bb}^{-1}\left(\underline{\mathbb{S}}_c^T\boldsymbol{\lambda} - \widetilde{\underline{\mathbf{F}}}_b\right) - \overline{\mathbf{e}} = \mathbf{0}.$$ (6.55)

After rearranging equation (6.55), the following equation is obtained

$$\boldsymbol{\lambda} = \left[\mathbb{S}_{\mathrm{c}} \widetilde{\mathbf{K}}_{\mathrm{bb}}^{-1} \mathbb{S}_{\mathrm{c}}^{T} \right]^{-1} \overline{\mathbf{e}} + \mathbb{S}_{\mathrm{c}} \widetilde{\mathbf{K}}_{\mathrm{bb}}^{-1} \widetilde{\mathbf{F}}_{\mathrm{b}}. \tag{6.56}$$

Here it is possible to identify the macro stresses and macro electric displacements as the Lagrangian multiplier

$$\overline{\mathbf{S}} = \boldsymbol{\lambda}. \tag{6.57}$$

Equation (6.56) can be written as

$$\overline{\mathbf{S}} = \left[\mathbb{S}_{\mathrm{c}} \widetilde{\mathbf{K}}_{\mathrm{bb}}^{-1} \mathbb{S}_{\mathrm{c}}^{T} \right]^{-1} \overline{\mathbf{e}} + \mathbb{S}_{\mathrm{c}} \widetilde{\mathbf{K}}_{\mathrm{bb}}^{-1} \widetilde{\mathbf{F}}_{\mathrm{b}}. \tag{6.58}$$

A comparison between the equations (6.12) and (6.58) leads to

$$\mathbb{L} = \left[\mathbb{S}_{\mathrm{c}} \widetilde{\mathbf{K}}_{\mathrm{bb}}^{-1} \mathbb{S}_{\mathrm{c}}^{T} \right]^{-1} \qquad \text{and} \qquad \underline{\mathbf{S}}^{0} = \mathbb{S}_{\mathrm{c}} \widetilde{\mathbf{K}}_{\mathrm{bb}}^{-1} \widetilde{\mathbf{F}}_{\mathrm{b}}. \tag{6.59}$$

From equation (6.59) the homogenized material parameters can be determined similarly as described for a displacement type boundary conditions based homogenization in Section 6.2.1.

6.2.3   Periodic boundary condition on the micro domain

For the numerical implementation of the periodic type boundary conditions, a discretization of constraints on "pairs" of node positions $\mathbf{x}_q^+$ and $\mathbf{x}_q^-$ from opposite parts $\partial \mathcal{B}_{\mathrm{mic}}^+$ and $\partial \mathcal{B}_{\mathrm{mic}}^-$ of the boundary of the microstructure is required. A mesh of P corresponding nodes on the boundary are to be generated. For a square-shaped micro domain, this gives $P = M/2 + 2$ pairs of nodes on the boundary. For all node pairs $q = 1, \ldots, P$, the periodicity conditions

$$[\![\mathbf{u}_q]\!]_{\mathrm{b}} = \overline{\nabla \mathbf{u}} [\![\mathbf{x}_q]\!]_{\mathrm{b}} = \overline{\boldsymbol{\varepsilon}} [\![\mathbf{x}_q]\!]_{\mathrm{b}} + \overline{\boldsymbol{\omega}} [\![\mathbf{x}_q]\!]_{\mathrm{b}}, \tag{6.60}$$

and

$$[\![\varphi_q]\!]_{\mathrm{b}} = -\overline{\mathbf{E}} \cdot [\![\mathbf{x}_q]\!]_{\mathrm{b}} \tag{6.61}$$

are assumed with the jump notation on the boundary $[\![\mathbf{x}_q]\!]_{\mathrm{b}} = \mathbf{x}_q^+ - \mathbf{x}_q^-$. By using matrix notations (6.17) and (6.19), these constraints may be reformulated as

$$\mathbf{\underline{u}}_q^+ - \mathbf{\underline{u}}_q^- = \left(\underline{\mathbb{Q}}_{qm}^{+T} - \underline{\mathbb{Q}}_{qm}^{-T} \right) \overline{\boldsymbol{\varepsilon}} + \left(\mathbb{A}_{qm}^{+T} - \mathbb{A}_{qm}^{-T} \right) \overline{\boldsymbol{\omega}}, \quad q = 1, \ldots, P, \tag{6.62}$$

and

$$\varphi_q^+ - \varphi_q^- = - \left(\underline{\mathbb{Q}}_{qe}^{+T} - \underline{\mathbb{Q}}_{qe}^{-T} \right) \overline{\mathbf{E}}, \quad q = 1, \ldots, P, \tag{6.63}$$

or, in the compact representations

$$\mathbb{P}_{qm}\mathbf{u}_{\mathrm{bm}} = \mathbb{Z}_{qm}^{T}\overline{\boldsymbol{\varepsilon}}, \quad q = 1, \ldots, P \tag{6.64}$$

and

$$\mathbb{P}_{qe}\varphi_{\mathrm{b}} = \mathbb{Z}_{qe}^{T}\overline{\mathbf{E}}, \quad q = 1, \ldots, P. \tag{6.65}$$

The term with $\overline{\boldsymbol{\omega}}$ in (6.62) is omitted in equation (6.64) for the same reason as discussed in Section 6.2.1. The combined form of the compact representations for mechanical and electrical quantities can be written as

$$\mathbb{P}_{qc}\mathbf{u}_{\mathrm{bc}} = \mathbb{Z}_{qc}^{T}\overline{\mathbf{e}}, \quad q = 1, \ldots, P. \tag{6.66}$$

The matrix $\mathbb{P}_{qc}$ is denoted as a link-topology matrix regarding the node pair q. The elements of this matrix are from $\{0, 1, -1\}$ only. All P constraints are assembled in the following global matrix notation,

$$\mathbf{p}(\mathbf{\underline{u}}_{\mathrm{b}}; \overline{\mathbf{e}}) = \mathbb{P}_{\mathrm{c}}\mathbf{\underline{u}}_{\mathrm{b}} - \mathbb{Z}_{\mathrm{c}}^{T}\overline{\mathbf{e}} \tag{6.67}$$

with the combined coordinate matrix $\mathbb{Z}_{\mathrm{c}} = \underline{\mathbb{Q}}_{\mathrm{c}}^{+} - \underline{\mathbb{Q}}_{\mathrm{c}}^{-} \in \mathbb{R}^{5} \times \mathbb{R}^{P \cdot (n_{\mathrm{dim}}+1)}$ for the case $n_{\mathrm{dim}} = 2$, which is built in the same way as in (6.21).

By applying the Lagrange multiplier method to incorporate these constraints into the computation of the equilibrium state microstructure, the set of linear equations

$$\begin{aligned} \mathbf{\underline{K}}_{\mathrm{ii}}\mathbf{\underline{u}}_{\mathrm{i}} + \mathbf{\underline{K}}_{\mathrm{ib}}\mathbf{\underline{u}}_{\mathrm{b}} - \mathbf{\underline{F}}_{\mathrm{i}} &= \mathbf{0}, \\ \mathbf{\underline{K}}_{\mathrm{bi}}\mathbf{\underline{u}}_{\mathrm{i}} + \mathbf{\underline{K}}_{\mathrm{bb}}\mathbf{\underline{u}}_{\mathrm{b}} - \mathbf{\underline{F}}_{\mathrm{b}} - \mathbb{P}_{\mathrm{c}}^{T}\boldsymbol{\pi} &= \mathbf{0}, \\ \text{and} \quad \mathbb{P}_{\mathrm{c}}\mathbf{\underline{u}}_{\mathrm{b}} - \mathbb{Z}_{\mathrm{c}}^{T}\overline{\mathbf{e}} &= \mathbf{0} \end{aligned} \tag{6.68}$$

is derived. The Lagrangian multiplier $\underline{\boldsymbol{\pi}} \in \mathbb{R}^{M \cdot (n_{\dim}+1)}$ represents the mechanical forces and electric charges acting on the node pairs of the boundary and enforces the constraint (6.67). The set of equations in (6.68) describes the state of the microstructure except rigid body motions; these are excluded by putting some additional constraints

$$\underline{\mathbf{u}}_{\mathrm{i}} = \underline{\mathbf{K}}_{\mathrm{ii}}^{-1} \left(\underline{\mathbf{F}}_{\mathrm{i}} - \underline{\mathbf{K}}_{\mathrm{ib}} \underline{\mathbf{u}}_{\mathrm{b}} \right) \tag{6.69}$$

$$\underline{\mathbf{K}}_{\mathrm{bi}} \underline{\mathbf{K}}_{\mathrm{ii}}^{-1} \left(\underline{\mathbf{F}}_{\mathrm{i}} - \underline{\mathbf{K}}_{\mathrm{ib}} \underline{\mathbf{u}}_{\mathrm{b}} \right) + \underline{\mathbf{K}}_{\mathrm{bb}} \underline{\mathbf{u}}_{\mathrm{b}} - \underline{\mathbf{F}}_{\mathrm{b}} - \mathbb{P}_{\mathrm{c}}^{T} \underline{\boldsymbol{\pi}} = \mathbf{0} \tag{6.70}$$

$$\left(\underline{\mathbf{K}}_{\mathrm{bi}} \underline{\mathbf{K}}_{\mathrm{ii}}^{-1} \underline{\mathbf{K}}_{\mathrm{ib}} + \underline{\mathbf{K}}_{\mathrm{bb}} \right) \underline{\mathbf{u}}_{\mathrm{b}} + \underline{\mathbf{K}}_{\mathrm{bi}} \underline{\mathbf{K}}_{\mathrm{ii}}^{-1} \underline{\mathbf{F}}_{\mathrm{i}} - \underline{\mathbf{F}}_{\mathrm{b}} - \mathbb{P}_{\mathrm{c}}^{T} \underline{\boldsymbol{\pi}} = \mathbf{0} \tag{6.71}$$

$$\underline{\mathbf{u}}_{\mathrm{b}} = \widetilde{\underline{\mathbf{K}}}_{\mathrm{bb}}^{-1} \left(\mathbb{P}_{\mathrm{c}}^{T} \underline{\boldsymbol{\pi}} - \widetilde{\underline{\mathbf{F}}}_{\mathrm{b}} \right) , \tag{6.72}$$

where

$$\widetilde{\underline{\mathbf{K}}}_{\mathrm{bb}} = \underline{\mathbf{K}}_{\mathrm{bb}} - \underline{\mathbf{K}}_{\mathrm{bi}} \underline{\mathbf{K}}_{\mathrm{ii}}^{-1} \underline{\mathbf{K}}_{\mathrm{ib}} \quad \text{and} \quad \widetilde{\underline{\mathbf{F}}}_{\mathrm{b}} = \underline{\mathbf{K}}_{\mathrm{bi}} \underline{\mathbf{K}}_{\mathrm{ii}}^{-1} \underline{\mathbf{F}}_{\mathrm{i}} - \underline{\mathbf{F}}_{\mathrm{b}}. \tag{6.73}$$

Inserting $\underline{\mathbf{u}}_{\mathrm{b}}$ from (6.72) in (6.68$_3$) gives

$$\underline{\boldsymbol{\pi}} = \left[\mathbb{P}_{\mathrm{c}} \widetilde{\underline{\mathbf{K}}}_{\mathrm{bb}}^{-1} \mathbb{P}_{\mathrm{c}}^{T} \right]^{-1} \mathbb{Z}_{\mathrm{c}}^{T} \overline{\mathbf{e}} + \mathbb{P}_{\mathrm{c}} \widetilde{\underline{\mathbf{K}}}_{\mathrm{bb}}^{-1} \widetilde{\underline{\mathbf{F}}}_{\mathrm{b}}. \tag{6.74}$$

For the discrete setting, the limit $\mathbf{t} \mathrm{d} \Gamma \longrightarrow \boldsymbol{\pi}_{q\mathrm{m}}$ of the infinitesimal forces $\mathbf{t} \mathrm{d} \Gamma$ in (6.1) is considered to be the finite forces $\boldsymbol{\pi}_{q\mathrm{m}}$ and the limit $Q \mathrm{d} \Gamma \longrightarrow \pi_{q\mathrm{e}}$ of the infinitesimal charges $Q \mathrm{d} \Gamma$ in (6.2) to be the finite charges $\pi_{q\mathrm{e}}$ acting on the node pair q associated with positions $\mathbf{x}_q^+$ and $\mathbf{x}_q^-$. Then (6.1) and (6.2) degenerate to the discrete sums

$$\overline{\boldsymbol{\sigma}} = \frac{1}{V} \sum_{q=1}^{P} \mathrm{sym} \left[\boldsymbol{\pi}_{q\mathrm{m}} \otimes (\mathbf{x}_q^+ - \mathbf{x}_q^-) \right] , \tag{6.75}$$

and

$$\overline{\mathbf{D}} = -\frac{1}{V} \sum_{q=1}^{P} \pi_{qe} (\mathbf{x}_q^+ - \mathbf{x}_q^-). \tag{6.76}$$

Equations (6.75) and (6.76) can be written in a combined way as in the following

$$\overline{\mathbf{S}} = \frac{1}{V} \sum_{q=1}^{P} \mathbb{Z}_{\mathrm{c}q} \boldsymbol{\pi}_q. \tag{6.77}$$

In a compact way the last equation can be written as

$$\overline{\underline{\mathbf{S}}} = \frac{1}{V}\mathbb{Z}_{\mathrm{c}}\underline{\boldsymbol{\pi}}. \tag{6.78}$$

Replacing $\underline{\boldsymbol{\pi}}$ in (6.78) the following equation can be deduced,

$$\overline{\underline{\mathbf{S}}} = \frac{1}{V}\mathbb{Z}_{\mathrm{c}}\left[\mathbb{P}_{\mathrm{c}}\widetilde{\mathbf{K}}_{\mathrm{bb}}^{-1}\mathbb{P}_{\mathrm{c}}^{T}\right]^{-1}\mathbb{Z}_{\mathrm{c}}^{T}\overline{\mathbf{e}} + \frac{1}{V}\mathbb{Z}_{\mathrm{c}}\mathbb{P}_{\mathrm{c}}\widetilde{\mathbf{K}}_{\mathrm{bb}}^{-1}\widetilde{\mathbf{F}}_{\mathrm{b}}. \tag{6.79}$$

Comparing equations (6.12) and (6.79) the following relations can be deduced,

$$\mathbb{L} = \frac{1}{V}\mathbb{Z}_{\mathrm{c}}\left[\mathbb{P}_{\mathrm{c}}\widetilde{\mathbf{K}}_{\mathrm{bb}}^{-1}\mathbb{P}_{\mathrm{c}}^{T}\right]^{-1}\mathbb{Z}_{\mathrm{c}}^{T} \qquad \text{and} \qquad \underline{\mathbf{S}}^{0} = \frac{1}{V}\mathbb{Z}_{\mathrm{c}}\mathbb{P}_{\mathrm{c}}\widetilde{\mathbf{K}}_{\mathrm{bb}}^{-1}\widetilde{\mathbf{F}}_{\mathrm{b}}. \tag{6.80}$$

From equation (6.80) one can determine the homogenized material parameters similarly as the displacement type boundary conditions in Section 6.2.1.

6.3 Homogenization of configurational forces for piezoelectric materials

Because of the inhomogeneity in piezoelectric materials, it is essential to homogenize the Eshelby stress tensor to capture the effects of the micro discontinuities on the macro level. There are several approaches to determine the homogenized Eshelby stress tensor, see Ricker et al. [84]. In this work the direct approach is used to determine the homogenized Eshelby stress tensor

$$\overline{\boldsymbol{\Sigma}} = \frac{1}{V}\int_{\mathcal{B}_{\mathrm{mic}}}\boldsymbol{\Sigma}\,\mathrm{d}\Omega. \tag{6.81}$$

For the expression of $\boldsymbol{\Sigma}$ and its homogenization, the readers are referred to Section 5.2. The configurational force at node J at the macro level is

$$\mathbf{G}^{J} = \bigcup_{e\,=\,1}^{n_{\mathrm{el}}^{*}}\int_{\mathcal{B}^{e}}\overline{\boldsymbol{\Sigma}}\nabla N^{J}\,\mathrm{d}\Omega, \tag{6.82}$$

where n_{el}^{*} is the total number of adjacent elements to node J.

6.4   Numerical results and analyses

In this work the main focus is to establish a numerical technique which is capable of capturing the effects of micro inhomogeneities in piezoelectric materials on the macro responses. Here the configurational force at the crack tip of the macro domain is considered as the macro response. An effort has been given to figure out the influence of the underlying microstructure on the configurational force at the crack tip of a macro specimen. An extensive investigation is done to understand the influence of an external electric field on the configurational force at the crack tip. Here to do the homogenization, simplified micro domains or RVEs with different orientations of domains, domain walls and grains are used. All numerical results presented in this chapter are generated using only the Dirichlet boundary condition for the BVP on the micro level. All numerical results presented in this chapter are already published in Khalaquzzaman et al. [47].

6.4.1   Macro geometry and microstructure

A 4 mm$\times 4$ mm macro specimen with a horizontal sharp crack (see Figure 6.1) is simulated to determine the configurational forces at the crack tip.
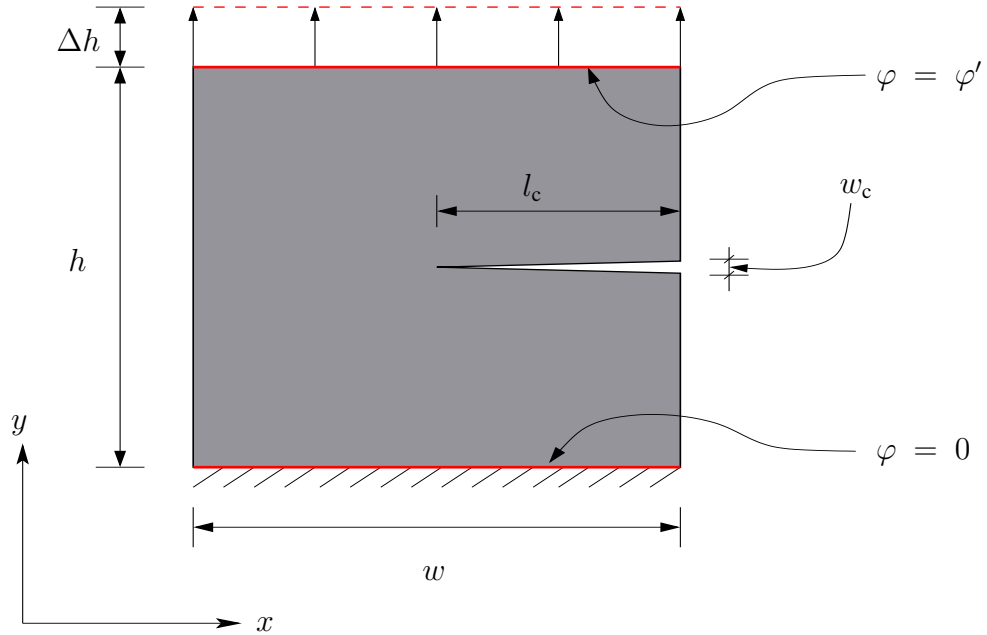

Figure 6.1: *A macro domain with dimension $h \times w$ contains a sharp crack with crack length l_c and width at opening w_c. The top of the structure is displaced with Δh and the applied potentials on the top and the bottom are φ' and 0, respectively*

A FE^2-based computational homogenization is performed for different microstructures assigned to each Gauß point of the macro domain. The length of the crack l_c is 2 mm, and the width of the crack at the opening w_c is 0.1 mm. In all simulations the bottom boundary of the macro domain remains fixed, and the top boundary is displaced by 0.2 mm. Three different electric field situations are taken into account to simulate the problem: no external electric field, nominal upward electric field, and nominal downward electric field. These electric field situations are realized by prescribing the electric potentials on the top and the bottom red boundaries (see Figure 6.1) of the macro specimen.

6.4.2   Material parameters

In this chapter all simulations are done for poled soft lead zirconate titanate (PZT) piezoelectric ceramics. The material parameters in Voigt-notation are given in the following:

$$
\begin{aligned}
\mathbb{C} &= \begin{bmatrix} 12.6 & 5.3 & 0.0 \\ 5.3 & 11.7 & 0.0 \\ 0.0 & 0.0 & 3.53 \end{bmatrix} \cdot 10^4 \frac{\mathrm{N}}{\mathrm{mm}^2}, \\
\mathbb{b} &= \begin{bmatrix} 0.0 & 0.0 & 17.0 \\ -6.5 & 23.3 & 0.0 \end{bmatrix} \cdot 10^{-6} \frac{\mathrm{C}}{\mathrm{mm}^2}, \\
\mathbf{A} &= \begin{bmatrix} 1.51 & 0.0 \\ 0.0 & 1.3 \end{bmatrix} \cdot 10^{-11} \frac{\mathrm{C}}{\mathrm{Vmm}}.
\end{aligned}
\tag{6.83}
$$

These material data are taken from McMeeking and Ricoeur [60]. This data set prescribes a material which is poled in the direction of the positive y-axis. The polarization in the positive y-direction is also considered by assigning

$$
\underline{\varepsilon}^0 = [-0.0039 \quad 0.0076 \quad 0.0]^T \quad \text{and} \quad \underline{\mathbf{P}}^0 = [0.0 \quad 0.2]^T \cdot 10^{-6} \frac{\mathrm{C}}{\mathrm{mm}^2}.
\tag{6.84}
$$

For piezoelectric materials poled with other orientations, the material parameters are transformed by multiplication of the corresponding rotation tensor.

6.4.3   Configurational forces in the micro domain

To determine the boundary conditions of the micro domain, the macro displacement gradient and the macro electric field are provided to the micro level. By using equations (6.5) and (6.8) the displacement and the potential boundary conditions are determined. To simulate this micro problem, the following macro displacement gradient and electric field are used

$$\overline{\nabla \mathbf{u}} = \begin{bmatrix} 0.1 & 0.05 \\ 0.07 & 0.15 \end{bmatrix} \quad \text{and} \quad \overline{\mathbf{E}} = \begin{bmatrix} 0 \\ 5 \end{bmatrix} \cdot 10^5 \frac{\text{V}}{\text{mm}}.$$

The micro domain in Figure 6.2(a) with three domains and two vertical domain walls is simulated. The central domain is poled downward, and the other two domains are poled upward. Figure 6.2(b) shows the nodal configurational forces (red arrows) on the domain walls. Here on the boundary of the micro domain, large configurational forces appear which are not plotted.

(a)   (b)
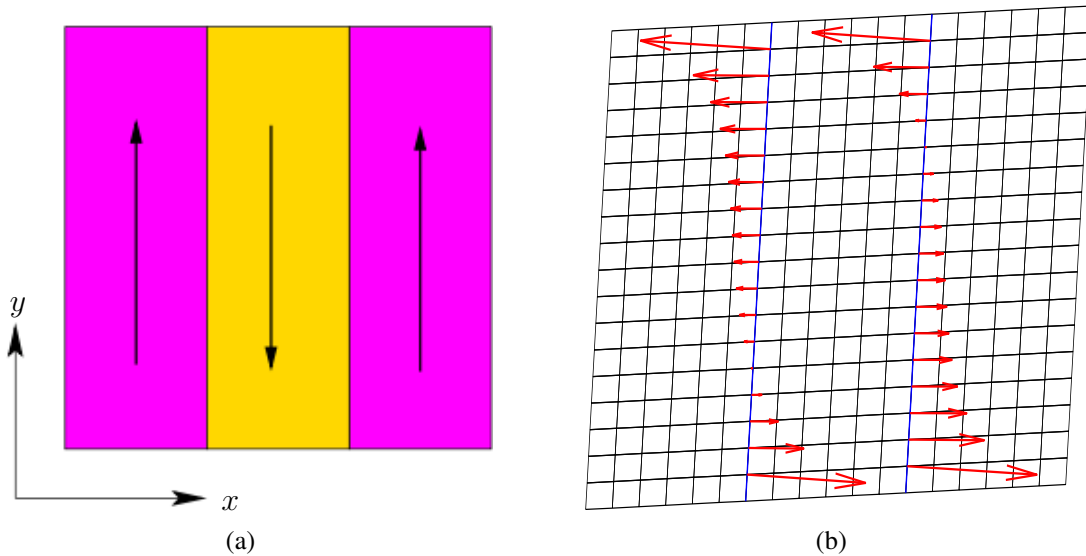
Figure 6.2: *Configurational forces on the domain walls of the microstructure*

6.4.4 Influence of different microstructures without external electric field

<div align="center">(a)</div>

<div align="center">(b)</div>

<div align="center">(c)</div>

<div align="center">(d)</div>
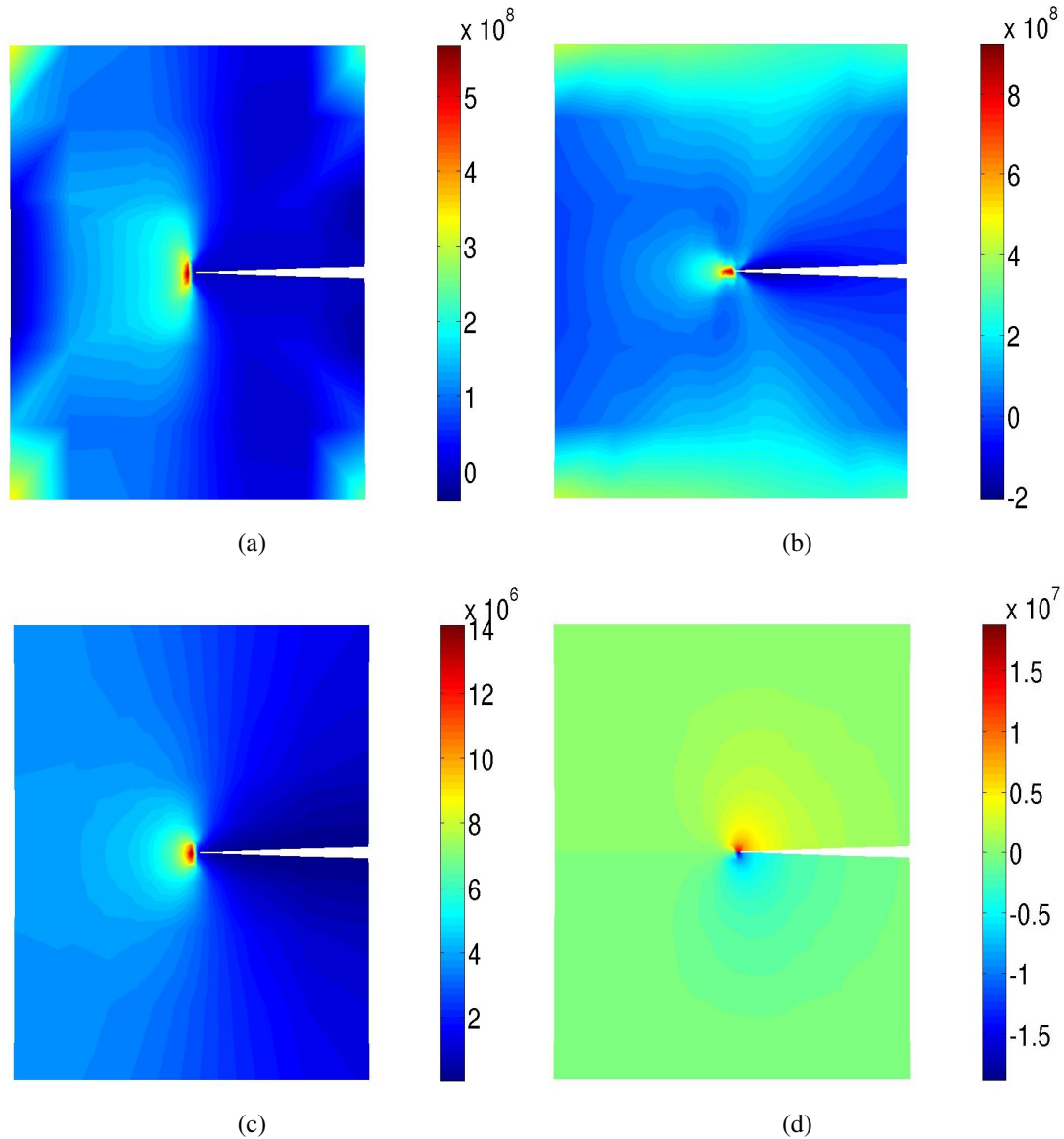
Figure 6.3: *Stress and electric field distributions on macroscopic specimen:* (a) σ_{yy} *component of the stress tensor in* N/m^2, (b) σ_{xx} *component of the stress tensor in* N/m^2, (c) E_y *component of the electric field in* V/m, (d) E_x *component of the electric field in* V/m

Figure 6.3(a) - 6.3(d) show the stress and the electric field distributions in the macro specimen which is simulated with the homogenized material parameters. At the crack tip of this macro specimen, the stress or the electric field concentrations or singularities are

visible. These are the reasons for the appearance of a large configurational force at the crack tip, see Figure 6.4. It may cause crack propagation in the opposite direction of the configurational force at the crack tip.

The top row in Figure 6.4 and 6.5 shows the corresponding micro domains or RVEs which are assigned to every Gauß point of the macro domain, and in the second rows are the deformed macro domains with configurational forces at the crack tip, and at the bottom the numerical values of the configurational forces at the crack tip are shown. The red arrows at the crack tips of the macro domains indicate the direction and the value of the configurational forces at the crack tip. The significance of the configurational forces is that the crack propagates in the opposite direction of the configurational force, and the amount of the propagation depends on the value of the configurational force.

$$\mathbf{G} = \begin{bmatrix} 608.48 \\ 0.000 \end{bmatrix} \mathbf{N} \qquad \mathbf{G} = \begin{bmatrix} 608.53 \\ 0.000 \end{bmatrix} \mathbf{N} \qquad \mathbf{G} = \begin{bmatrix} 745.30 \\ 34.894 \end{bmatrix} \mathbf{N}$$

Figure 6.4: *Configurational forces for different microstructures without external electric field*

Figure 6.4(a) shows that when the assigned micro domain is homogeneous and poled upward, there is a horizontal configurational force of 608.48 N. In Figure 6.4(b) the assigned micro domain has three domains with two vertical $180°$ domain walls. The two outer domains are poled upward, and the middle domain is poled downward. In this case the configurational force is approximately the same as in the previous case. The reason is that the mechanical properties do not change if the remanent polarization points to the opposite direction. Thus, the material behavior remains unchanged if no electric field is applied. In Figure 6.4(c) the corresponding micro domain has three domains and two horizontal $90°$-domain walls, here the polarizations are inclined by $45°$. In this case we get an upward inclined configurational force with a y-component of 34.894 N and a x-component of 745.30 N. This implies that the crack may move in an inclined direction with respect to the x-axis.

$$\mathbf{G} = \begin{bmatrix} 879.19 \\ 0.000 \end{bmatrix} \mathrm{N} \qquad \mathbf{G} = \begin{bmatrix} 879.16 \\ 0.000 \end{bmatrix} \mathrm{N} \qquad \mathbf{G} = \begin{bmatrix} 745.29 \\ 34.904 \end{bmatrix} \mathrm{N} \qquad \mathbf{G} = \begin{bmatrix} 793.62 \\ 0.000 \end{bmatrix} \mathrm{N}$$
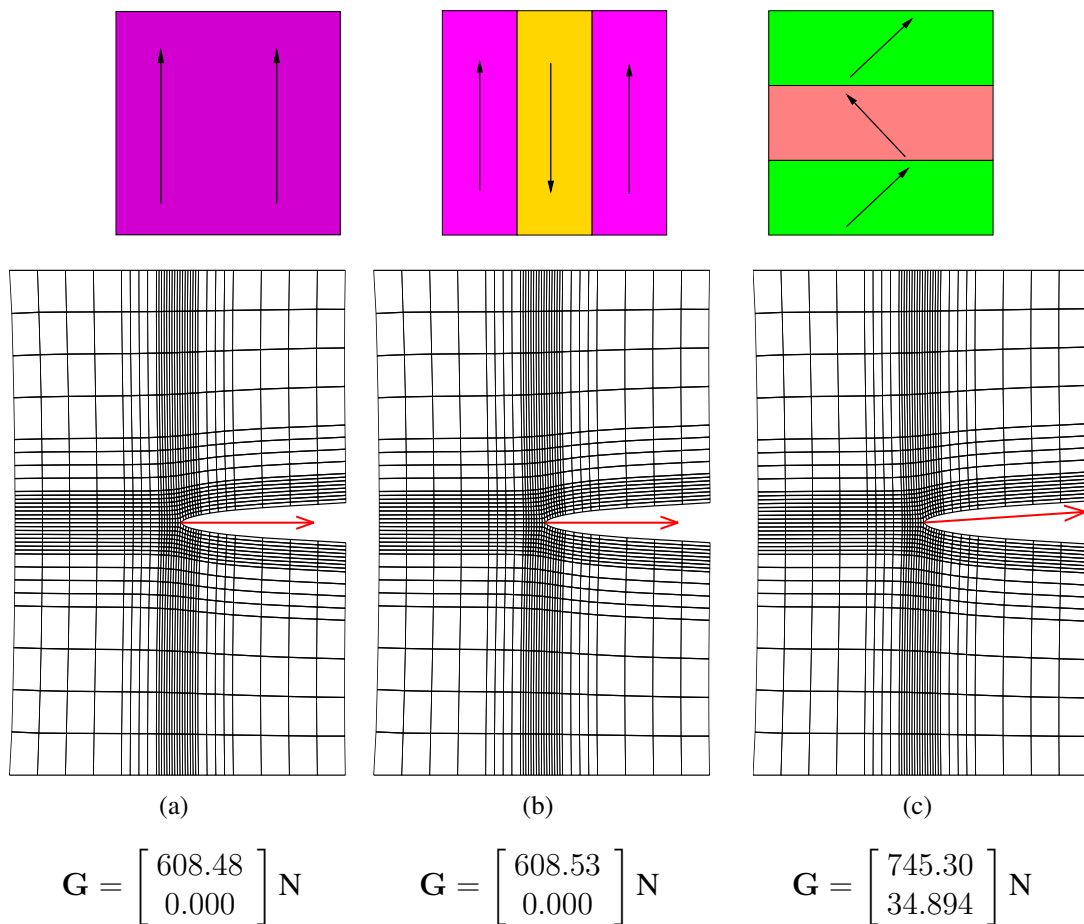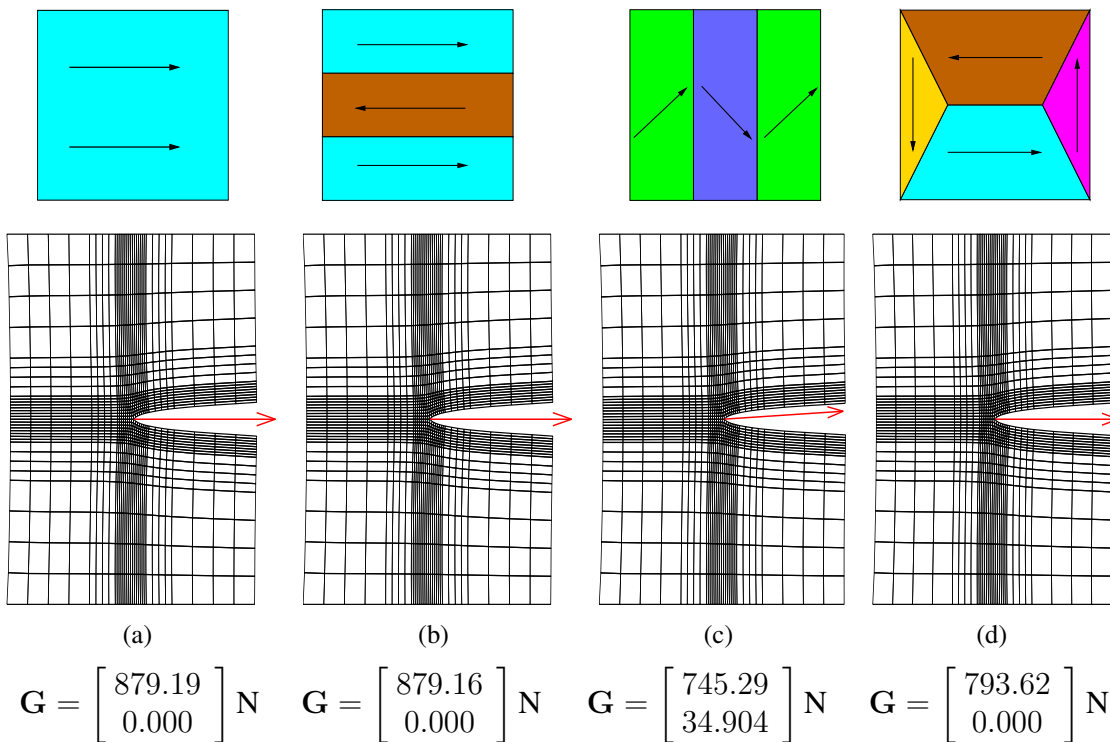
Figure 6.5: *Configurational forces for different microstructures without an external electric field*

In Figure 6.5(a) the assigned micro domain is homogeneous and horizontally poled in the positive x-axis. In this case a horizontal configurational force of 879.19 N, which is larger than the configurational force in Figure 6.4(a), appears at the crack tip. Similar to

Figure 6.4(a) or 6.4(b), Figure 6.5(b) gives an almost identical configurational force as in Figure 6.5(a). In Figure 6.5(c) the assigned micro domain comprises three domains of inclined polarity and two vertical $90°$-domain walls. In this case one gets a similar configurational force as in Figure 6.4(c). In Figure 6.5(d) the microstructure has four domains: two are horizontally poled and the other two are vertically poled. This results in four $90°$-domain walls. In this case the configurational force has an x-component of 793.62 N and no y-component.

It is worthwhile to point out the two extreme cases of configurational forces: if the polarization is horizontal, the value of the configurational force is maximal; and if it is vertically poled, the value of the configurational force is minimal. The other cases give an intermediate value of the configurational forces between the two extreme values. The components of the elasticity tensor in the poling direction have lower values which means that the material is more rigid in the transverse direction to the polarization than in the poling direction. For that reason, the minimum configurational force is obtained if the mechanical displacement is applied in the poling direction.

6.4.5   Influence of an external electric field

In this section simulations are carried out for different external electric field conditions. In each example results are compared among three cases: merely mechanical loading, mechanical loading along with upward external electric field and mechanical loading along with downward external electric field. In Figure 6.6 the simulations are done with a micro domain poled in the direction of the mechanical displacement. The simulation without external electric field results in a horizontal configurational force of 608.16 N while the simulation with the upward external electric field results in a smaller horizontal configurational force of 278.66 N. Meanwhile the simulation with downward electric field gives also a smaller horizontal configurational force of 293.80 N. It is noticeable that for both upward and downward external electric fields the configurational forces are reduced by more than 50%.

Figure 6.6: *Configurational forces for different electric loadings using a microstructure which contains vertical domain walls*

In Figure 6.7 the simulations are done for a micro domain poled in the direction perpendicular to the mechanical displacement. The simulation without external electric field gives a horizontal configurational force of 879.16 N. The simulation with upward external electric field reduces the configurational force by a significant amount, and it produces a small positive y-component. Similar results are found in the case with downward external electric field. It is also noted that there is a reduction of the configurational force in the presence of either an upward or a downward electric field. The reduction is approximately 50%.
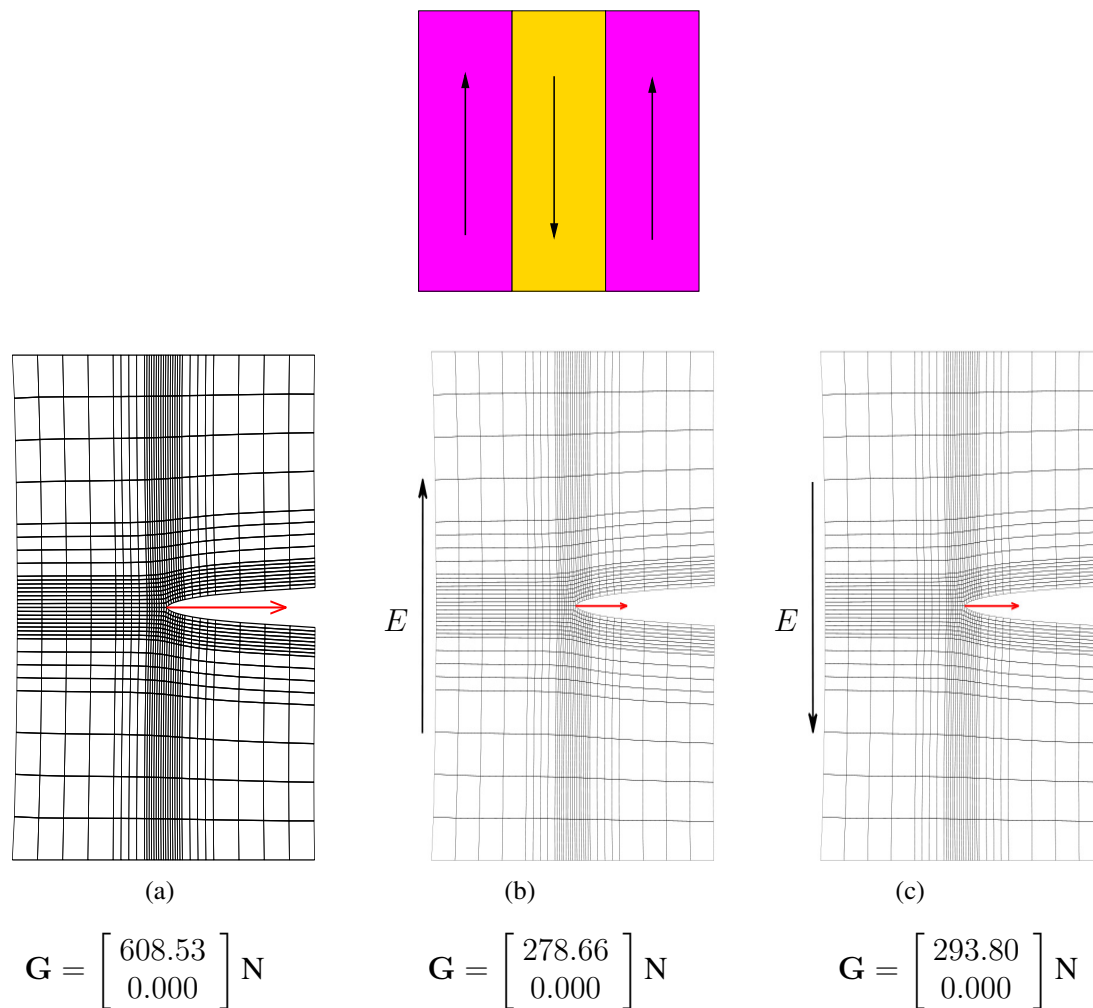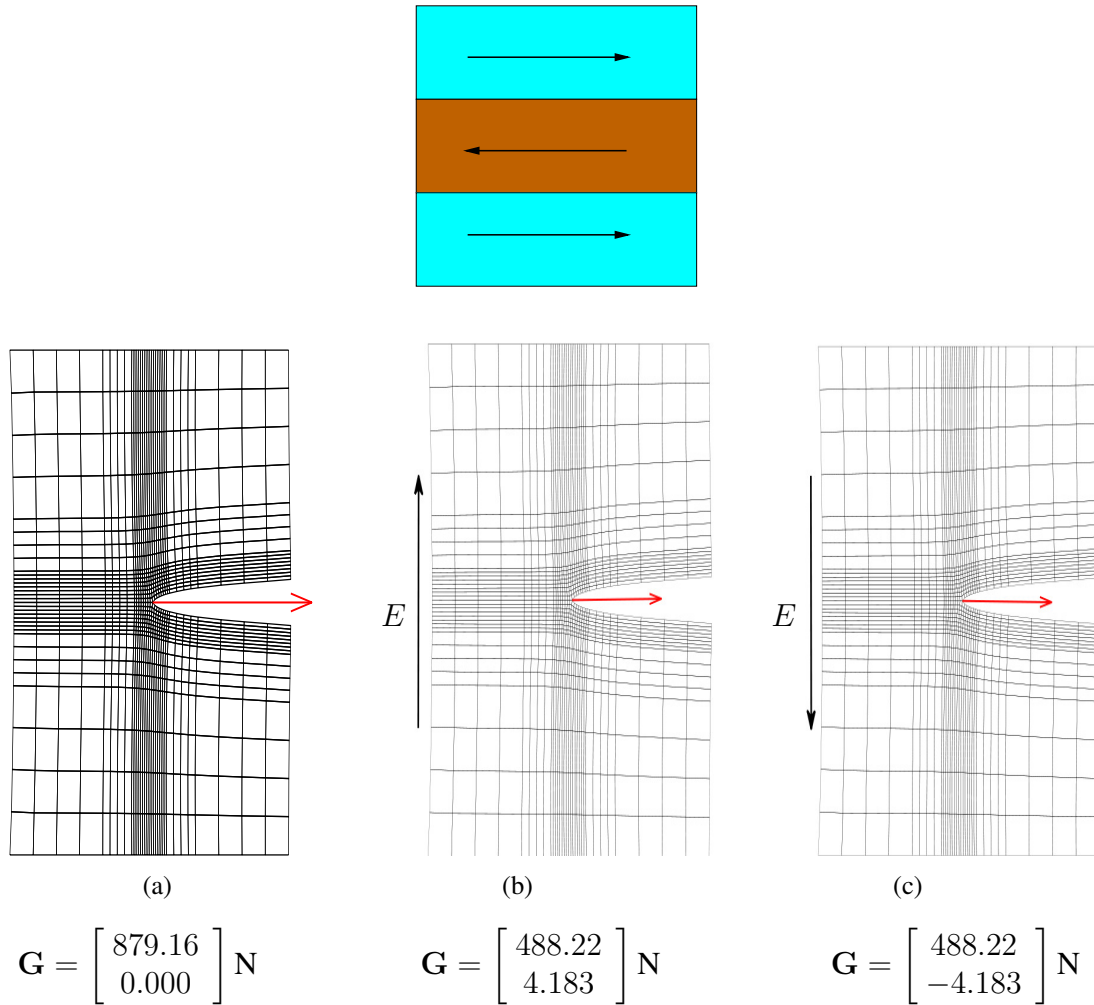
Figure 6.7: *Configurational forces for different electric loading using a microstructure which contains horizontal domain walls*

All previous simulations were done for simple micro domains or RVEs. These micro domains or RVEs may not represent the real situation of the micro inhomogeneities of piezoelectric materials. The microstructures in real problems feature complex inhomogeneities, for example domains, domain walls, micro cracks, grains, grain boundaries, etc. In attempt to obtain a better approximation of the real situation regarding the micro inhomogeneities, the micro domain in Figure 6.8 is used. In this micro domain there are five grains enclosed by the boundaries (red). Each grain features domains and domain walls. When the simulation is done only for mechanical displacement, a configurational force with an x-component of 741.97 N and a y-component of -33.168 N is obtained. These values imply that the crack may propagate in an inclined direction to the x-axis.

When external field is present, either downward or upward, the configurational forces are
reduced to an x-component of 386.21 N and a y-component of -26.173 N. The degree
of the reduction in the components of the configurational force are not equal. Comparing
with the case of without electric field, the direction of the configurational force is also
changed.

$$\mathbf{G} = \begin{bmatrix} 741.97 \\ -33.168 \end{bmatrix} \mathrm{N} \qquad \mathbf{G} = \begin{bmatrix} 386.21 \\ -26.173 \end{bmatrix} \mathrm{N} \qquad \mathbf{G} = \begin{bmatrix} 386.24 \\ -26.205 \end{bmatrix} \mathrm{N}$$
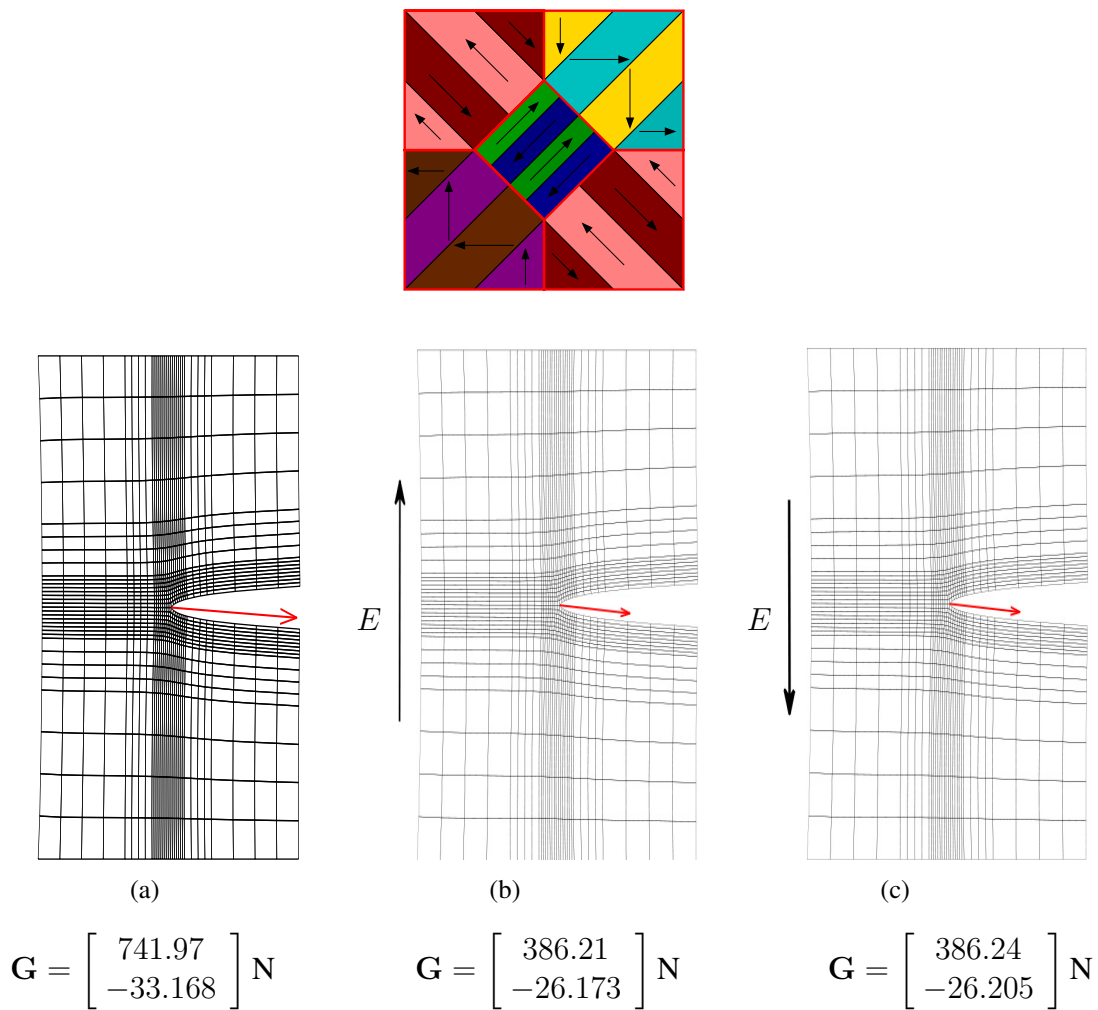
Figure 6.8: *Configurational forces for different electric loadings using a relatively complex microstructure*

The calculated configurational forces for different microstructures and different external
electric field conditions are in Figure 6.9.
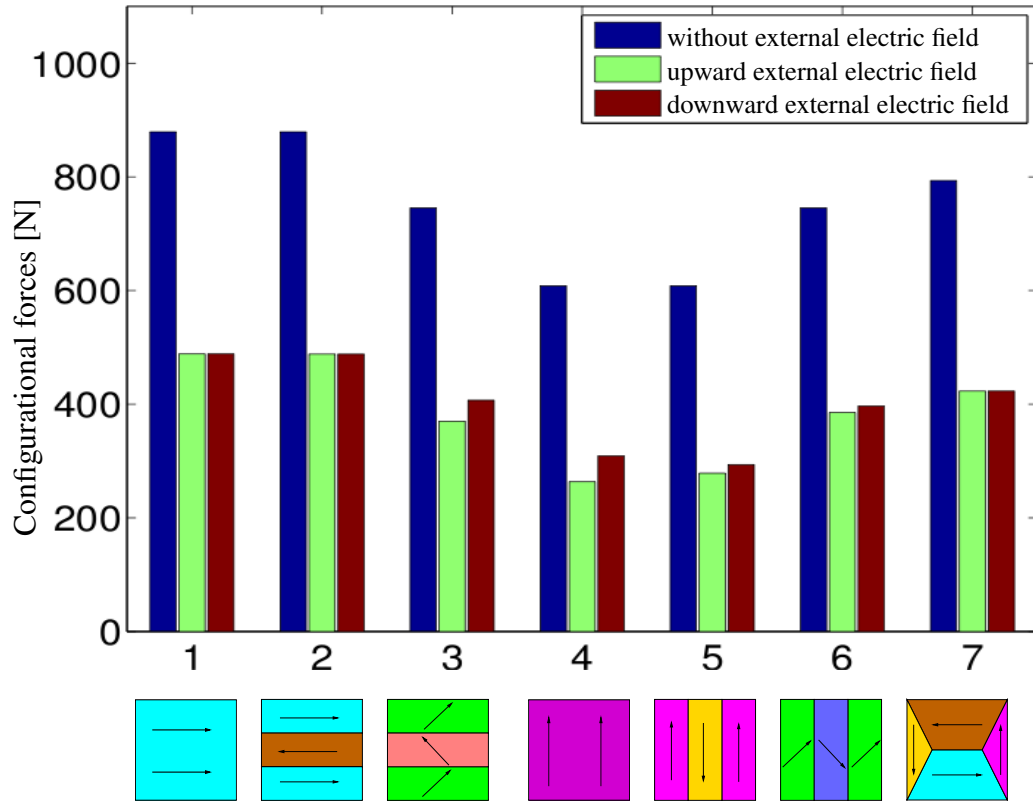
Figure 6.9: *Absolute value of the configurational forces for different microstructures with different electric loadings*

6.4.6 Influence of the material parameters

The simulation results shown in Figure 6.10(b) - 6.10(d) and 6.11(b) - 6.11(d) are produced by using different sets of material parameters. The set of material parameters in Section 6.4.2 is considered as one of the sets of material parameters. Other sets of material parameters are obtained through different combinations of the material parameters in the following

$$
\begin{aligned}
\mathbb{b}_{\mathrm{mod}} &= \begin{bmatrix} 0.0 & 0.0 & 17.0 \\ -6.5 & 23.3 & 0.0 \end{bmatrix} \cdot \mathbf{10^{-4.5}} \frac{\mathrm{C}}{\mathrm{mm}^2}, \\
\underline{\mathbf{A}}_{\mathrm{mod}} &= \begin{bmatrix} 1.51 & 0.0 \\ 0.0 & 1.3 \end{bmatrix} \cdot \mathbf{10^{-14}} \frac{\mathrm{C}}{\mathrm{Vmm}}, \\
\underline{\mathbf{P}}^0_{\mathrm{mod}} &= \begin{bmatrix} 0.0 \\ 0.2 \end{bmatrix} \cdot \mathbf{10^{-4.5}} \frac{\mathrm{C}}{\mathrm{mm}^2}.
\end{aligned}
\tag{6.85}
$$

Figure 6.10: *Dependence of configurational forces on the electric field for different material parameters: (c) polarization and piezoelectric material constant; (d) dielectric material constant*

Figure 6.10(b) - 6.10(d) and 6.11(b) - 6.11(d) show the plots (configurational forces at crack tip vs. applied potential difference to the macro domain) for different mechanical loads. The simulation results in Figure 6.10(b) - 6.10(d) are determined using the micro domain presented in Figure 6.10(a). The simulation results in Figure 6.10(b) are determined using the material parameters from Section 6.4.2. The plots in Figure 6.10(b) show that the curves are parabolic with negative curvature. The reason lies in the fact that the main contribution to the configurational forces is coming from the electric enthalpy which has a quadratic term comprising the electric field. The plots in Figure 6.10(b) are approximately symmetric. If larger values for the piezoelectric constants (e.g., $\underline{\mathbb{b}}_{\mathrm{mod}}$ of (6.85)) and remanent polarizations (e.g., $\underline{\mathbf{P}}^0_{\mathrm{mod}}$ of (6.85)) are being used, the parabolic curves shift to the right, see Figure 6.10(c). In the case with smaller dielectric constants (e.g.,

$\underline{\mathbf{A}}_{\mathrm{mod}}$ of (6.85)), the plots are flattened, see Figure 6.10(d). The plots in Figure 6.11(b) - 6.11(d) are produced by using a micro domain with horizontal polarization as shown in Figure 6.11(a) and with the same set of material parameters used for the results in Figure 6.10. A similar dependence of the configurational forces on the material parameters is observed.
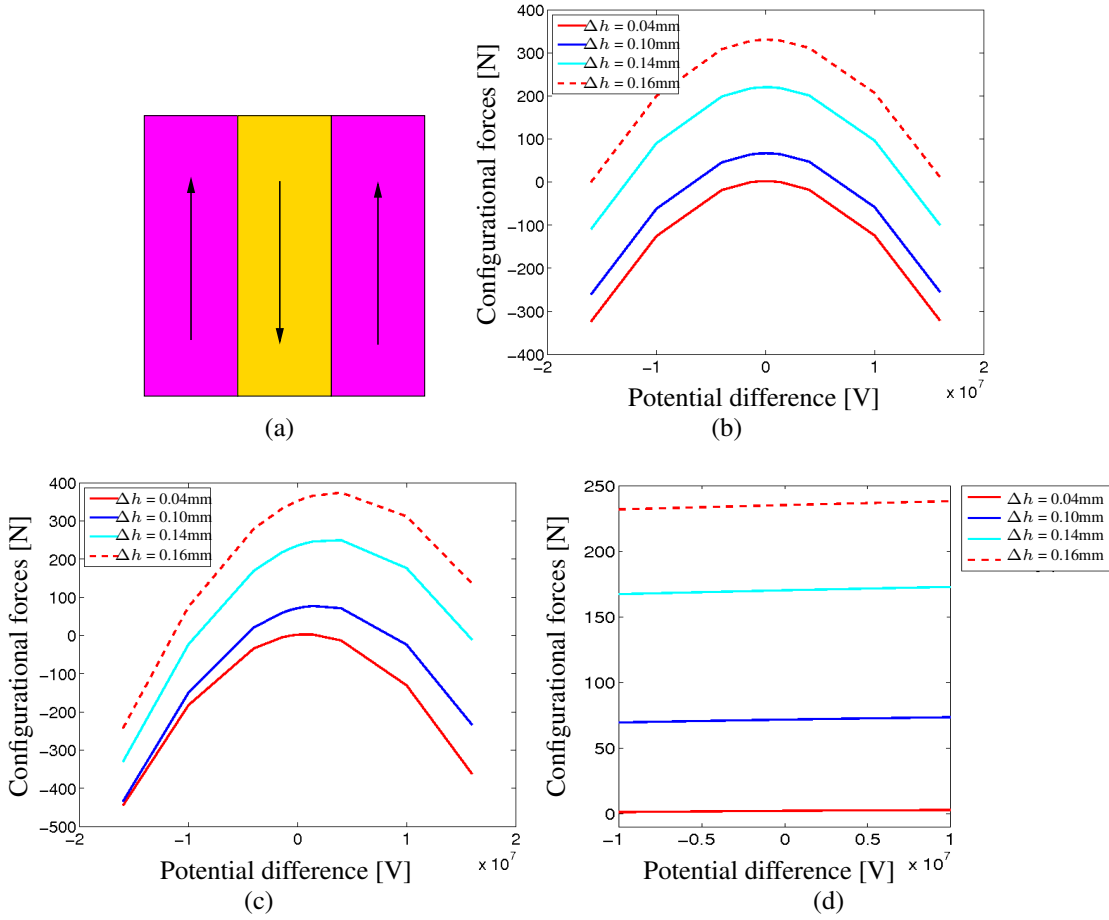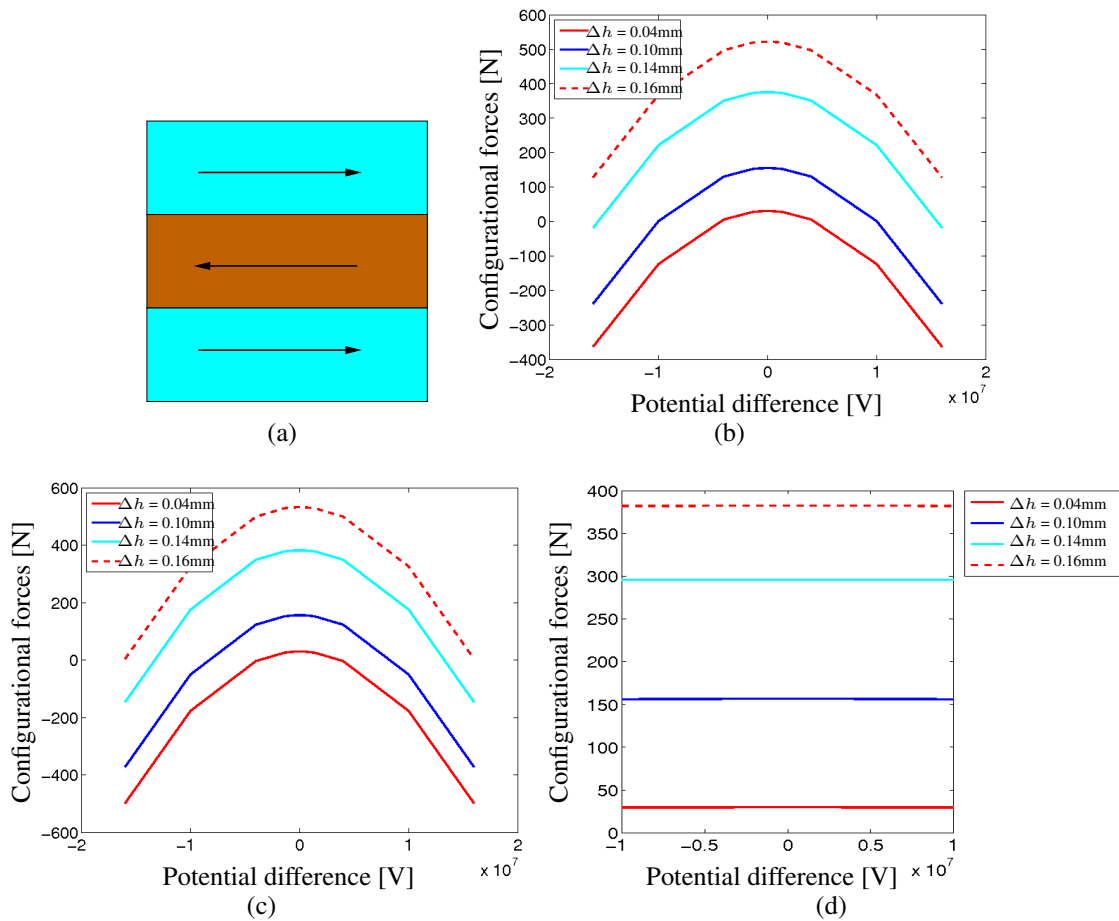

Figure 6.11: *Dependence of configurational forces on the electric field for different material parameters: (c) polarization and piezoelectric material constant; (d) dielectric material constant*

Chapter 7

Homogenization of piezoelectric materials using evolving microstructures

In the previous chapter, the investigation of the configurational forces at the macro crack tip was carried out using a fixed or non-evolving microstructure as the representative volume element (RVE). In other words, the movement of the domain wall was neglected. But in real situations, one has no direct control over the movement of the domain walls. The movement of the interface can be induced by an external electric and/or mechanical loading. If an electric field larger than the critical electric field is applied to a piezoelectric specimen, the domain walls can move. Thus, homogenization using evolving microstructures is required to obtain physically more accurate simulation results. As a consequence of the evolution of the microstructure, it is necessary to update the micro domain at every step of the homogenization during the the application of a varying electric field.

7.1 Domain wall driving force and interface kinetics

As stated previously, domain walls in ferroelectric materials can be modeled in two different ways: one is the sharp interface approach, and the other one is the phase field model approach. Here the sharp interface approach is used. The assumption for the sharp in-

terface model is that each ferroelectric domain is considered as a homogeneous domain and is separated by a domain wall with zero thickness. For this reason the geometry of the domain wall $\mathcal{S}$ can be seen as an internal variable of the electric enthalpy. For a RVE with a single interface, the dependence of the electric enthalpy on this position can be expressed by

$$
\begin{aligned}
\bar{H}(\boldsymbol{\varepsilon}, \mathbf{E}, \mathbf{X}; \mathcal{S}) \;=\; & \frac{1}{2}(\boldsymbol{\varepsilon} - \boldsymbol{\varepsilon}_{\pm}^0)\!:\!\left[\mathbb{C}_{\pm}(\boldsymbol{\varepsilon} - \boldsymbol{\varepsilon}_{\pm}^0)\right] - (\boldsymbol{\varepsilon} - \boldsymbol{\varepsilon}_{\pm}^0)\!:\!(\mathbb{b}_{\pm}^T \mathbf{E}) \\
& -\frac{1}{2}\mathbf{E}\!\cdot\!(\mathbf{A}_{\pm}\,\mathbf{E}) - \mathbf{P}_{\pm}^0\!\cdot\!\mathbf{E},
\end{aligned}
\tag{7.1}
$$

where the material parameter $(\cdot)_+$ is considered if $\mathbf{X} \in \mathcal{B}^+$ and $(\cdot)_-$ is considered if $\mathbf{X} \in \mathcal{B}^-$ (see Figure 4.1).

Recalling the Eshelby stress tensor for piezoelectric materials

$$
\boldsymbol{\Sigma} = H\,\mathbf{1} - (\nabla\,\mathbf{u})^T \boldsymbol{\sigma} - \nabla\,\varphi \otimes \mathbf{D},
\tag{7.2}
$$

the configurational force balance (4.25) can be reduced in this case to the jump relation

$$
[\![\boldsymbol{\Sigma}]\!]\mathbf{n}_{\mathcal{S}} + \mathbf{G}_{\mathcal{S}} = \mathbf{0},
\tag{7.3}
$$

where $\mathbf{G}_{\mathcal{S}}$ is the surface configurational force acting on the domain wall, i.e. a force per unit area, and $\mathbf{n}_{\mathcal{S}}$ is the normal vector to the domain wall pointing towards the domain $\mathcal{B}^+$, see Figure 4.1. If the domain wall moves with velocity $\mathbf{w}_{\mathcal{S}}$, the energy dissipation due to this movement is given by

$$
\mathcal{D} = -\int_{\mathcal{S}} \mathbf{G}_{\mathcal{S}}\!\cdot\!\mathbf{w}_{\mathcal{S}}\mathrm{d}\Gamma = \int_{\mathcal{S}} \tau_n w_n \mathrm{d}\Gamma \geqslant 0.
\tag{7.4}
$$

Hereby the fact is considered that only the normal component of the configurational force on the interface has a contribution to the dissipation. In the above equation the following quantities are used,

$$
\tau_n = -\mathbf{G}_{\mathcal{S}}\!\cdot\!\mathbf{n}_{\mathcal{S}} = \mathbf{n}_{\mathcal{S}}\!\cdot\![\![\boldsymbol{\Sigma}]\!]\mathbf{n}_{\mathcal{S}} \quad \text{and} \quad w_n = \mathbf{w}_{\mathcal{S}}\!\cdot\!\mathbf{n}_{\mathcal{S}}.
\tag{7.5}
$$

Recalling the resulting configurational force at node K, which was obtained by assembling all n_e elements adjacent to node K, we have

$$\mathbf{G}^K = \bigcup_{e=1}^{n_e} \mathbf{G}_e^K. \tag{7.6}$$

The normal component of the configurational force G_n acting on the interface $\mathcal{S}$ is formulated by

$$G_n = \sum_K \mathbf{G}_{\mathcal{S}}^K \cdot \mathbf{n}_{\mathcal{S}}, \tag{7.7}$$

where the summation includes all nodes located on the interface $\mathcal{S}$. Furthermore, scalar multiplication of the balance of configurational forces on $\mathcal{S}$ in (7.3) with $-\mathbf{n}_{\mathcal{S}}/A_{\mathcal{S}}$ and integration over $\mathcal{S}$ leads to

$$-\frac{1}{A_{\mathcal{S}}} \int_{\mathcal{S}} \mathbf{G}_{\mathcal{S}} \cdot \mathbf{n}_{\mathcal{S}} \mathrm{d}\Gamma = \frac{1}{A_{\mathcal{S}}} \int_{\mathcal{S}} \tau_n \mathrm{d}\Gamma = T_n. \tag{7.8}$$

With the help of the finite element approximation (4.36), the average domain wall driving force on $\mathcal{S}$ is determined from

$$T_n = -\frac{1}{A_{\mathcal{S}}} \int_{\mathcal{S}} \mathbf{G}_{\mathcal{S}} \cdot \mathbf{n}_{\mathcal{S}} \mathrm{d}\Gamma = -\frac{1}{A_{\mathcal{S}}} \sum_K \mathbf{G}_{\mathcal{S}}^K \cdot \mathbf{n}_{\mathcal{S}} = -\frac{1}{A_{\mathcal{S}}} G_n. \tag{7.9}$$

The formulations shown above do not state a specific kinetic law for the interface normal velocity w_n. To establish such a relationship, experimental investigations by Flippen [21] are taken into consideration. In these experiments the dynamics of the $180°$ domain wall between two domains in Gadolinium Molybdate (GMO) single crystal was investigated, in that a domain wall was relocated through the material by applying an external homogeneous electric field E parallel to the interface or the domain wall. The measurements show a linear relationship between the interface velocity w_n and the electric field E. The kinetic law can be formulated in terms of the applied electric field by

$$w_n = \bar{\mu}(E - E_0). \tag{7.10}$$

The parameter $\bar{\mu}$ denotes the mobility of the domain wall or the interface, and E_0 is the threshold or critical electric field for domain wall movement. It is noted that this simplified relation is only applicable for the homogeneous electric field. In the case of inhomogeneous fields, which are present in general, and with the consideration of the

second law (7.4), the kinetic law is required to be reformulated in terms of the wall driving force τ_n (or the averaged resulting wall driving force T_n) acting on the interface. As the domain walls are only modeled as plane interfaces here, the normal velocity w_n is homogeneous on the interface $\mathcal{S}$, i.e. the interface moves only by translation. Thus, kinetic law for the interface normal velocity w_n is to be formulated as a function of T_n. Figure 7.1 shows one thermodynamically admissible constitutive relation. The postulated kinetic law can be written as

$$
w_n = \begin{cases} \mu(T_n - T_0) & \text{if } T_n \geqslant T_0, \\ 0 & \text{if } |T_n| \leqslant T_0, \\ \mu(T_n + T_0) & \text{if } T_n \leqslant -T_0. \end{cases} \tag{7.11}
$$

The parameters μ and T_0 are the interface mobility and the threshold of the averaged driving force, respectively. It can be stated that this relationship implies the assumption that the interface kinetics is invariant of the dimensions of the interface. Some recent investigative works on the dynamics of domain walls in GMO can be found in Shur et al. [95, 96, 97].
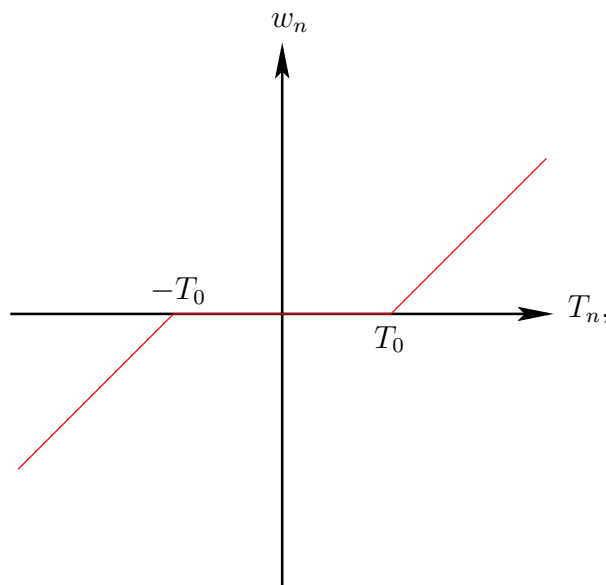
Figure 7.1: *Kinetics of the domain wall movement*

The wall driving force on a $180°$-domain wall in the presence of an external electric field E parallel to the interface can be determined from (7.5). As derived in Appendix A.4.1, this wall driving force is approximated by

$$\tau_n \approx [\![\mathbf{P}^0 \cdot \mathbf{E}]\!] = 2P^0 E, \tag{7.12}$$

where $P^0 = |\mathbf{P}^0|$, see Loge and Suo [56]. The value of T_0 is determined from (7.8) and (7.12) for $E = E_0$

$$T_0 = \frac{1}{A_\mathcal{S}} \int_\mathcal{S} \tau_n(E_0) \mathrm{d}\Gamma = \tau_n(E_0) = 2P^0 E_0. \tag{7.13}$$

For $E = 2E_0$ and evidently $T_n = 2T_0$, the combination of (7.10) and (7.11) leads to

$$w_n = \mu(T_n - T_0) = \mu T_0 = 2\mu P^0 E_0 = \bar{\mu} E_0, \tag{7.14}$$

which infers

$$\mu = \frac{\bar{\mu}}{2P^0}. \tag{7.15}$$

The value for $\bar{\mu}$ and E_0 can be found in Flippen [21].

Similarly, for a $90°$-domain wall,

$$\tau_n \approx [\![\mathbf{P}^0 \cdot \mathbf{E}]\!] = 2P_2^0 E, \tag{7.16}$$

where P_2^0 is the vertical component of $\mathbf{P}^0$. The threshold wall driving force $T_0 = 2P_2^0 E_0$ and wall mobility parameter $\mu = \bar{\mu}/2P_2^0$.

7.1.1 Time integration

The Euler forward (or an explicit) time integration formula is applied to obtain a discretized form of the kinetic law (7.11) in time. Hence the discretized position (only w.r.t. time) of the domain wall can be formulated as

$$X_\mathcal{S}^{n+1} = X_\mathcal{S}^n + w_n^n \triangle t, \tag{7.17}$$

where the indices n, $n + 1$ represent the current time step t_n and the next time step t_{n+1}, respectively. And $\triangle t$ is the time increment, which is here considered as constant for simplicity of the numerical computations. The interface velocity at the time step t_n is denoted by w_{n}^n. The interface velocity can be determined by using equation (7.11).
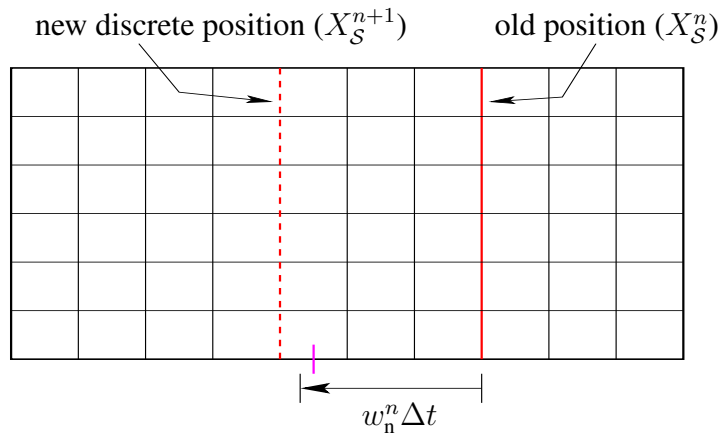
Figure 7.2: *Determination of new interface position $X_{\mathcal{S}}^{n+1}$ in micro domain*

A coincidence of the new domain wall position $X_{\mathcal{S}}^{n+1}$ with element boundaries is unlikely for an arbitrary choice of constant time step. To ensure that the new interface position coincides with element boundaries, one needs to remesh the microstructures at every time step, which is computationally inefficient. To avoid this remeshing of the micro domain at each time step, an approximation scheme is used. The mesh of the micro domain is regular and remains untouched. By using equation (7.17) the new position of the domain wall is calculated, and then the closest element boundaries are taken as the new discrete position of the domain wall. To lower the error in the time integration, a sufficiently fine mesh for the micro domain is required. The approximation scheme is demonstrated in Figure 7.2. After determining the discrete interface position at the time step t_{n+1}, the updated boundary value problem for piezoelectric materials at t_{n+1} can be solved on the micro level. Hence the computational homogenization of piezoelectric materials can be performed by using the evolved microstructure.

7.2 Numerical results and analyses

The results of the homogenization of piezoelectric materials containing evolving microstructures are described in this section. The numerical results are mainly presented for the configurational forces.

7.2.1 Material parameters

In the following all simulations are done for Gadolinium Molybdate (GMO). The material parameters in Voigt-notation are the following:

$$
\begin{aligned}
\mathbb{C} &= \begin{bmatrix} 6.82 & 2.0 & 0.0 \\ 2.0 & 9.82 & 0.0 \\ 0.0 & 0.0 & 2.55 \end{bmatrix} \cdot 10^4 \frac{\text{N}}{\text{mm}^2}, \\
\underline{\mathbb{b}}_\pm &= \begin{bmatrix} 0.0 & 0.0 & \pm 17.0 \\ \mp 6.5 & \pm 23.3 & 0.0 \end{bmatrix} \cdot 10^{-8} \frac{\text{C}}{\text{mm}^2}, \\
\underline{\mathbf{A}} &= \begin{bmatrix} 8.41 & 0.0 \\ 0.0 & 9.29 \end{bmatrix} \cdot 10^{-14} \frac{\text{C}}{\text{Vmm}}.
\end{aligned}
\tag{7.18}
$$

The polarization is also considered by assigning

$$
\underline{\varepsilon}^0 = [-0.004 \quad 0.024 \quad 0.0]^T \quad \text{and} \quad \underline{\mathbf{P}}_\pm^0 = [0.0 \quad \pm 0.002]^T \cdot 10^{-6} \frac{\text{C}}{\text{mm}^2}.
\tag{7.19}
$$

Numerical values of the interface mobility $\bar{\mu}$ in (7.15) can be found in Flippen [21], Toda et al. [106] and Shur et al. [95]. The value of the interface mobility parameter, $\bar{\mu} = 2.1 \cdot 10^{-6}$ m^2/(Vs), is taken into account to determine the value of the other mobility parameter μ as

$$
\mu = \frac{\bar{\mu}}{2P_0} = \frac{2.1 \cdot 10^{-6} \text{ m}^2/(\text{Vs})}{2 \cdot 0.002 \text{ Cm}^{-2}} = 5.25 \cdot 10^{-4} \frac{\text{m}^4}{\text{Js}}.
\tag{7.20}
$$

The threshold electric field E_0 in (7.10) does not contain a unique numerical value in the literature mentioned above. The following value of the threshold electric field and the corresponding threshold driving force are used,

$$E_0 = 10^5 \frac{\text{V}}{\text{m}} \qquad \Longrightarrow \qquad T_0 = 400 \frac{\text{J}}{\text{m}^3}. \qquad (7.21)$$

7.2.2 Movement of the domain wall

Special attention is given in this section to the effect of the applied external electric field on the microstructures at different locations in the macro specimen. The micro specimen in Figure 7.3(a) is used as the representative microstructure. This microstructure contains one $180°$-domain wall and the domains are vertically poled. A downward applied external electric field produces domain wall driving forces as shown in Figure 7.3(b). If the wall driving force exceeds the critical value, the interface will start moving in the direction of the wall driving force.

(a)   (b)
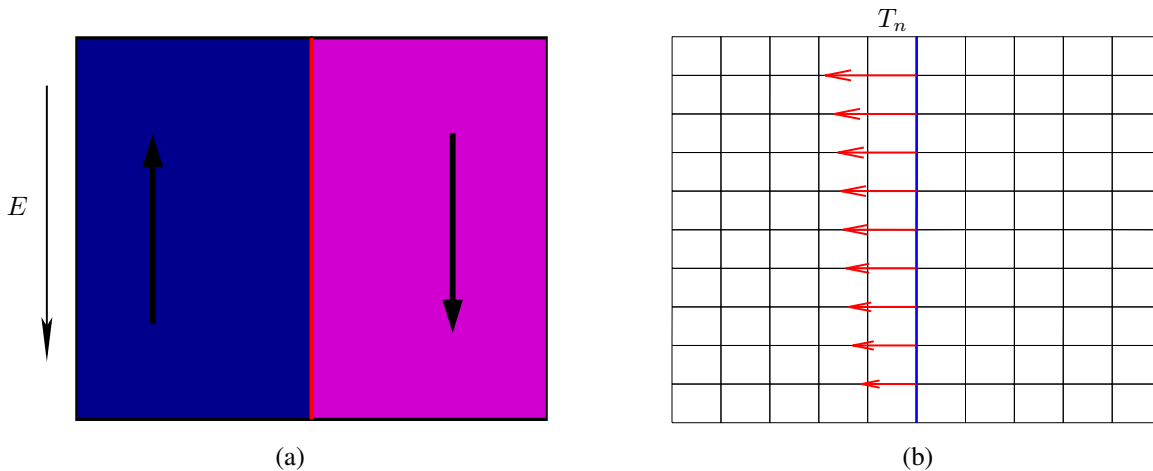
Figure 7.3: (a) *Microstructure used for homogenization*, (b) *microstructure with the nodal driving forces on the domain wall*

To obtain representative results of domain wall movement, two different locations on the macro specimen are chosen, see Figure 7.4. 'Location-2' is in the vicinity of the crack tip and 'Location-1' is in the vicinity of the boundary of the macro specimen. Now a downward external electric field is applied, and the intensity of the electric field is gradually increased. At each increment of the electric field, the configurational forces on the interface are determined with the help of FE^2-based computational homogenization.

The domain wall driving force has the same value as the configurational force, but it points to the opposite direction of the configurational force.
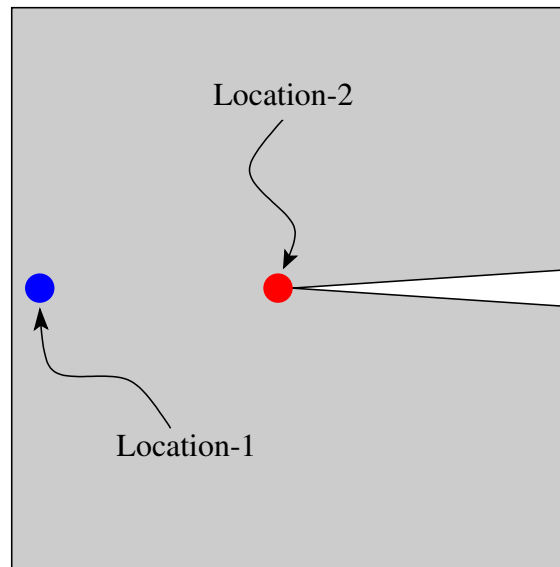
Figure 7.4: *Macro specimen*

Figure 7.5(a), 7.5(c), 7.5(e) and 7.5(g) show the evolution of the microstructure at 'Location-1' at different stages of the externally applied electric field, while Figure 7.5(b), 7.5(d), 7.5(f) and 7.5(h) show the evolution of the microstructure at 'Location-2'. In the initial configuration of both parts, the interfaces are located at the center of the microstructures, see Figure 7.5(a) and 7.5(b). Now the external electric field is increased gradually. When the intensity of the nominal electric field reaches the value of $10 \cdot 10^5$ V/m, the interface at 'Location-1' remains at its position, while the interface at 'Location-2' has already started to move to the left. This is due to the fact that at the crack tip region the electric field is intensified. When the value of the nominal electric field reaches $17.5 \cdot 10^5$ V/m, the microstructure in the vicinity of the crack tip in Figure 7.5(f) is approximately completely poled downward. On the other hand, the interface in Figure 7.5(e) has just started to move to the left. At the end of the application of $25 \cdot 10^5$ V/m nominal electric field, the microstructure at the 'Location-2' is completely poled downward and the microstructure at the 'Location-1' still is not fully poled downward. With these simulation results, it can also be concluded that the evolution of the microstructure varies with the location. In particular, near the crack tip domain switching initiates earlier and can be completed.

at 'Location-1'   at 'Location-2'

at $0.0 \frac{V}{m}$

(a)   (b)

at $10 \cdot 10^5 \frac{V}{m}$

(c)   (d)

at $17.5 \cdot 10^5 \frac{V}{m}$

(e)   (f)

at $25 \cdot 10^5 \frac{V}{m}$

(g)   (h)
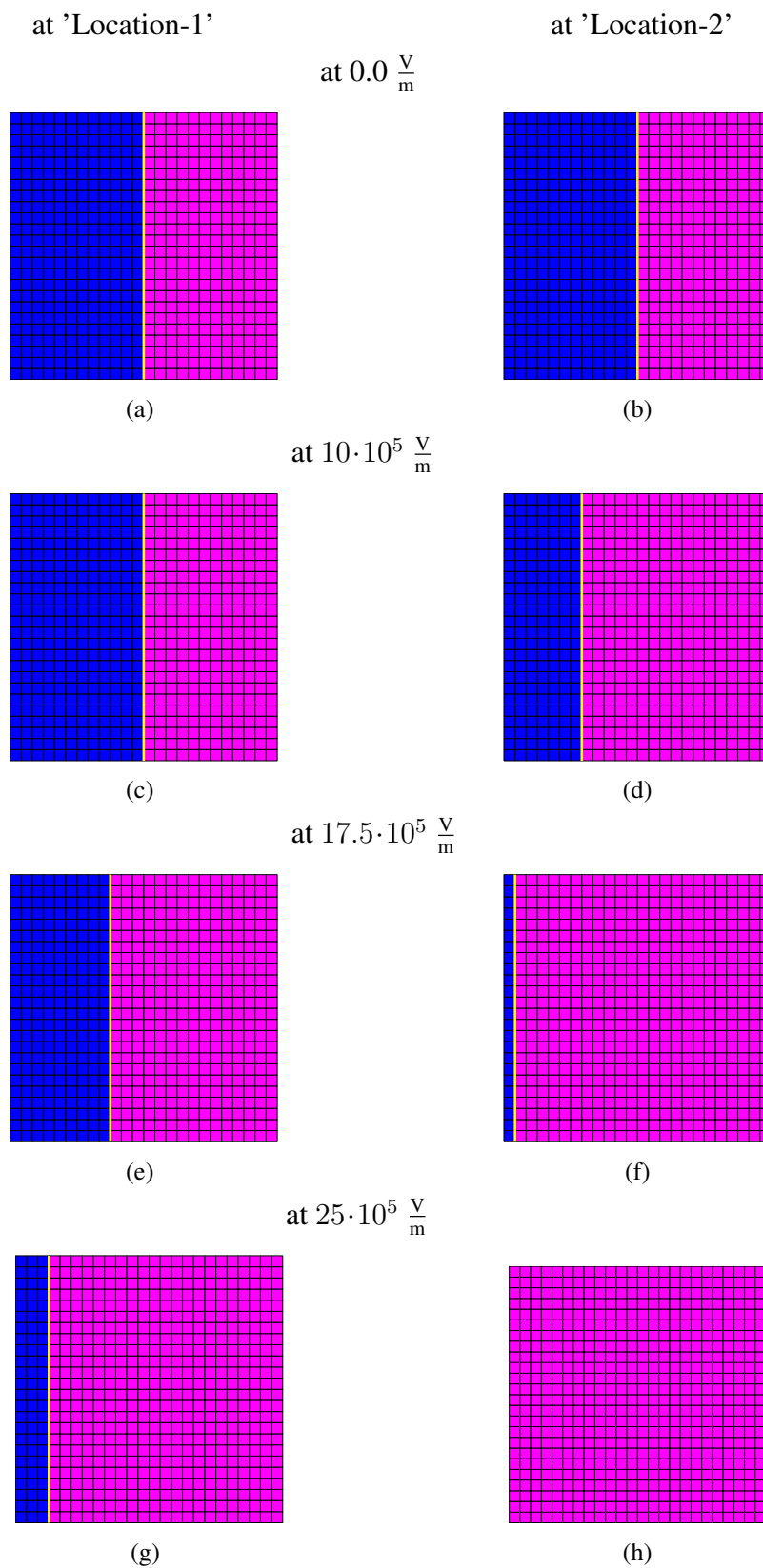
Figure 7.5: *Evolving microstructures at 'Location-1' and 'Location-2' at different nominal applied electric fields*

Previous results are only for two different locations in the macro specimen. Now we will demonstrate the microstructures in the entire macro specimen. Figure 7.6 shows the percentage of the left domain fraction at different intensity of the applied nominal electric field. The domain wall is initially at the center of the microstructure, and thus the domain fraction is 50%. If the fraction is 0.0%, it implies that the micro domain is fully poled downward. Since a downward nominal electric field is applied, the interfaces of the microstructures at every location on the macro specimen move to the left. As a result, the values of the left domain fraction are in the range from 0% to 50%.

at $0.0 \ \frac{\text{V}}{\text{m}}$ at $10\cdot10^5 \ \frac{\text{V}}{\text{m}}$

(a)   (b)

at $17.5\cdot10^5 \ \frac{\text{V}}{\text{m}}$ at $25\cdot10^5 \ \frac{\text{V}}{\text{m}}$

(c)   (d)

Figure 7.6: *Percentage of the left domain distribution on the macro specimen at different intensities of nominal electric field*

Figure 7.6(a) shows the left domain fraction distribution at the beginning of the application of the external electric field. The domain fraction values in the entire macro specimen are 50%. Figure 7.6(b) shows the left domain fraction distribution, when the external electric field has reached to $10 \cdot 10^5$ V/m. The left domain fraction at the crack tip region is smaller than 50%. This means that the interfaces of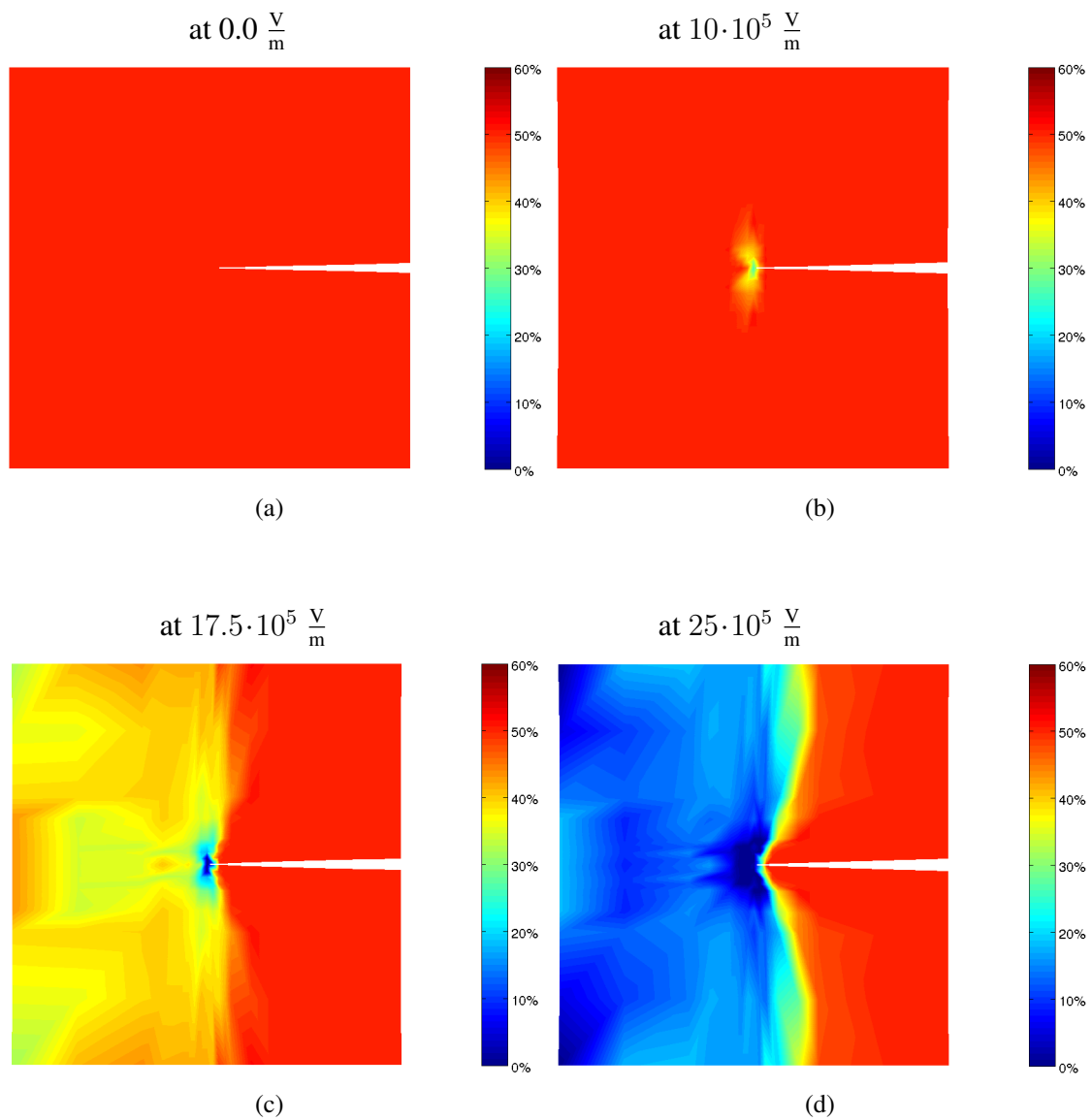 the microstructures at the crack tip vicinity have already started to move to the left. Figure 7.6(c) gives the left domain fraction distribution at the nominal electric field of $17.5 \cdot 10^5$ V/m.

The fraction values at the crack tip region reached approximately 0.0%, whereas in the left part of the macro specimen the values are smaller than 50%. It implies that the interfaces started moving towards the left in some other parts of the macro specimen. After the completion of the application of the nominal electric field of $25 \cdot 10^5$ V/m, one sees in Figure 7.6(d) that the distribution values on the left part of the macro specimen reach approximately 0.0%. This infers that the microstructures on the left part of the macro specimen are approximately poled downward as well. On the the other hand, the distribution values at the the regions above and below the macro crack still lie at 50%. This means that in these regions no movement of the interfaces is observed.

7.2.3   Comparison of the macro configurational forces for fixed and evolving microstructures

Figure 7.7(a) and 7.7(b) show the distribution of the magnitude of the homogenized electric displacement on the macro specimen for fixed and evolving microstructures, respectively. For the non-evolving microstructure, the macro electric displacement is more uniform than that for an evolving microstructure. It is evident that the electric displacement is directly related to the remanent polarization, see equation (4.9). In the case of the non-evolving microstructure, the interface is kept fixed at the center of the microstructures, and the consequence is that the homogenized remanent polarization always remains zero. For an evolving microstructure, the movement of the interface is allowed. As a result, the homogenized remanent polarizations may vary with the locations of the macro specimen.
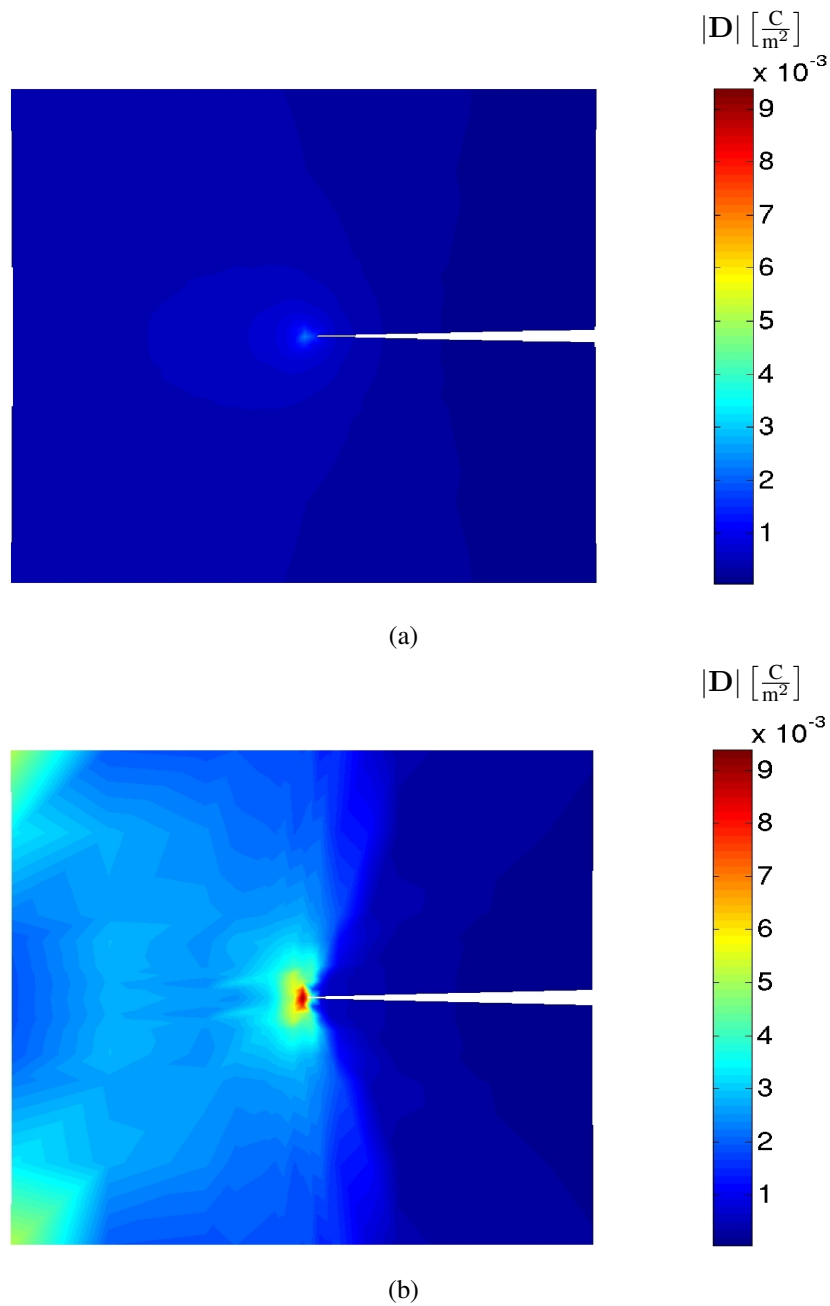
(a)

(b)

Figure 7.7: (a) *Electric displacement using fixed RVE*, (b) *Electric displacement using evolving RVE in macro specimen*

Figure 7.8 shows the comparison of the crack tip nodal configurational forces between the cases using non-evolving and evolving microstructures. A smaller value of configurational forces is observed for evolving microstructures in Figure 7.8. When the movement
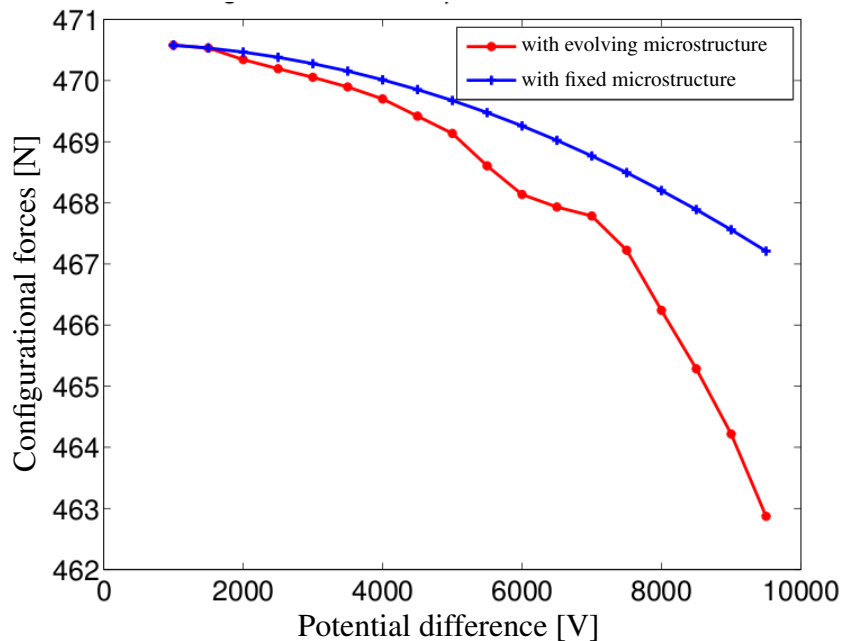
Figure 7.8: *Comparison of the configurational forces at the crack tip*

of the interface is allowed, the energy dissipates. Thus, a smaller value of configurational forces is found at the crack tip.

7.2.4   Dielectric hysteresis on the macro level

With the help of the computational homogenization along with the configurational force theory, it is possible to construct the hysteresis of the electric displacement vs. the electric field on the macro level. In this simulation a homogenization technique is applied to the electro-mechanically coupled problem by considering a varying external electric field with time. In the following results involving the homogenized electrical quantities are presented. For this simulation a homogeneous macro specimen, which contains no macro discontinuities, is used. For the simplicity of the computation, a microstructure with a vertical $180°$-domain wall is considered. These simulation results are calculated for a bipolar electrical loading in the vertical direction. Thereby no mechanical loading is considered.

The plot in Figure 7.9 shows the history of the applied electric field. The application of the external electric field begins with a value of 0.0 V/m, then the intensity of the electric field is gradually increased up to $1.9 \cdot 10^5$ V/m at point D. Afterwards the intensity of the

electric field is gradually decreased. At one point the external electric field reaches the value 0.0 V/m. Then a downward electric field is gradually applied and the intensity of the external electric field reaches the value $-6.5 \cdot 10^5$ V/m at point G. Now the intensity of the downward electric field is decreased and reaches the value 0.0 V/m. Afterwards the electric field is gradually increased to $5.25 \cdot 10^5$ V/m at point I.
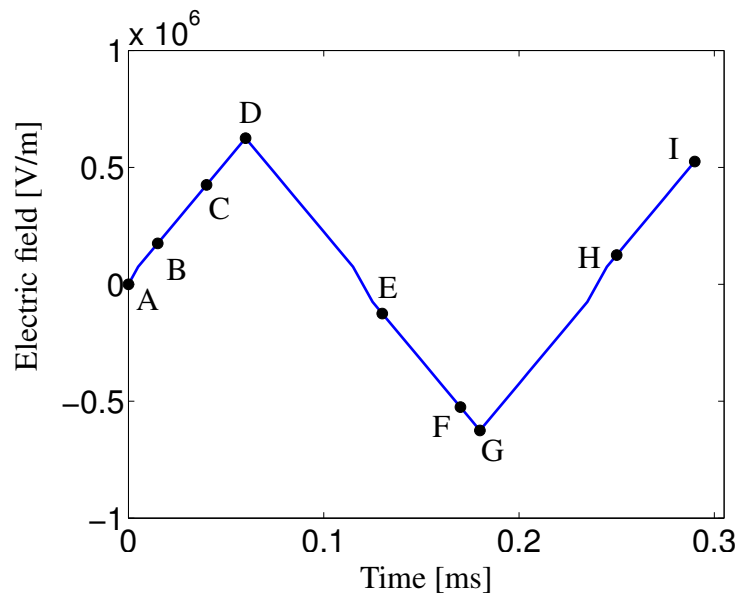
Figure 7.9: *Nominal electric field vs. time on the macro level*

Figure 7.10 shows a plot of the homogenized electric displacement vs. time along with the evolving microstructures for different time intervals. The homogenized electric displacements are determined with the application of the varying external electric field as stated in Figure 7.9. Figure 7.11 shows the plot of the homogenized electric displacement vs. nominal electric field. In particular, the time parts A to I are highlighted in the figures.

At the beginning of the application of the external electric field, the homogenized polarization is 0.0 C/m^2, since the domain wall divides the microstructure equally. As a result of a trivial electric field and homogenized polarization, the homogenized electric displacement is 0.0 C/m^2. Now the external electric field is gradually increased. The domain wall does not move until the value of the external electric field reaches $1.9 \cdot 10^5$ V/m. Within the range from point A to point B in Figure 7.11, the changes in homogenized electric displacements are very small.
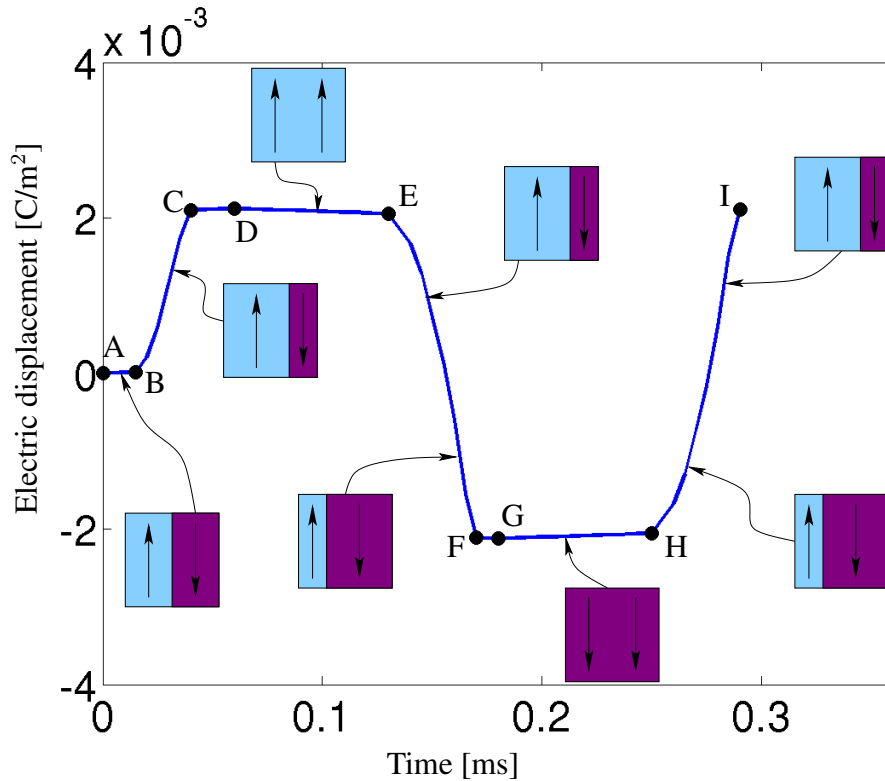
Figure 7.10: *Electric displacement vs. time on the macro level*

By increasing the intensity of the external electric field beyond $1.9 \cdot 10^5$ V/m at point B in Figure 7.11, the domain wall starts moving. At this point the homogenized polarization has a positive value. As the electric displacement and the remanent polarization are directly related to each other, the change in homogenized electric displacement is larger than that in the range of A-B. When the value of the external electric field reaches to $4.25 \cdot 10^5$ V/m at point C, the microstructure is completely poled upward. This implies that the piezoelectric material is microscopically saturated, and the homogenized electric displacement is $2.1 \cdot 10^{-3}$ C/m^2. Further incrementation of the electric field intensity (point D) changes the homogenized electric displacement linearly.

Likewise, the domain wall does not start moving in the other direction until the electric field reaches the value $-1.75 \cdot 10^5$ V/m at point E. From point D to point E, it is noticed that the changes in the electric displacements are very small. With the application of a larger downward electric field than that of point E, the domain wall starts moving in the opposite direction. As a result of the movement of the interface, the values of the electric displacements change rapidly. This situation is seen in the range from point E to point F in

the plot in Figure 7.11. At point F the micro domain is completely poled downward, and the applied electric field and the homogenized electric displacement are $-5.75 \cdot 10^5$ V/m and $-2.1 \cdot 10^{-3}$ C/m^2, respectively. Further incrementation of the value of the downward applied electric field does not change the homogenized electric displacement significantly, as the microstructure is fully poled downward.

Then we start applying an upward electric field and increase its value gradually. Between point G and point H, there are very little changes in the electric displacements, as there are no changes in polarization in the microstructures. When the applied electric field is increased beyond the value $1.25 \cdot 10^5$ V/m at point H in Figure 7.11, the value of the homogenized electric displacement changes rapidly until it reaches the value $2.1 \cdot 10^{-3}$ C/m^2 at point I. In the range from point H to point I, this phenomenon is seen because the domain wall keeps moving as the applied electric field is increased. When it reaches point I, the microstructure is fully poled upward. Further incrementation of the applied electric field does not change the homogenized electric displacement by a significant amount.
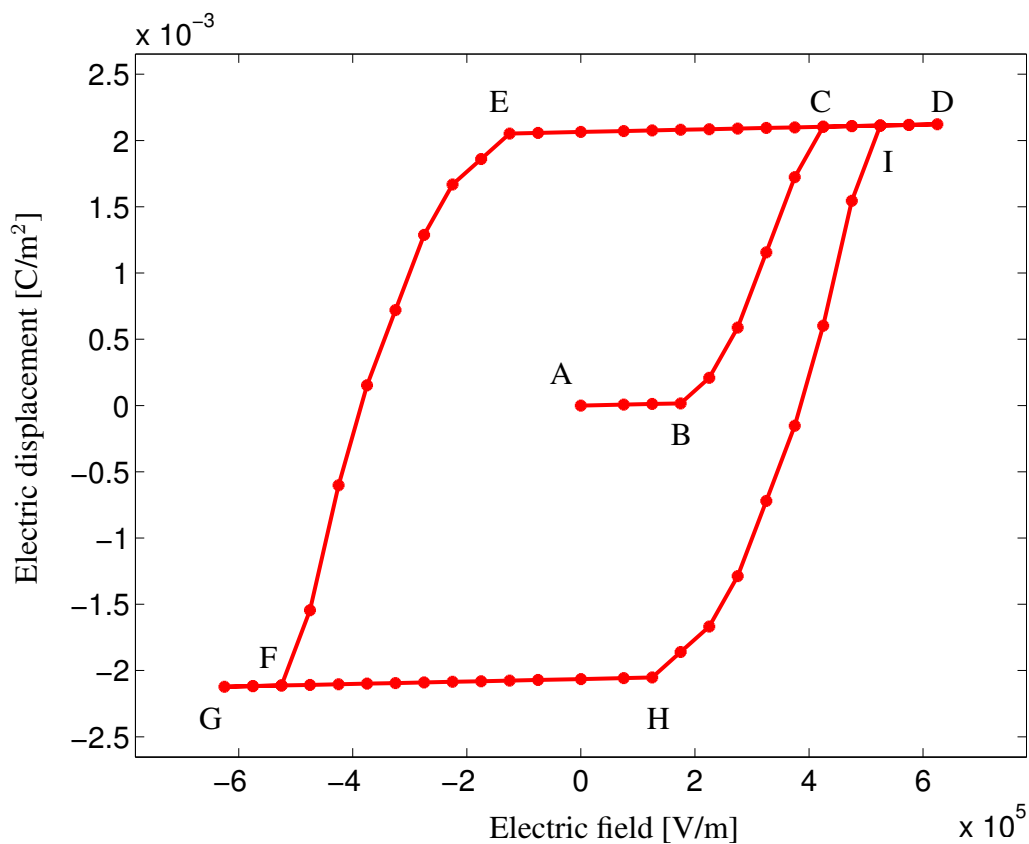
Figure 7.11: *Hysteresis loop (electric displacement vs. electric field) on the macro level*

In the ranges from A to B, from C to D, from D to E, from F to G, and from G to H in Figure 7.11, very small changes in the homogenized electric displacement are observed only due to the linear response of the dielectric effect in the material.

It should be noted that in the simulation the domain walls are not allowed to leave the microstructures during their movement in response of the applied electric field. After the domain is completely poled, the domain wall is kept at the element boundary.

The shape of the hysteresis loop is dependent on the time rate of the electric field. If the electric field is changed fast, the shape of the hysteresis loop is widened, in the other case it is narrowed.

Chapter 8

Conclusion

In this work a novel homogenization technique for piezoelectric materials is presented. Special attention is given to the homogenization of the electro-mechanical Eshelby stress tensor which is then used to determine the configurational forces at a crack tip on the macro level. A FE^2-based multiscale simulation technique is adopted to accomplish the homogenization of piezoelectric materials. In the FE^2-based homogenization, three different possible boundary conditions can be passed to the micro domain to solve the micro BVP of piezoelectric materials. If the simulation is carried out with the strain tensor based micro boundary conditions, a problem regarding the configurational force at the crack tip occurs. This approach does not provide a physically compatible configurational force at the crack tip. A thorough investigation is carried out to identify and solve the problem. It is found that this problem can be solved by using displacement gradient driven boundary conditions on the micro domain for the mechanical part of the homogenization process. A detailed description of boundary conditions based on displacement gradient is presented. If the micro problem is solved by strain based boundary conditions, unphysical volume configurational forces occur on the macro level. It is due to the exclusion of the rotational part of the deformation. The displacement gradient driven boundary conditions preserve the rotational part. For this reason it results in physically compatible configurational forces on the macro level.

For simplicity the Dirichlet boundary condition (displacement gradient driven BC for mechanical part) is used for the homogenization of piezoelectric materials. Multiscale simulations are carried out for both fixed and evolving microstructures. A macro specimen with a horizontal sharp crack has been simulated. To obtain the effect of the micro

inhomogeneities on the crack tip configurational force at macro level, simulations are performed with several types of microstructures containing different inhomogeneities. It is found from the simulation results that for both horizontal and vertical polarizations in the microstructure, a configurational force appears parallel to the crack ligament. A configurational force slightly inclined to the crack ligament is noticed in the case of an inclined polarization. When the mechanical load is along the polarization of the micro domain, a lower bound is found. The case with the mechanical displacement perpendicular to the polarization delivers an upper bound, because piezoelectric materials are stiffer in the transverse direction to the polar axis. If an electric field along with mechanical displacement is applied, the value of the configurational force reduces significantly for both positive and negative electric fields. But the amount of the reduction is different for different types of microstructures.

If an external electric field is applied to a piece of piezoelectric material, the interfaces may move. To capture this effect of the micro heterogeneities onto the crack tip configurational force, the evolution of the microstructures must be considered at the time of the application of the external electric field. A sharp interface model is used to treat the domain walls in piezoelectric materials, in which configurational forces are used to define the kinetics of the domain wall. A simple microstructure with a $180°$-domain wall is considered for the homogenization process. It can be concluded from these simulations that the microstructures in the crack tip region are the most affected microstructures. A comparison shows that the crack tip configurational force obtained by using evolving microstructures is smaller in value than that obtained by using fixed microstructures. In the case of evolving microstructures in piezoelectric materials, the total energy of the system is lowered by the motion of the interfaces of the material. As a result, a smaller configurational force is obtained in the case of evolving microstructures.

Simulations are carried out for the macro specimen featuring very simplified microstructures, which do not represent the real situation of the microstructures of piezoelectric materials. When the simulations are done with relatively complex microstructure including grains, the grain boundary is modeled as perfect interfaces for the sake of simplicity. An investigation of the configurational force at the crack tip are only performed for mode-I type crack. The homogenization process can be carried out in future for other types of boundary conditions assigned to the micro domains. Further modeling of grain boundaries in piezoelectric materials can be done, and multiscale simulations can be carried out for a piezoelectric specimen including other types of crack situations, e.g., mode-II, mode-III

cracks. In this work multiscale simulations are done using an evolving microstructure featuring the simplest structure with only one interface. Further investigations can be performed using more complex microstructures. In this case the biggest challenge will be the tracking of the interfaces in the microstructure. For a convenient tracking of the interfaces, the level set method may be used.

Appendix A

Appendix

A.1 Relations on a sharp interface

By defining the positive and negative interface limiting values of a scalar quantity a in the following way

$$
\begin{aligned}
a^+ &= \lim_{\epsilon \to 0} a(\mathbf{x}_{\mathcal{S}} + \epsilon \mathbf{n}_{\mathcal{S}}), \\
a^- &= \lim_{\epsilon \to 0} a(\mathbf{x}_{\mathcal{S}} - \epsilon \mathbf{n}_{\mathcal{S}}),
\end{aligned}
\tag{A.1}
$$

the jump $[\![a]\!]$ and average $\langle\!\langle a \rangle\!\rangle$ of a scalar quantity a can be written as

$$
\begin{aligned}
[\![a]\!] &= a^+ - a^-, \\
\langle\!\langle a \rangle\!\rangle &= \frac{1}{2}(a^+ + a^-).
\end{aligned}
\tag{A.2}
$$

The jump of a product is defined by

$$
[\![ab]\!] = [\![a]\!]\langle\!\langle b \rangle\!\rangle + \langle\!\langle a \rangle\!\rangle[\![b]\!].
\tag{A.3}
$$

According to the Lemma of Hadamard, the jump of a continuous scalar quantity a in the gradient at the singular surface $\mathcal{S}$ can only be in the normal direction to the surface:

$$
[\![a]\!] = 0 \quad \to \quad [\![\nabla a]\!] \cdot \mathbf{m}_\gamma = 0.
\tag{A.4}
$$

Using the Lemma we can, for example, calculate the rate of the jump for the continuous electric potential φ

$$\frac{\mathrm{d}}{\mathrm{d}t}[\![\varphi]\!] = [\![\nabla\varphi \cdot \mathbf{v}]\!] + [\![\frac{\partial\varphi}{\partial t}]\!] = 0, \tag{A.5}$$

which gives

$$[\![\dot\varphi]\!] = -[\![\nabla\varphi \cdot \mathbf{v}]\!] = -[\![\nabla\varphi]\!] \cdot \mathbf{v} \tag{A.6}$$
$$= -[\![\nabla\varphi]\!] \cdot (\mathbf{n}_{\mathcal{S}} v_n + \mathbf{m}_\gamma v^\gamma) \tag{A.7}$$
$$= -[\![\nabla\varphi]\!] \cdot \mathbf{n}_{\mathcal{S}} v_n, \tag{A.8}$$

where $\mathbf{v}$ is the velocity of the domain wall and $\mathbf{m}_\gamma$ are the tangent vectors to the Gaussian parametrization ξ^γ of the interface $\mathcal{S}$. Similarly, one obtains for the displacement $\mathbf{u}$:

$$[\![\dot{\mathbf{u}}]\!] = -[\![\nabla\mathbf{u}]\!]\mathbf{n}_{\mathcal{S}} v_n. \tag{A.9}$$

A.2 Voigt-notation

It is observed that symmetric tensors are used to denote many physical quantities. By using the Voigt-notation, the symmetry of tensor can be exploited in order to convert second order tensors (e.g., Cauchy stress tensor) to vectors and forth order tensors to square matrices (e.g., elasticity tensor). Commonly, the quantities in Voigt-notation are expressed with under-bar. The Voigt-notations are frequently seen in continuum mechanics.

A symmetric second order tensor, e.g., the Cauchy stress tensor $\boldsymbol{\sigma}$ in three dimension, can be formulated to a vector ($\underline{\boldsymbol{\sigma}}$ in Voigt-notation) as

$$\boldsymbol{\sigma} = \begin{pmatrix} \sigma_{11} & \sigma_{12} & \sigma_{13} \\ \sigma_{21} & \sigma_{22} & \sigma_{23} \\ \sigma_{31} & \sigma_{32} & \sigma_{33} \end{pmatrix} \Rightarrow \begin{pmatrix} \sigma_{11} \\ \sigma_{22} \\ \sigma_{33} \\ \sigma_{23} \\ \sigma_{13} \\ \sigma_{12} \end{pmatrix} = \begin{pmatrix} \underline{\sigma}_1 \\ \underline{\sigma}_2 \\ \underline{\sigma}_3 \\ \underline{\sigma}_4 \\ \underline{\sigma}_5 \\ \underline{\sigma}_6 \end{pmatrix} = \underline{\boldsymbol{\sigma}}. \tag{A.10}$$

The Equivalency of the indices of tensor and Voigt-notation in (A.10) is as in the following:

Tensor notation	11	22	33	23 or 32	13 or 31	12 or 21
Voigt-notation	1	2	3	4	5	6

Using substitutions of indices, it enables us to express a symmetric second order tensor as a vector with six components. Similarly, a third order tensor can be replaced by a 3×6 matrix (by keeping the first index unchanged, e.g., $T_{123} = T_{14}$), and a fourth order tensor can be represented with a 6×6 matrix (by performing the operation on the first two, and later on the last two indices, e.g., $T_{1322} = T_{52}$). This is quite helpful because every tensor up to 4th order can be expressed by a single two-dimensional matrix. The procedure of Voigt-notation simplifies the maths and makes them convenient to denote. The representation with Voigt-notation is particularly very useful for the equations of elasticity, where $\sigma_{ij} = C_{ijkl}\varepsilon_{kl}$ $(i,j,k,l = 1 \text{ to } 3)$ or $\boldsymbol{\sigma} = \mathbb{C}\boldsymbol{\varepsilon}$ can be transformed to $\underline{\sigma}_i = \underline{C}_{ij}\underline{\varepsilon}_j$ $(i,j = 1 \text{ to } 6)$ or $\underline{\boldsymbol{\sigma}} = \underline{\mathbb{C}}\,\underline{\boldsymbol{\varepsilon}}$:

$$
\begin{bmatrix}
\underline{\sigma}_1 \\
\underline{\sigma}_2 \\
\underline{\sigma}_3 \\
\underline{\sigma}_4 \\
\underline{\sigma}_5 \\
\underline{\sigma}_6
\end{bmatrix}
=
\begin{bmatrix}
\underline{C}_{11} & \underline{C}_{12} & \underline{C}_{13} & \underline{C}_{14} & \underline{C}_{15} & \underline{C}_{16} \\
\underline{C}_{21} & \underline{C}_{22} & \underline{C}_{23} & \underline{C}_{24} & \underline{C}_{25} & \underline{C}_{26} \\
\underline{C}_{31} & \underline{C}_{32} & \underline{C}_{33} & \underline{C}_{34} & \underline{C}_{35} & \underline{C}_{36} \\
\underline{C}_{41} & \underline{C}_{42} & \underline{C}_{43} & \underline{C}_{44} & \underline{C}_{45} & \underline{C}_{46} \\
\underline{C}_{51} & \underline{C}_{52} & \underline{C}_{53} & \underline{C}_{54} & \underline{C}_{55} & \underline{C}_{56} \\
\underline{C}_{61} & \underline{C}_{62} & \underline{C}_{63} & \underline{C}_{64} & \underline{C}_{65} & \underline{C}_{66}
\end{bmatrix}
\begin{bmatrix}
\underline{\varepsilon}_1 \\
\underline{\varepsilon}_2 \\
\underline{\varepsilon}_3 \\
\underline{\varepsilon}_4 \\
\underline{\varepsilon}_5 \\
\underline{\varepsilon}_6
\end{bmatrix},
\qquad (A.11)
$$

where

$$
\boldsymbol{\varepsilon} =
\begin{pmatrix}
\varepsilon_{11} & \varepsilon_{12} & \varepsilon_{13} \\
\varepsilon_{21} & \varepsilon_{22} & \varepsilon_{23} \\
\varepsilon_{31} & \varepsilon_{32} & \varepsilon_{33}
\end{pmatrix}
\Rightarrow
\begin{pmatrix}
\varepsilon_{11} \\
\varepsilon_{22} \\
\varepsilon_{33} \\
2\varepsilon_{23} \\
2\varepsilon_{13} \\
2\varepsilon_{12}
\end{pmatrix}
=
\begin{pmatrix}
\underline{\varepsilon}_1 \\
\underline{\varepsilon}_2 \\
\underline{\varepsilon}_3 \\
\underline{\varepsilon}_4 \\
\underline{\varepsilon}_5 \\
\underline{\varepsilon}_6
\end{pmatrix}
= \underline{\boldsymbol{\varepsilon}}.
\qquad (A.12)
$$

A.3 Balance of the homogenized configurational forces

In this section an investigation is carried out for the balance of macro configurational forces. The homogenized Eshelby stress tensor is determined through volume averaging of the micro Eshelby stress tensor. The microstructure is deformed in two different ways which are demonstrated in the following.

A.3.1   Macro displacement gradient based deformation of the micro domain

The micro domain is deformed according to the macro displacement gradient for both types of boundary conditions (Dirichlet and periodic boundary conditions) on the domain. By taking divergence of both sides of (5.32), we get

$$\overline{\Sigma}_{ij,j} = \frac{1}{V}\int_{\mathcal{B}_{\text{mic}}} \Sigma_{ij,j}\, \mathrm{d}\Omega = \frac{1}{V}\int_{\partial\mathcal{B}_{\text{mic}}} \Sigma_{ij} n_j\, \mathrm{d}\Gamma \qquad \text{(using divergence theorem).} \qquad \text{(A.13)}$$

Inserting the definition of the Eshelby stress tensor in (A.13), the equation can be written as

$$
\begin{aligned}
\overline{\Sigma}_{ij,j} &= \frac{1}{V}\int_{\partial\mathcal{B}_{\text{mic}}} (W\delta_{ij} - u_{k,i}\sigma_{kj}) n_j\, \mathrm{d}\Gamma \\
&= \frac{1}{V}\int_{\partial\mathcal{B}_{\text{mic}}} \delta_{ij} W n_j\, \mathrm{d}\Gamma - \frac{1}{V}\int_{\partial\mathcal{B}_{\text{mic}}} u_{k,i}\sigma_{kj} n_j\, \mathrm{d}\Gamma.
\end{aligned} \qquad \text{(A.14)}
$$

Using the definition of the displacement gradient on the boundary of the micro domain from equation (5.19) , equation (A.14) can be written as

$$
\begin{aligned}
\overline{\Sigma}_{ij,j} &= \frac{1}{V}\int_{\mathcal{B}_{\text{mic}}} \delta_{ij} W_{,j}\, \mathrm{d}\Omega - \frac{1}{V}\int_{\partial\mathcal{B}_{\text{mic}}} (\overline{u}_{k,i} + \widetilde{w}_{k,i})\, \sigma_{kj} n_j\, \mathrm{d}\Gamma \\
&= \frac{1}{V}\int_{\mathcal{B}_{\text{mic}}} W_{,i}\, \mathrm{d}\Omega - \frac{1}{V}\int_{\partial\mathcal{B}_{\text{mic}}} \overline{u}_{k,i}\sigma_{kj} n_j\, \mathrm{d}\Gamma - \frac{1}{V}\int_{\partial\mathcal{B}_{\text{mic}}} \widetilde{w}_{k,i}\sigma_{kj} n_j\, \mathrm{d}\Gamma.
\end{aligned} \qquad \text{(A.15)}
$$

With the definition of boundary traction and using the divergence theorem, equation (A.15) can be written as

$$
\begin{aligned}
\overline{\Sigma}_{ij,j} &= \overline{W}_{,i} - \frac{1}{V}\int_{\mathcal{B}_{\text{mic}}} \left(\overline{u}_{k,i}\sigma_{kj}\right)_{,j}\, \mathrm{d}\Omega - \frac{1}{V}\int_{\partial\mathcal{B}_{\text{mic}}} \widetilde{w}_{k,i} t_k\, \mathrm{d}\Gamma \\
&= \overline{W}_{,i} - \frac{1}{V}\int_{\mathcal{B}_{\text{mic}}} \left(\overline{u}_{k,ij}\sigma_{kj} + \overline{u}_{k,i}\sigma_{kj,j}\right)\, \mathrm{d}\Omega - \frac{1}{V}\int_{\partial\mathcal{B}_{\text{mic}}} \widetilde{w}_{k,i} t_k\, \mathrm{d}\Gamma \\
&= \overline{W}_{,i} - \frac{1}{V}\int_{\mathcal{B}_{\text{mic}}} \overline{u}_{k,ij}\sigma_{kj}\, \mathrm{d}\Omega - \frac{1}{V}\int_{\partial\mathcal{B}_{\text{mic}}} \widetilde{w}_{k,i} t_k\, \mathrm{d}\Gamma \qquad (\text{as } \sigma_{kj,j} = 0).
\end{aligned} \qquad \text{(A.16)}
$$

For periodic boundary conditions on the micro domain, it can be written that $\int_{\partial\mathcal{B}_{\text{mic}}} \widetilde{w}_{k,i} t_k\, \mathrm{d}\Gamma = 0$, as $\widetilde{w}_{k,i}^{+} = \widetilde{w}_{k,i}^{-}$ and $t_k^{+} = -t_k^{-}$ on opposite faces of the micro domain. The fluctua-

tion term $\widetilde{w}$ vanishes for a Dirichlet boundary condition on the micro domain. Equation (A.16) can be written as

$$
\begin{aligned}
\overline{\Sigma}_{ij,j} &= \overline{W}_{,i} - \overline{u}_{k,ij} \frac{1}{V} \int_{\mathcal{B}_{\mathrm{mic}}} \sigma_{kj} \, \mathrm{d}\Omega \\
&= \overline{W}_{,i} - \overline{u}_{k,ij} \overline{\sigma}_{kj}.
\end{aligned}
\tag{A.17}
$$

As $\overline{W}_{,i} - \overline{u}_{k,ij} \overline{\sigma}_{kj} = \overline{g}_i$ (where $\overline{g}_i$ is the macro volume configurational force), the material is macroscopically homogeneous, and there are no body forces in the material, there will be no macro volume configurational force in the material. Thus, equation (A.17) or the balance of homogenized configurational forces can be stated as

$$
\overline{\Sigma}_{ij,j} = \overline{g}_i = 0.
$$

In this case no unphysical volume configurational forces are produced on the macro level due to the homogenization of the material.

A.3.2 Macro strain based deformation of the micro domain

In this section the micro domain is deformed according to the macro strain in both type of boundary conditions (Dirichlet and periodic boundary conditions). So, in this case the balance of the macro configurational forces in (A.16) can written as

$$
\begin{aligned}
\overline{\Sigma}_{ij,j} &= \frac{1}{V} \int_{\mathcal{B}_{\mathrm{mic}}} \delta_{ij} W_{,j} \, \mathrm{d}\Omega - \frac{1}{V} \int_{\partial\mathcal{B}_{\mathrm{mic}}} (\overline{\varepsilon}_{ki} + \widetilde{w}_{k,i}) \sigma_{kj} n_j \, \mathrm{d}\Gamma \\
&= \frac{1}{V} \int_{\mathcal{B}_{\mathrm{mic}}} \delta_{ij} W_{,j} \, \mathrm{d}\Omega - \frac{1}{V} \int_{\partial\mathcal{B}_{\mathrm{mic}}} (\overline{u}_{k,i} - \overline{\omega}_{ki} + \widetilde{w}_{k,i}) \sigma_{kj} n_j \, \mathrm{d}\Gamma \\
&= \frac{1}{V} \int_{\mathcal{B}_{\mathrm{mic}}} W_{,i} \, \mathrm{d}\Omega - \frac{1}{V} \int_{\partial\mathcal{B}_{\mathrm{mic}}} \overline{u}_{k,i} \sigma_{kj} n_j \, \mathrm{d}\Gamma \\
&\quad - \frac{1}{V} \int_{\partial\mathcal{B}_{\mathrm{mic}}} \widetilde{w}_{k,i} \sigma_{kj} n_j \, \mathrm{d}\Gamma + \frac{1}{V} \int_{\partial\mathcal{B}_{\mathrm{mic}}} \overline{\omega}_{ki} \sigma_{kj} n_j \, \mathrm{d}\Gamma.
\end{aligned}
\tag{A.18}
$$

The first three terms in (A.18) are similar as in the previous section and they will vanish in the formulation. Thus, equation (A.18) can be written as

$$
\overline{\Sigma}_{ij,j} = \frac{1}{V} \int_{\partial\mathcal{B}_{\mathrm{mic}}} \overline{\omega}_{ki} \sigma_{kj} n_j \, \mathrm{d}\Gamma = \frac{1}{V} \int_{\mathcal{B}_{\mathrm{mic}}} (\overline{\omega}_{ki} \sigma_{kj})_{,j} \, \mathrm{d}\Omega = \frac{1}{V} \int_{\mathcal{B}_{\mathrm{mic}}} (\overline{\omega}_{ki,j} \sigma_{kj} + \overline{\omega}_{ki} \sigma_{kj,j}) \, \mathrm{d}\Omega
$$

$$= \overline{\omega}_{ki,j} \frac{1}{V} \int_{\mathcal{B}_{\mathrm{mic}}} \sigma_{kj} \, \mathrm{d}\Omega = \overline{\omega}_{ki,j} \overline{\sigma}_{kj}. \tag{A.19}$$

So, the balance of the macro configurational forces can be written as

$$\overline{\Sigma}_{ij,j} = \overline{\omega}_{ki,j} \overline{\sigma}_{kj}.$$

Although the material is macroscopically homogeneous and there is no macroscopic body force in the material, the balance of the macro configurational forces produces some unphysical volume configurational forces. The amount of the unphysical volume configurational forces is $-\overline{\omega}_{ki,j} \overline{\sigma}_{kj}$.

A.4   Domain wall driving force

A.4.1   On a 180°-domain wall

The driving force acting on a 180°-domain wall is approximated as illustrated in the following. The geometry sketched in Figure 7.3(a) is considered for the formulations.

By inserting the Eshelby stress tensor of (7.2) into the domain wall driving force (first equation in (7.5)); and assuming that there is no free charge on the domain wall ($[\![\mathbf{D}]\!] \cdot \mathbf{n}_\mathcal{S} = 0$, where $\mathbf{n}_\mathcal{S}$ is the normal vector to the domain wall); and considering the mechanical equilibrium condition on the domain wall ($[\![\boldsymbol{\sigma}]\!]\mathbf{n}_\mathcal{S} = \mathbf{0}$) , the wall driving can be formulated as

$$\tau_n = [\![H]\!] - \mathbf{n}_\mathcal{S} \cdot \left([\![(\nabla\mathbf{u})^T \boldsymbol{\sigma}]\!]\mathbf{n}_\mathcal{S} \right) + \mathbf{n}_\mathcal{S} \cdot ([\![\mathbf{E} \otimes \mathbf{D}]\!]\mathbf{n}_\mathcal{S}) \tag{A.20}$$

$$= \frac{1}{2}[\![(\boldsymbol{\varepsilon} - \boldsymbol{\varepsilon}_0) \cdot [\mathbb{C}(\boldsymbol{\varepsilon} - \boldsymbol{\varepsilon}_0)]]\!] - [\![(\boldsymbol{\varepsilon} - \boldsymbol{\varepsilon}_0) \cdot (\mathbb{b}^T \mathbf{E})]\!]$$

$$- \frac{1}{2}[\![\mathbf{E} \cdot (\mathbf{A}\mathbf{E})]\!] - [\![\mathbf{P}^0 \cdot \mathbf{E}]\!] - \mathbf{n}_\mathcal{S} \cdot \left([\![(\nabla\mathbf{u})^T]\!]\boldsymbol{\sigma} - [\![\mathbf{E}]\!] \otimes \mathbf{D} \right) \mathbf{n}_\mathcal{S}. \tag{A.21}$$

The material parameters in equations (7.18) and (7.19) imply that the electric field is not significantly stronger than approximately 1 MV/m, the terms in the first line of (A.21) and the first term in the second line of (A.21) can be assumed to be small compared to $[\![\mathbf{P}^0 \cdot \mathbf{E}]\!]$. The last term in (A.21) is neglected with the same arguments, because the jumps of $(\nabla\mathbf{u})^T$ and $\mathbf{E}$ in the normal direction of the domain wall are also small compared to

$\llbracket \mathbf{P}^0 \cdot \mathbf{E} \rrbracket$. By all the arguments and assumptions, the approximated driving force can be written as

$$
\begin{aligned}
\tau_n \;\approx\; \llbracket \mathbf{P}^0 {\cdot} \mathbf{E} \rrbracket = \mathbf{P}^{0+} {\cdot} \mathbf{E}^+ - \mathbf{P}^{0-} {\cdot} \mathbf{E}^- &= \begin{bmatrix} 0 \\ P^0 \end{bmatrix} \cdot \begin{bmatrix} 0 \\ E_2 \end{bmatrix} - \begin{bmatrix} 0 \\ -P^0 \end{bmatrix} \cdot \begin{bmatrix} 0 \\ E_2 \end{bmatrix} \\
&= P^0 E_2 + P^0 E_2 = 2P^0 E_2.
\end{aligned}
$$

A.4.2   On a 90°-domain wall

Similar arguments and assumptions can be stated for a 90°-domain wall of piezoelectric materials. This leads to the approximated driving force on a 90°-domain wall

$$
\begin{aligned}
\tau_n \;\approx\; \llbracket \mathbf{P}^0 \cdot \mathbf{E} \rrbracket = \mathbf{P}^{0+} {\cdot} \mathbf{E}^+ - \mathbf{P}^{0-} {\cdot} \mathbf{E}^- &= \begin{bmatrix} P_1^0 \\ P_2^0 \end{bmatrix} \cdot \begin{bmatrix} 0 \\ E_2 \end{bmatrix} - \begin{bmatrix} P_1^0 \\ -P_2^0 \end{bmatrix} \cdot \begin{bmatrix} 0 \\ E_2 \end{bmatrix} \\
&= P_2^0 E_2 + P_2^0 E_2 = 2P_2^0 E_2.
\end{aligned}
$$

Bibliography

[1] R. Ahluwalia and W. Cao. Effect of surface induced nucleation of ferroelastic domains on polarization switching in constrained ferroelectrics. *J. Appl. Phys.*, 93(1):537–544, 2003.

[2] R. Ahluwalia, T. Lookman, A. Saxena, and W. Cao. Domain-size dependence of piezoelectric properties of ferroelectrics. *Phys. Rev. B*, 72(1):014112, 2005.

[3] H. Allik and T. J. R. Hughes. Finite element method for piezoelectric vibration. *Int. J. Numer. Meth. Eng.*, 2(2):151–157, 1970.

[4] G. Bao, J. W. Hutchinson, and R. M. McMeeking. Particle reinforcement of ductile matrices against plastic flow and creep. *Acta Metall. Mater.*, 39(8):1871–1882, 1991.

[5] A. Bensoussan, J.-L. Lions, and G. Papanicolau. Asymptotic analysis for periodic structures. Studies in Mathematics and its Application, North-Holland, Amsterdam, 1978.

[6] Y. Benveniste. A new approach to the application of Mori-Tanaka's theory in composite materials. *MM*, 6:147–157, 1987.

[7] J. Betten. *Kontinuumsmechanik*. Springer, Berlin, Heidelberg, New York, Barcelons, Hong Kong, London, Milan, Paris, Singapore, Tokyo, 2001.

[8] M. Braun. Configurational forces induced by finite-element discretization. *Proc. Estonian Acad. Sci. Phys. Math.*, 46(1/2):24–31, 1997.

[9] W. Cao and G. R. Barsch. Landau-Ginzburg model of interphase boundaries in improper ferroelastic Perovskites of D_{4h}^{18} symmetry. *Phys. Rev. B*, 41(7):4334–4348, 1990.

[10] S. Choudhury, Y. L. Li, C. E. Krill III, and L.-Q. Chen. Phase-field simulation of polarization switching and domain evolution in ferroelectric polycrystals. *Acta Mater.*, 53(20):5313–5321, 2005.

[11] S. Choudhury, Y. L. Li, C. E. Krill III, and L.-Q. Chen. Effect of grain orientation and grain size on ferroelectric domain switching and evolution: phase field simulations. *Acta Mater.*, 55(4):1415–1426, 2007.

[12] T. Christman, A. Needleman, and S. Suresh. An experimental and numerical study of deformation in metal-ceramic composites. *Acta Metall.*, 37(11):3029–3050, 1989.

[13] F. Devries, H. Dumontet, G. Duvaut, and F. Lene. Homogenization and damage for composite structures. *Int. J. Numer. Meth. Eng.*, 27:285–298, 1989.

[14] J. D. Eshelby. The force on an elsatic singularity. *Phil. Trans. Roy. Soc. London A*, 244:87–112, 1951.

[15] J. D. Eshelby. The determination of the elastic field of an ellipsoidal inclusion, and related problems. *Proc. Roy. Soc. London A*, 241:376–396, 1957.

[16] J. D. Eshelby. Energy relations and the energy-momentum tensor in continumm mechanics. *in Kanninen*, pages 77–115, 1970.

[17] F. Feyel. Multiscale FE^2 elastoviscoplastic analysis of composite structures. *Comput. Mater. Sci.*, 16:344–354, 1999.

[18] F. Feyel. A multilevel finite element method (FE^2) to describe the response of highly non-linear structures using generalized continua. *Comput. Meth. Appl. Mech. Eng.*, 192:3233–3244, 2003.

[19] F. Feyel and J.-L. Chaboche. FE^2 multiscale approach for modelling the elastoviscoplastic behaviour of long fiber SiC/Ti composite materials. *Comput. Meth. Appl. Mech. Eng.*, 183:309–330, 2000.

[20] J. Fish, Q. Yu, and K.-L. Shek. Computational damage mechanics for composite materials based on mathematical homogenization. *Int. J. Numer. Meth. Eng.*, 45:1657–1679, 1999.

[21] R. B. Flippen. Domain wall dynamics in ferroelectric/ferroelastic molybdates. *J. Appl. Phys.*, 46(3):1068–1071, 1975.

[22] P. A. Fotiu and S. Nemat-Nasser. Overall properties of elastic-viscoplastic periodic composites. *Int. J. Plast.*, 12:163–190, 1996.

[23] Y. C. Fung and P. Tong. *Classical and computational solid mechanics*. World Scientific, Singapore, New Jersey, London, Hong Kong, 2001.

[24] M. G. D. Geers, V. G. Kouznetsova, and W. A. M. Brekelmans. Multi-scale computational homogenization: Trends and challenges. *J. Comput. Appl. Math.*, 234:2175–2182, 2010.

[25] S. Ghosh, K. Lee, and S. Moorthy. Multiple scale analysis of heterogeneous elastic structures using homogenization theory and Voronoi cell finite element method. *Int. J. Sol. Struc.*, 32(1):27–62, 1995.

[26] S. Ghosh, K. Lee, and S. Moorthy. Two scale analysis of heterogeneous elastic-plastic materials with asymptotic homogenization and Voronoi cell finite element model. *Comput. Meth. Appl. Mech. Eng.*, 132, 1996.

[27] S. Ghosh, K. Lee, and S. Moorthy. A multi-level computational model for multi-scale damage analysis in composite and porous materials. *Int. J. Sol. Struc.*, 38, 2001.

[28] O. Goy. *Point defects in piezoelectric materials – continuum mechanical modelling and numerical simulation*. PhD thesis, Technische Universität Kaiserslautern, Kaiserslautern, 2010.

[29] D. Gross and T. Seelig. *Bruchmechanik: Mit einer Einführung in die Mikromechanik*. Springer, Berlin, 2007.

[30] J. M. Guedes and N. Kikuchi. Preprocessing and postprocessing for materials based on the homogenization method with adaptive finite element methods. *Comput. Meth. Appl. Mech. Eng.*, 83:143–198, 1990.

[31] M. E. Gurtin. *An introduction to continuum mechanics*. Academic Press, New York, London, Toronto, Sydney, San Francisco, 1981.

[32] M. E. Gurtin. *Configurational forces as basic concepts of continuum physics*. Springer, New York, Berlin, Heidelberg, 2000.

[33] Z. Hashin. The elastic moduli of heterogeneous materials. *J. Appl. Mech.*, 29:143–150, 1962.

[34] Z. Hashin. Analysis of composite materials - a survey. *J. Appl. Mech.*, 50:481–505, 1983.

[35] Z. Hashin and A. Shtrikman. A variational approach to the theory of the elastic behaviour of polycristals. *J. Mech. Phys. Solid.*, 10:343–352, 1962.

[36] Z. Hashin and A. Shtrikman. On some variational principles in anisotropic and nonhomogeneous elasticity. *J. Mech. Phys. Solid.*, 10:335–342, 1962.

[37] Z. Hashin and A. Shtrikman. A variational approach to the theory of the elastic behaviour of multiphase materials. *J. Mech. Phys. Solid.*, 11:127–140, 1963.

[38] P. Haupt. *Continuum mechanics and theory of materials*. Springer, Heidelberg, New York, Barcelona, Hong Kong, London, Milan, Paris, Singapure, Tokyo, 2000.

[39] R. Hill. A self-consistent mechanics of composite materials. *J. Mech. Phys. Solid.*, 13:213–222, 1965.

[40] G. A. Holzapfel. *Nonlinear solid mechanics: a continuum approach for engineering*. John Wiley & Sons, Chichester, 2001.

[41] T. J. R. Hughes. *The finite element method*. Prentice Hall, Englewood Cliffs, 1987.

[42] J. D. Jackson. *Classical electrodynamics, 3rd edition*. John Wiley & Sons, Inc., New York, 1999.

[43] P. Kanouté, D. P. Boso, J. L. Chaboche, and B. A. Schrefler. Multiscale methods for composites: a review. *Arch. Comput. Meth. Eng.*, 16:31–75, 2009.

[44] M.-A. Keip and J. Schröder. Effective electromechanical properties of heterogeneous piezoelectrics. *Advances in Extended and Multifield Theories for Continua, Lecture Notes in Applied and Computational Mechanics*, 59:109–128, 2011.

[45] H. Kessler and H. Balke. A continuum analysis of charge induced ferroelectric domain wall motions. *J. Mech. Phys. Solids*, 54(1):86–112, 2006.

[46] H. Kessler and H. Balke. A continuum analysis of the driving forces of ferroelectric/ferroelastic domain wall motions. *J. Mech. Phys. Solids*, 54(1):113–127, 2006.

[47] M. Khalaquzzaman, B. X. Xu, S. Ricker, and R. Müller. Computational homogenization of piezoelectric materials using FE^2 to determine configurational forces. *Technische Mechanik*, 32(1):21–37, 2012.

[48] R. Kienzler and G. Herrmann. *Mechanics in material space*. Springer, New York, Berlin, Heidelberg, 2000.

[49] V. Kouznetsova, W. A. M. Brekelmans, and F. P. T. Baaijens. An approach to micro-macro modeling of heterogeneous materials. *Comput. Mech.*, 27:37–48, 2001.

[50] E. Kröner. Berechnung der elastichen Konstanten des Vielkristalls aus den Konstanten des Einkristalls. *Z. Phys.*, 151:504–518, 1958.

[51] L. D. Landau and E. M. Lifshitz. *The classical theory of fields, vol. 2 of course of theoretical physics, 4th edition*. Butterworth-Heinemann, Amsterdam, Boston, Heidelberg, 1980.

[52] L. D. Landau and E. M. Lifshitz. *Electrodynamics of continuous media, vol. 8 of course of theoretical physics, 2nd edition*. Butterworth-Heinemann, Amsterdam, Boston, Heidelberg, 1984.

[53] P. H. Leo and R. F. Sekerka. The effect of surface stress on crystal-melt and crystal-crystal equilibrium. *Acta Metall.*, 37(12):3119–3138, 1989.

[54] Z. Li, C. Wang, and C. Chen. Effective electromechanical properties of transversely isotropic piezoelectric ceramics with microvoids. *Comput. Mater. Sci.*, 27:381–392, 2003.

[55] I.-S. Liu. *Continuum mechanics*. Springer, Berlin, Heidelberg, New York, Barcelons, Hong Kong, London, Milan, Paris, Singapore, Tokyo, 2002.

[56] R. E. Loge and Z. Suo. Nonequilibrium thermodynamics of ferroelectric domain evolution. *Acta Mater.*, 44(8):3429–3438, 1996.

[57] J. E. Marsden and T. J.R. Hughes. *Mathematical foundations of elasticity*. Devor, Mineola, New York, 1983.

[58] G. A. Maugin. *Configurational forces: thermomechanics, physics, mathematics, and numerics*. Chapman & Hall/CRC, London, Glasgow, New York, Tokyo, Melbourne, Madras, 2010.

[59] P. E. McHugh, R. J. Asaro, and C. F. Shih. Computational modeling of metal matrix composite materials - II. isothermal stress-strain behaviour. *Acta Metall. Mater.*, 41(5):1477–1488, 1993.

[60] R. McMeeking and A. Ricoeur. The weight function for cracks in piezoelectrics. *Int. J. Solid Struc.*, 40:6143–6162, 2003.

[61] V. Mehling. *Phenomenological modeling of ferroelectric material behavior*. PhD thesis, Technische Universität Darmstadt, Darmstadt, 2007.

[62] J. C. Michel, H. Moulinec, and P. Suquet. Effective properties of composite materials with periodic microstructure: a computational approach. *Comput. Meth. Appl. Mech. Eng.*, 172:109–143, 1999.

[63] C. Miehe. Strain-driven homogenization of inelastic microstructures and composites based on an incremental variational formulation. *Int. J. Numer. Meth. Eng.*, 55:1285–1322, 2002.

[64] C. Miehe. Computational micro-to-macro transitions for discretized microstructures of heterogeneous materials at finite strains based on the minimization of averaged incremental energy. *Comput. Meth. Appl. Mech. Eng.*, 192:559–591, 2003.

[65] C. Miehe and A. Koch. Computational micro-to-macro transitions of discretized microstructures undergoing small strains. *Arch. Appl. Mech.*, 72:300–317, 2002.

[66] C. Miehe, J. Schotte, and J. Schröder. Computational micro-macro transitions and overall moduli in the analysis of polycrystals at large strains. *Comput. Mater. Sci.*, 16:372–382, 1999.

[67] C. Miehe, J. Schröder, and J. Schotte. Computational homogenization analysis in finite plasticity. Simulation of texture development polycrystalline materials. *Comput. Meth. Appl. Mech. Eng.*, 171:387–418, 1999.

[68] T. Mori and K. Tanaka. Average stress in matrix and average elastic energy of materials with misfitting inclusions. *Acta Metall.*, 21:571–574, 1973.

[69] H. Moulinec and P. Suquet. A numerical method for computing the overall response of nonlinear composites with complex microstructure. *Comput. Meth. Appl. Mech. Eng.*, 157:69–94, 1998.

[70] R. Müller and D. Gross. 3D simulation of equilibrium morphologies of precipitates. *Comput. Mater. Sci.*, 11:35–44, 1998.

[71] R. Müller and D. Gross. 3D inhomogeneous, misfitting second phage particles-equilibrium shapes and morphological development. *Comput. Mater. Sci.*, 16:53–60, 1999.

[72] R. Müller, D. Gross, and D. C. Lupascu. Driving forces on domain walls in ferroelectric materials and interaction with defects. *Comput. Mater. Sci.*, 35:42–52, 2006.

[73] R. Müller, S. Kolling, and G. A. Maugin. On configurational forces in the context of the finite element method. *Int. J. Numer. Meth. Eng.*, 53(7):1557–1575, 2002.

[74] R. Müller and G. A. Maugin. On material forces and finite element discretizations. *Comput. Mech.*, 29(1):52–60, 2002.

[75] T. Nakamura and S. Suresh. Effect of thermal residual stress and fiber packing on deformation of metal-matrix composites. *Acta Metall. Mater.*, 41(6):1665–1681, 1993.

[76] S. Nemat-Nasser and M. Hori. *Micromechanics: overall properties of heterogeneous materials*. North-Holland, Amsterdam, London, New York, Tokyo, 1993.

[77] R. Ogden. *Non-linear elastic deformations*. Dover Publications, Inc., Mineola, New York, 1984.

[78] C. Poizat and M. Sester. Effective properties of composites with embedded piezoelectric fibres. *Comput. Mater. Sci.*, 16:89–97, 1999.

[79] E. M. Purcell. *Electricity and magnetism, vol. 2 of Berkley physics course*. McGraw-Hill, Inc., New York, 1965.

[80] Q. Qin. *Fracture mechanics of piezoelectric materials*. WIT Press, Southamton, 2001.

[81] A. Reuss. Berechnung der Fliessgrenze von Mischkristallen auf Grund der Plastiz-itätsbedingung für Einkristalle. *Z. Angew. Math. Mech.*, 9:49–58, 1929.

[82] J. R. Rice. A path independent integral and the approximate analysis of strain concentration by notches and cracks. *J. Appl. Mech.*, 35:379–386, 1968.

[83] S. Ricker, J. Mergheim, and P. Steinmann. On the scale computation of defect driving force. *Int. J. Multiscale Comput. Eng.*, 7(5):457–474, 2009.

[84] S. Ricker, J. Mergheim, P. Steinmann, and R. Müller. A comparison of different approaches in the multi-scale computation of configurational forces. *Int. J. Frac.*, 166(1-2):203–214, 2010.

[85] E. Sanchez-Palenzia. Non-homogeneous media and vibration theory. *Lecture Notes in Physics*, 127:193–278, 1980.

[86] D. Schrade. *Microstructural modeling of ferroelectric material behavior*. PhD thesis, Technische Universität Kaiserslautern, Kaiserslautern, 2011.

[87] D. Schrade, R. Müller, and D. Gross. Parameter identification in phase field models for ferroelectrics. *Proc. Appl. Math. Mech.*, 9(1):369–370, 2009.

[88] D. Schrade, R. Müller, D. Gross, T. Utschig, V. Y. Shur, and D. C. Lupascu. In-teraction of domain walls with defects in ferroelectric materials. *Mech. Mater.*, 39:161–174, 2007.

[89] D. Schrade, R. Müller, B. X. Xu, and D. Gross. Domain evolution in ferroelec-tric materials: a continuum phase field model and finite element implementation. *Comput. Meth. Appl. Mech. Eng.*, 196(41-44):4365–4374, 2007.

[90] D. Schrade, B. X. Xu, R. Müller, and D. Gross. On phase field modeling of ferro-electrics: parameter indication and verification. *ASME conf. proc. (Smart Materi-als, Adaptive Structures and Intelligent Sytems 2008*, 1:299–306, 2008.

[91] J. Schröder. Derivation of the localization and homogenization conditions for electro-mechanically coupled problems. *Comp. Mater. Sci.*, 46:595–599, 2009.

[92] J. Schröder and M.-A. Keip. *A framework for the two-scale homogenization of electro-mechanically coupled boundary value problems, advanced structured ma-terials (1): computer methods in mechanics*. Springer, 2010.

[93] J. Schröder and M.-A. Keip. Multiscale modeling of electro-mechanically coupled materials: homogenization procedure and computation of overall moduli. *IUTAM Symposium on Multiscale Modelling of Fatigue, Damage and Fracture in Smart Materials*, 24 of IUTAM Bookseries:265–276, 2011.

[94] J. Schröder and M.-A. Keip. Two-scale homogenization of electro-mechanically coupled boundary value problems. *Comput. Mech.*, 50:229–244, 2012.

[95] V. Y. Shur, A. L. Gruverman, V. P. Kuminov, and N. A. Tonkachyova. Dynamics of plane domain walls in lead germanate and gadolinium molybdate. *Ferroelectrics*, 111(1):197–206, 1990.

[96] V. Y. Shur, A. L. Gruverman, V. P. Kuminov, and N. A. Tonkachyova. Dynamics of incoherent domain walls in gadolinium molybdate. *Ferroelectrics*, 130(1):341–346, 1992.

[97] V. Y. Shur, E. V. Nikolaeva, E. L. Rumyantsev, E. I. Shishkin, A. L. Subbotin, and V. L. Kozhevnikov. Smooth and jump-like dynamics of the plane domain wall in gadolinium molybdate. *Ferroelectrics*, 222(1):323–331, 1999.

[98] R. J. M. Smit, W. A. M. Brekelmans, and H. E. H. Meijer. Prediction of the mechanical behaviour of non-linear heterogeneous systems by multi-level finite element modeling. *Comput. Meth. Appl. Mech. Eng.*, 155:181–192, 1998.

[99] Y. Su and C. M. Landis. Continuum thermodynamics of ferroelectric domain evolution: theory, finite element implementation, and application to domain wall pinning. *J. Mech. Phys. Solid.*, 55(2):280–305, 2007.

[100] P. M. Suquet. Local and global aspects in the mathematical theory of plasticity. In S. Sawczuk and G. Bianchi, editors, *Plasticity today: Modelling, Methods and Applications*, pages 279-310, Elsevier, London, 1985.

[101] S. Suresh, A. Mortensen, and A. Needleman. *Fundamentals of metal-matrix composites*. Butterworth-Heinemann, Boston, 1993.

[102] K. Tanaka and T. Mori. Note on volume integrals of the elastic field around an ellipsoidal inclusion. *J. Elasticity*, 2:199–200, 1972.

[103] A. Teledano and H. Murakami. A high order mixture model for periodic particulate composites. *Int. J. Solid Struc.*, 23:989–1002, 1987.

[104] K. Terada and N. Kikuchi. Nonlinear homogenization method for practical applications. In Ghosh, S. and Ostoja-Starzewski, M., editors, *Computational methods in micromechanics*, AMD-Vol. 212/Md-Vol. 62, pages 1-16. ASME, 1995.

[105] K. Terada and N. Kikuchi. A class of general algorithms for multi-scale analysis of heterogeneous media. *Comput. Meth. Appl. Mech. Eng.*, 190:5427–5464, 2001.

[106] M. Toda, S. Tosima, E. Shima, and T. Iwasa. Variable delay devices using ferroelastic and ferroelectric crystal $Gd_2(MoO_4)_3$. *IEEE Transaction on Sonics and Ultrasonics*, SU-20(4):376–379, 1973.

[107] W. Voigt. Über die Beziehung zwischen den Elastizitätskonstanten isotroper Körper. *Wied. Ann.*, 38:573–587, 1889.

[108] J. Wang and M. Kamlah. Domain structures of ferroelectric nanotubes controlled by surface charge compensation. *Appl. Phys. Lett.*, 93(4):042906, 2008.

[109] J. Wang, S.-Q. Shi, L.-Q. Chen, Y. Li, and T.-Y. Zhang. Phase-field simulations of ferroelectric/ferroelastic polarization switching. *Acta Mater.*, 52(3):749–764, 2004.

[110] J. R. Willis. Bounds and self-consistent estimates for the overall properties of anisotropic composites. *J. Mech. Phys. Solid.*, 25:185–202, 1977.

[111] P. Wriggers. *Nichtlineare Finite-Element-Methoden*. Springer, Berlin, 2001.

[112] Y. Xu. *Ferroelectric materials and their applications*. Elsevier Science Publishers B.V., Holland, 1991.

[113] W. Zhang and K. Bhattacharya. A computational model of ferroelectric domains. Part I: model formulation and domain switching. *Acta Mater.*, 53(1):185–198, 2005.

[114] O. C. Zienkiewicz and R. L. Taylor. *The finite element method, the basis (volume 1)*. Butterworth-Heinemann, Oxford, 2000.

Lebenslauf

Name: Khalaquzzaman, Md

01/1983 - 04/1993   *Secondary School Certificate Examination*,
                           Rajshahi, Bangladesch

07/1993 - 08/1995   *Higher Secondary Certificate Examination*,
                           Dhaka, Bangladesch

12/1996 - 04/2002   Bachelorstudium im Bauingenieurwesen, *Bangladesh University of Engineering and Technology*,
                           Dhaka, Bangladesch
                           Abschluss: Bachelor im Bauingenieurwesen

10/2003 - 09/2009   Masterstudium im *Computational Sciences in Engineering*, TU Braunschweig
                           Abschluss: Master im CSE

10/2009 – 03/2012   Stipendiat im DFG-Graduiertenkolleg 814,
                           Lehrstuhl für Technische Mechanik,
                           Technische Universität Kaiserslautern

04/2012 – 11/2012   Stipendiat der TU Kaiserslautern,
                           Lehrstuhl für Technische Mechanik

12/2012 – 11/2013   Wissenschaftlicher Mitarbeiter,
                           Lehrstuhl für Technische Mechanik,
                           Technische Universität Kaiserslautern